Formation and Deposition of Polymer Nanostructures on Surfaces

Maria Wieland

Thesis submitted to the University of Nottingham

for the degree of Doctor of Philosophy

July 2015

Abstract

In this thesis different routes to the formation of extended two-dimensional polymers via on-surface coupling reactions are presented. Polyphenylene networks formed by the molecules tri-(bromo-phenyl)-benzene via on-surface Ullmann coupling reactions are investigated with scanning tunnelling microscopy. The polyphenylene networks with near complete surface coverage exhibit a vitreous structure. The network is composed of linked molecules forming polygons with four to eight edges.

A different set of covalently bound molecular nanostructures can be formed on a surface upon thermal activation of porphyrin building blocks. Porphyrin molecules are covalently linked to form one dimensional chains or extended networks using either Ullmann-type coupling reactions to link brominated phenyl sidegroups, or Glaser-Hay-type coupling to form butadiene links via reaction of two phenyl-ethylene sidegroups. The resulting polymers are investigated with scanning tunnelling microscopy and Raman spectroscopy.

In a complementary strand of research it is shown that thin films of C_{60} can promote adhesion between a gold thin film deposited on mica and a solution-deposited layer of the elastomer polymethyldisolaxane (PDMS). This molecular adhesion facilitates the removal of the gold film from the mica support by peeling and provides a new approach to template stripping which avoids the use of conventional adhesive layers. The fullerene adhesion layers may also be used to remove organic monolayers and thin films as well as two-dimensional polymers such as the porphyrin networks discussed previously. Following the removal from the mica support the monolayers may be isolated and transferred to a dielectric surface by etching of the gold thin film, mechanical transfer and removal of the fullerene layer by annealing/dissolution. The use of this molecular adhesive layer provides a new route to transfer polymeric films from metal substrates to other surfaces.

A different set of experiments investigated porphyrin nanorings and their interaction with C_{60} on a gold surface. Solvent-induced aggregates of nanoring cyclic polymers may be transferred by electrospray deposition to a surface where they adsorb as three dimensional columnar stacks. The observed stack height varies from single rings to three stacked rings. Those stacked layers of cyclic porphyrin nanorings constitute nanoscale receptacles with variable height and diameter which preferentially adsorb sublimed C_{60} molecules. Using scanning tunnelling microscopy the filling capacity of these nanoring traps is determined, as is the dependence of adsorbate capture on stack height and diameter.

List of publications

S. A. Svatek, L. M. A. Perdigão, A. Stannard, **M. B. Wieland**, D. V. Kondratuk, H. L. Anderson, J. N. O'Shea, and P. H. Beton, "Mechanical stiffening of porphyrin nanorings through supramolecular columnar stacking.," *Nano Lett.*, vol. 13, no. 7, pp. 3391–3395, Jul. 2013.

M. B. Wieland, A. G. Slater, B. Mangham, N. R. Champness, and P. H. Beton, "Fullerenes as adhesive layers for mechanical peeling of metallic, molecular and polymer thin films.," *Beilstein J. Nanotechnol.*, vol. 5, pp. 394–401, Jan. 2014.

S. Whitelam, I. Tamblyn, T. K. Haxton, **M. B. Wieland**, N. R. Champness, J. P. Garrahan, and P. H. Beton, "Common Physical Framework Explains Phase Behavior and Dynamics of Atomic, Molecular, and Polymeric Network Formers," *Phys. Rev. X*, vol. 4, no. 1, p. 011044, Mar. 2014.

M. B. Wieland, L. M. A. Perdigão, D. V. Kondratuk, J. N. O'Shea, H. L. Anderson, and P. H. Beton, "Height dependent molecular trapping in stacked cyclic porphyrin nanorings.," *Chem. Commun. (Camb).*, vol. 50, no. 55, pp. 7332–7335, Jul. 2014.

Acknowledgements

It is a pleasure for me to finally thank those people who made this thesis possible. First and foremost I would like to thank my supervisor Peter for giving me the opportunity to be part of the nanoscience group. His guidance and support over the last four years made me learn a lot and the PhD a very enjoyable time. Always having enough space and freedom to learn from my own mistakes was surely an additional motivation for me.

I also want to thank the members of the nanoscience group who all contributed in some way to this thesis. It has always been a great atmosphere working within the team. Especially I want to mention the very patient Luis, who was always on call to fix my UHV issues. This made life a lot easier. Thanks to my fellow students Julian, Jason, Faris, Dave, Simon, Alex, Pete and Rob for discussions, explanations, teamwork, improving my English, Friday pub and other extracurricular activities.

Special thanks belong to Julian, Dave, Phil, and the other physics buskers who introduced and included me to the physics outreach activities. This helped me decide on and pursue a career path in science communication.

Contents

1. Introduction and scope **1**

1.1. Overview of this thesis 3

2. Background **5**

2.1. On-surface coupling and polymerisation 6

2.1.1. Ullmann coupling 9

2.1.2. Dehydration reaction 18

2.1.3. Imine (Schiff base) and imide formation 20

2.1.4. Acetylenic (Glaser-Hay) coupling 22

2.1.5. Tautomerisation 26

2.2. Porphyrin 27

2.2.1. Porphyrin monomers 27

2.2.2. Synthesis of porphyrin oligomers 30

2.2.3. Porphyrin and spectroscopy 35

2.3. Template stripping and transfer printing techniques 40

2.3.1. Template stripped metal surfaces 41

2.3.2. Transfer printing 43

3. Experimental technique **48**

3.1. Introduction 49

3.2. Ultra high vacuum and deposition techniques 49

3.2.1. Ultra high vacuum 49

3.2.2. Sample preparation via argon ion sputtering and annealing 52

3.2.3. Deposition via sublimation from a Knudsen cell 53

3.2.4. Electrospray deposition 55

3.3. Scanning tunnelling microscopy 57

3.3.1. Quantum mechanic tunnelling 57

3.3.2. Tersoff-Hamann theory 60

3.3.3. Imaging molecules on surfaces 62
3.3.4. Experimental setup 63
3.4. Spectroscopy 66
3.4.1. Fluorescence spectroscopy 66
3.4.2. Raman spectroscopy 69

4. Formation of extended covalent networks via Ullmann coupling 72
4.1. Introduction 73
4.2. Formation of extended polyphenylene networks 74
4.3. On-surface polymerisation of porphyrin monomers. 83
4.4. Conclusions 90

5. The transfer of metallic, molecular, and polymer thin films using fullerenes as adhesive layers 91
5.1. Introduction 92
5.2. Fullerenes as an adhesive 94
5.3. Transfer of molecular thin films and covalent networks 98
5.3.1. Steps of the transfer process shown for molecular thin films 98
5.3.2. Transfer of covalent organic networks 103
5.4. Conclusions and Outlook 108

6. Molecular trapping in stacked porphyrin nanorings 109
6.1. Introduction 110
6.2. Electrospray deposition of porphyrin nanorings 112
6.3. Adding fullerenes 114
6.4. Analysis and statistics of the STM images 117
6.5. Comparison with c-P12 120
6.6. Transfer of cyclic porphyrin nanorings 123
6.7. Conclusions 126

7. Raman and STM studies of acetylenic (Glaser-Hay) coupling of porphyrins **127**

7.1. Introduction 128

7.2. Raman studies of one-dimensional polymerisation of solution deposited di-ethynyl porphyrin monomers 130

7.3. STM and Raman studies of two-dimensional polymerisation of electrospray deposited tetra-ethynyl porphyrin monomers 135

7.4. Conclusions and outlook 140

8. Summary and Outlook **142**

9. Bibliography **145**

Chapter 1

Introduction and scope

One aspect of this thesis that combines the different experimental chapters is the on-surface formation of polymer nanostructures. A major objective of nanoscience is the realisation of nanostructures suitable for molecular electronics. In future technologies logic gates and circuits could be integrated in intramolecular structures, providing an interesting alternative to microelectronic devices based on silicon. To realise this strategy, bottom-up approaches for the formation of atomically precise, extended, and stable structures are required. Tailored organic molecules undergo on-surface coupling reactions to form well defined nano architectures. The formation of those structures typically requires ultra high vacuum conditions to avoid contaminations by ambient gases or solvents. The on-surface formation of covalently linked structures under UHV conditions conveys a range of advantages. The formation of stable covalent bonds provides high stability to the resulting structure. The absence of solvents in UHV allows for a larger range of reaction temperatures and the choice of substrate may act as a catalyst for the reaction. However, a drawback of covalently coupled structures is their non-reversible nature. Thus an understanding and optimisation of the formation of two-dimensional polymers is important to develop this field.

Another important aspect of this thesis is the use of porphyrin molecules. Porphyrins are a class of naturally occurring macrocyclic compounds which play an important role in the metabolism of living organisms. Porphyrin derivatives are ubiquitous in natural systems, they occur in essential biological processes such as photosynthesis or oxygen transport in the blood. Thus porphyrins are widely studied due to their prospective applications in mimicking enzymes, catalytic reactions, photodynamic therapy, molecular electronic devices, and conversion of solar energy. In particular, numerous porphyrins based artificial light-harvesting antennae, and donor acceptor dyads and triads have been prepared and tested to improve our understanding of the photochemical aspect of natural photosynthesis. Key aspects of porphyrins are their special

absorption, emission, charge transfer and complexing properties as a result of their characteristic ring structure of conjugated double bonds.

1.1. Overview of this thesis

The background chapter provides an overview of the current developments in the on-surface formation of two-dimensional polymers and the different on-surface coupling reactions this entails. Further it gives a summary of porphyrin, the synthesis of porphyrin-based molecules and a background to spectroscopy of porphyrin and its derivatives. Last it gives an introduction to the history and current developments in template stripping and transfer printing methods.

The experimental techniques chapter provides an overview of the techniques used in this thesis. The basic principles and setup of the ultra high vacuum chambers used for the experiments is given. Scanning tunnelling microscopy, fluorescence spectroscopy, and Raman spectroscopy are the main analytical techniques used in this thesis. Thus a brief overview of the basic theory and experimental setup is given for each of those techniques.

The focus of chapter four is on the on-surface formation of two-dimensional networks via Ullmann coupling reactions on gold surfaces. The reaction is mediated by the catalytically induced breaking of carbon-halogen bonds. First, extended polyphenylene networks, networks solely consisting of phenyl rings, are formed, imaged, and analysed. The networks exhibit a vitreous structure after formation and deviate from their expected honeycomb symmetry. Further, extended networks of phenyl-porphyrin molecules are formed via the phenyl sidegroups. The resulting porphyrin networks exhibit patches of network with square symmetry within a disordered matrix.

Chapter five explores the adhesive properties of the fullerene C_{60}. Thin films of C_{60} can promote adhesion between a gold thin film on mica and an elastomer.

This molecular adhesion facilitates the removal of the gold film from the mica support by peeling and provides a new approach to template stripping. The fullerene adhesion layer is further explored as a way to remove organic monolayers and thin films as well as two-dimensional polymers from the gold surface. Following the removal from the mica support the monolayers may be isolated and transferred to a new substrate by etching of the gold thin film, mechanical transfer and removal of the fullerene layer by annealing/dissolution. The use of this molecular adhesive layer provides a new route to transfer polymeric films from metal substrates to other surfaces as is demonstrated for an assembly of covalently coupled porphyrins. Porphyrins exhibit strong fluorescence, monolayers of monomers or two-dimensional polymers can be detected with fluorescence spectroscopy and are thus ideal for the transfer experiments.

Chapter six takes a look at different porphyrin based molecules. Solvent-induced aggregates of porphyrin nanorings are transferred by electrospray deposition to a surface where they adsorb as three dimensional columnar stacks. Those stacked layers of porphyrin nanorings constitute nanoscale receptacles which preferentially adsorb sublimed molecules. Using scanning tunnelling microscopy the filling capacity of these nanoring traps is determined, as is the dependence of adsorbate capture on stack height and diameter.

The last experimental chapter explores a different on-surface coupling reaction, acetylenic or Glaser-Hay coupling, on the example of porphyrin. Tis coupling reaction results in polymerised structures with a distinct Raman spectrum. Monomers are deposited from solution by immersion or vial electrospray onto various substrates and covalently linked via annealing. The resulting structures are analysed with Raman spectroscopy and STM.

Chapter 2

Background

2.1. On-surface coupling and polymerisation

This chapter provides an overview over the different types of on-surface covalent coupling reactions. The polymerisation of tailored molecular building blocks on surfaces has been in the focus of surface science related studies since the mid-2000s [1]. Due to a much higher bond strength compared with weak bonds such as Van der Waals interactions, covalent organic networks exhibit much higher thermal and chemical stability, as shown in Table 2-1.

Interaction type	*Interaction energy [eV]*
Van der Waals	0.02 – 0.1
Hydrogen bonding	0.05 – 0.4
Metal-coordination bonds	0.5 – 2
Covalent bonding	3

Table 2-1: Interaction energy of the different bond types [2].

Van der Waals interactions encompass intermolecular attractive and repulsive forces between dipoles. They are relatively weak and rapidly diminish with increasing distance between interacting molecules. Halogenated molecules, for example tri-(bromo-phenyl)-benzene [3], often form regular self-assembled monolayers stabilised by van-der Waals interactions and halogen bonds. Such halogen-terminated molecules are typically the educt for the Ullmann-type covalent coupling reactions described in section 2.1.1.

A hydrogen bond derives from an electrostatic attractive interaction between a hydrogen atom with a positive partial charge, and an electron lone pair of an electronegative atom such as oxygen or nitrogen. Hydrogen bonds play an important role in self-assembled monolayers of molecules which have functional groups containing hydrogen atoms and electronegative atoms, for example carboxylic acids [4].

Due to the relatively weak interaction energy of Van der Waals interactions and hydrogen bonds the thermal and chemical stability of self-assembled

monolayers stabilized via such interactions is very low. However, this permits self-healing processes of the structures, resulting often in large areas of long range ordered patterns with few defects, as compared to more stable covalently coupled extended networks [3].

Metal coordination bonds are commonly defined as interactions between organic molecules via a metal adatom. A metal atom, acting as an electron pair acceptor, increases the interaction energy further. Metal coordination bonds may be realised by deposition of organic building blocks directly onto a metal substrate, where the adatoms from the surface can be incorporated as coordination centres. This approach requires only one deposition step, but limits the choice of substrate [5]. Alternatively, the metal adatoms can be deposited in a separate sublimation step. This decouples the choice of substrate from the choice of metal coordination centre and thus allows for greater variety in the nano architectures [6]. In some studies metal coordinated networks have been reported that function as a protopolymer prior to thermally induced conversion to form a polymer through covalent coupling [5, 7].

Covalent bonds were first defined by Langmuir in 1919 [8] as shared electron pairs between atoms. Covalent bonds are directed, rigid, and stable with interaction energies up to two orders of magnitude higher than van der Waals or hydrogen bonding, as shown in Table 2-1. Covalent bonds enable the bottom-up synthesis of chemically and thermally stable polymeric nano architectures. However, the high interaction energy prevents cleaving and recombination processes that may heal defects, often resulting in a high degree of disorder for extended structures [3].

Molecules with well-defined structures are required for the formation of tailored one- or two-dimensional polymers. The structure of the monomer typically includes a backbone and functional groups attached to the backbone. To realise on-surface coupling, two-dimensional molecules with coplanar functional groups adsorb on a target surface before they polymerise into larger

structures. An overview of some possible bottom-up formation approaches for two-dimensional polymers is shown in Figure 2-1.

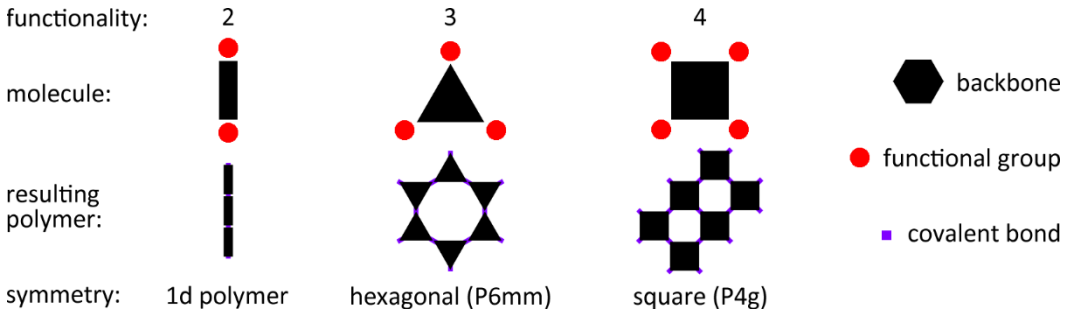

Figure 2-1: Overview of bottom-up synthesis of polymers with varying symmetry of monomers with different functionalities.

These simplified depictions of molecules consist of a backbone (black) with a certain symmetry and functional groups attached to corners of the backbones which follow that symmetry (red). The functionality refers to the number of reactive sites (purple) after activation of the functional groups. It is the parameter that determines the topology of the resulting polymer. One functional group attached to a backbone limits the reaction to dimer synthesis. Two functional groups already allows the formation of one-dimensional polymer chains. Three or more functional groups lead to dendritic polymerisation and may result in fully cross-linked two-dimensional structures.

The nature of the functional groups determines the chemical structure of the resulting covalent bond after the coupling reaction and which residual groups (if any) are present afterwards. Examples of such residual groups are halogen atoms and H_2O. Residual groups are not part of the final polymeric structure. The chemical properties of the leaving groups and the substrate influence whether the residual groups are co-adsorbed with the polymer on the surface, or desorb after activation of the functional groups.

Some covalent organic networks have been predicted to exhibit semiconducting properties similar to graphene [9], with possible applications in

the field of optoelectronics. Alternatively the tuneability and high porosity of covalent networks makes them suitable for gas storage [10, 11] or usable as catalysts [12].

2.1.1. Ullmann coupling

The most common on-surface coupling reaction explored to date is the Ullmann coupling of aryl halides on different metal substrates. The reaction is named after German chemist Fritz Ullmann, who first described the formation of dinitrio-biphenyl by heating bromo-nitrobenzene in the presence of a copper powder catalyst in solution in 1901 [13]. This reaction basically consists of three steps as shown in Figure 2-2.

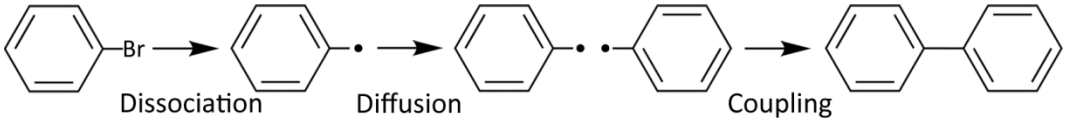

Figure 2-2: Steps of the Ullmann reaction on the example of bromo-benzene forming a biphenyl.

The first step is the dissociation of the bromo-benzene to a phenyl radical (that is prone to dimerization) and bromine, followed by diffusion of the phenyl groups to find another phenyl as a reaction partner. The third and final step is the formation of covalent bonds to form biphenyl. The Ullmann reaction is commonly used in synthetic chemistry due to its versatility and typically high yields. In the late 90s and early 2000s Rieder and co-workers pioneered on-surface coupling via the Ullmann reaction. Hla [14] recreated this reaction step-by-step in situ on a copper substrate using various STM manipulation techniques. The STM tip-induced synthesis steps of a biphenyl molecule on a copper substrate start with the deposition of small amounts of iodobenzene onto a clean Cu(111) surface held at 20K. The first reaction step separates the iodine from the iodobenzene via electron-induction of the tip at 1.5 V while the tip is positioned over the molecule [15]. Subsequently the iodine atom is moved

to a terrace site by lateral manipulation. Using the same manipulation parameters two phenyls are brought together. The last step of the reaction is the electron-induced chemical association of the phenyl groups to form biphenyl. To confirm that the coupling reaction worked, the synthesized biphenyl molecule is pulled by its front end with the STM tip.

Since then, Ullmann-type metal mediated radical covalent coupling on surfaces has been reported using a variety of halogenated organic compounds. An example of covalent networks formed via the Ullmann reaction, related to the experiments described in section 4.3 is the formation of covalently bonded nano architectures with halogenated tetra-phenyl-porphyrins as building blocks.

Grill and co-workers [16] were the first to report the formation of two-dimensional covalent networks on a surface. In 2007 they described Ullmann-type covalent coupling of tetra-phenyl-porphyrin molecules. The synthesis and properties of porphyrin and its derivatives will be described in detail in section 2.3. The molecule Grill and co-workers use in their work is tetra-phenyl-porphyrin (TPP), a porphyrin macrocycle with four substituted phenyl/ bromophenyl rings in varying composition. Once activated, these TPP molecules form dimers, chains or two-dimensional networks, depending on the number of bromine substituents, as shown in the STM images in Figure 2-3.

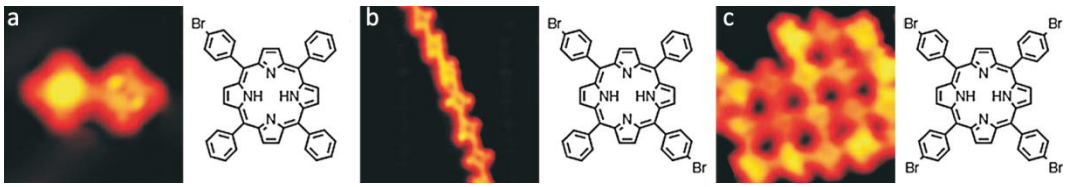

Figure 2-3: STM images (a: 5 x 5 nm^2, b: 10 x 10 nm^2, c: 8.5 x 8.5 nm^2) of the nanostructures after activation and connection of the different monomer building blocks with one (a), two (b), and four (c) Br substituents [16].

Activation was achieved via two different methods. One approach is to sublime the molecules at 180°C onto Au(111) kept at room temperature. Subsequent annealing of the gold substrate activated the molecules and led to the formation of covalent bonds. In an alternative method the molecules were deposited at an elevated evaporator temperature of 220°C, causing the activation of the molecules already in the evaporator, so that molecules land on the surface ready to form covalent bonds upon diffusion. Both methods lead to similar results of small patches of covalently bonded structures, as shown in Figure 2-3c. In the case of porphyrin monomers with one bromine substituent, only dimers were observed on the surface, as shown in Figure 2-3a. With two bromine substituents in the *trans* geometry the porphyrin molecules form long, linear chains, as shown in Figure 2-3b.

In 2012 Grill and co-workers [17] developed molecular architecture further by using I_2Br_2TPP, porphyrin monomers with these types of halogenated linkers: two bromine and two iodine substituents in *trans* configuration, as depicted schematically in Figure 2-4a. The bromine-phenyl group has a higher dissociation energy than the iodine-phenyl group, thus enabling stepwise dissociation and covalent linking first into chains with subsequent formation of a two-dimensional extended network, as shown in Figure 2-4b.

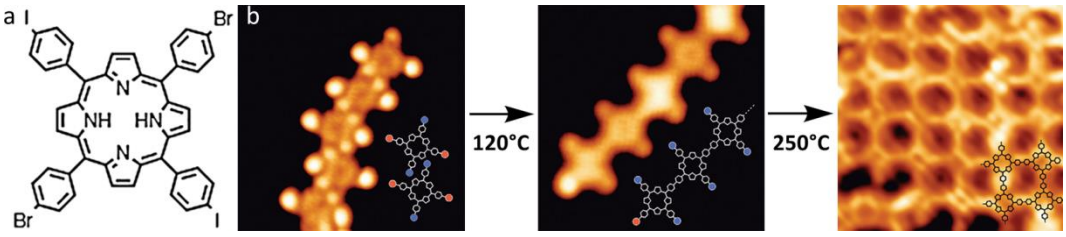

Figure 2-4a: Schematic of a trans-Br_2I_2TPP molecule; b: STM images of stepwise dissociation of the different halogen-phenyl groups of the porphyrin molecules [17].

After deposition of the molecules onto a Au(111) surface kept at -200°C, the sample is annealed to 120°C. This enables dissociation of the iodine and linear

polymerisation of the porphyrins into chains. Following that, the sample is heated to 250°C, creating a two-dimensional network by dissociation of the bromine and interconnection of neighbouring chains. The resulting network exhibits fewer defects and better long-range order than networks built up of Br_4TPP described earlier.

Another group of molecules that form networks via Ullmann-type radical covalent coupling are halogen-terminated phenyl based molecules, such as tri-(bromo-phenyl)-benzene (TBPB) [7, 3] or hexaiodo-substituted-cyclohexa-m-phenylene (HCP) [18]. The resulting polyphenylene networks, also called porous graphene, solely consist of two- and threefold benzene rings arranged (ideally) in hexagonal patterns of varying pore size as shown in Figure 2-5.

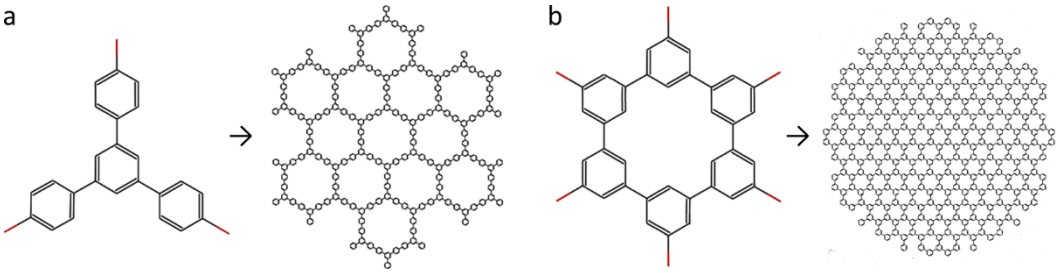

Figure 2-5: Two examples of polyphenylene networks; a: Tri-(bromo-phenyl)-benzene (TBPB) and its ideal hexagonal covalent network; b: Hexaiodo-cyclohexa-m-phenylene (HCP) and its ideal hexagonal covalent network.

Those networks can be viewed as graphene sheets with systematically removed carbon atoms and hydrogen saturation to form regular pores. Depending on the structure of the polyphenylene, significantly different optoelectronic properties such as the band gap are predicted for the structures according to DFT [9].

Previous work done in the Nottingham nanoscience group was on the polymerisation of TBPB on a Au(111) substrate and subsequent molecular adsorption in the cavities of the network [3]. Deposition of the molecules from a Knudsen cell onto a gold substrate at room temperature in UHV leads to the

formation of close-packed ordered structures, as shown in the STM image in Figure 2-6a. Annealing of that sample at moderate temperatures of 110°C causes the molecules to form dimers. The dimers also form close packed ordered structures, as shown in Figure 2-6b. Further annealing leads to cross-polymerisation and the formation of a highly cross-linked, disordered network. The molecular density of the self-assembled monolayers is higher than the density of molecules in the target open-porous polymer, so the formation of the network requires a different strategy.

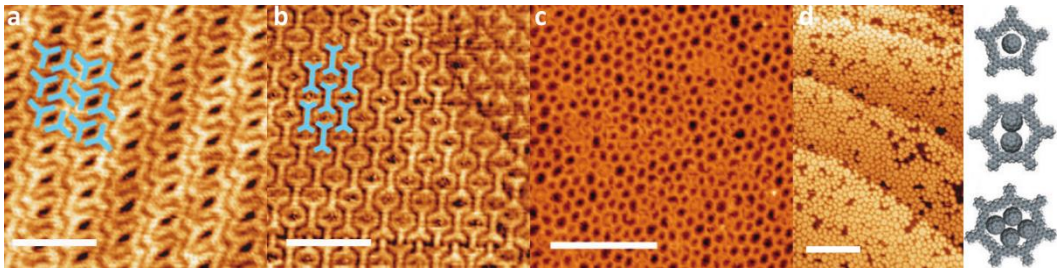

Figure 2-6a: STM image of a close-packed monolayer TBPB on Au(111); scale bar 4 nm; b: STM image of ordered domains of dimerised TBPB after annealing at 110°; scale bar 5 nm; c: STM image of a porous covalent network formed at a substrate held at 140°C and subsequent annealing; scale bar 19 nm; d: STM image and structural models of captured C_{60} in the cavities of a porous TBPB network; scale bar: 20 nm [3].

In such an alternative approach the molecules are deposited onto a heated substrate with subsequent annealing. Due to the increased mobility and reactivity of the molecules on the surface, an open-porous extended polymer network is formed as shown in Figure 2-6c. Additionally to the expected hexagonal structures depicted in Figure 2-5a, polygons with 4, 5, 7, or 8 corners are observed. The statistics of the polygon distribution in those networks will be addressed in more detail in the experimental section 4.1.

Subsequently, C_{60} molecules were deposited onto the TBPB polymer and imaged with an UHV-STM. The molecules are trapped inside the pores and form

clusters, where the size of the cluster depends on the pore size. Figure 2-6d shows an STM image of a TBPB network with a high coverage of C_{60} molecules trapped in the cavities. Pentagons are observed only with one fullerene molecule trapped. Clusters of two C_{60} are prevalent and occur in hexagons, clusters of more than two molecules are present in heptagonal or larger pores. These results show that covalent structures may be used to template the adsorption of guest molecules.

The substrate can play an important role in the formation of polyphenylene networks as shown by Lackinger and co-workers [7]. They investigated the formation of covalent TBPB networks depicted in Figure 2-5a on different substrates: graphene, Cu(111), and Ag(110). On graphene the molecule forms a non-covalent self-assembled ordered structure that desorbs upon annealing rather than forming a covalent organic framework. This is not surprising since the Ullmann reaction requires a metal catalyst to occur. On Cu(111) and Ag(110) the molecules first form a protopolymer upon deposition onto a substrate held at room temperature, as shown in the STM image in Figure 2-7a.

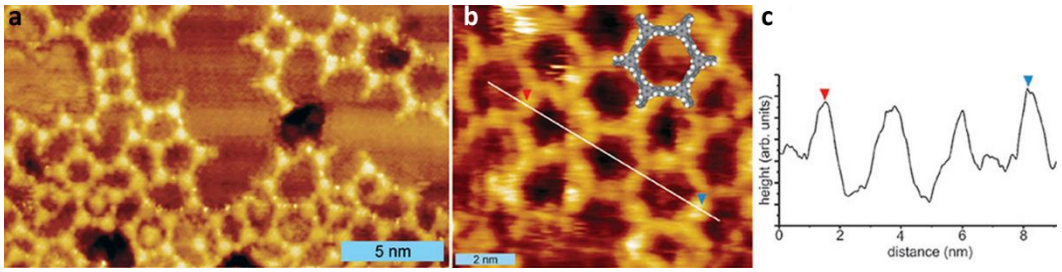

Figure 2-7a: STM image of TBPB protopolymer on Cu(111) before annealing; spherical protrusions between radicals are clearly observable; b: STM image of TBPB covalent organic framework on Cu(111), evaporation temperature of 140°C for 8 minutes and subsequent annealing to 300°C, a scaled hexagonal ring is overlaid; c: Line scan as indicated in 2-3b across three rings yielding a centre-to-centre distance of 2.2 nm for a single ring [7].

In this protopolymer the molecules dissociate and diffuse to form the expected hexagonal pattern. But the third step of the Ullmann coupling reaction, the covalent coupling, has not occurred yet. Instead, the radicals seem to be linked via a metal atom, resulting in larger bond lengths than expected for a covalent network, according to DFT calculations. Visible in the STM images of the protopolymer are bright protrusions between adjacent molecules. The authors attribute these to single copper atoms coordinating two radicals.

To induce the third step of the Ullmann reaction, the sample is annealed. After heating the sample to 300°C a network consisting of mostly five to seven membered rings is formed shown in Figure 2-7b. The dimensions of these rings, see line scan in Figure 2-7c, now correlate with calculated bond lengths and literature values for a hexagonal covalent framework consisting of phenyl rings, as shown in Figure 2-5a.

In 2010 Fasel and co-workers [18] discussed how the substrate influences the adsorption energies, diffusion barriers, and lateral interactions of the molecules involved in the coupling reaction. They investigated the behaviour of the hexaiodo-substituted macrocycle cyclohexa-*m*-phenylene (CHP) on Cu(111), Au(111), and Ag(111) with a combination of STM, XPS, and DFT. CHP is a macromolecule composed of six phenyl rings in cyclic conformation. The outwards pointing carbon atom in each phenyl ring is substituted with iodine, as depicted in Figure 2-5b. The resulting ideal network is similar to the network TBPB forms as shown in Figure 2-5a, only with smaller cavities.

As in the work described previously, the molecules are dehaloginated after deposition onto the surface held at room temperature without further annealing required. The iodobenzene bond dissociates below room temperature on all three metal substrates, as XPS analysis shows. The radicals are then stabilized by free electrons of the metal surface, preventing immediate covalent coupling. The formation of covalent aryl-aryl bonds is thermally induced and leads to significantly different network structures depending on the substrate, as

depicted in the STM images in Figure 2-9. Covalent coupling occurs at different temperatures depending on the substrate. The molecules form covalent bonds at about 200°C on Cu(111), at 250°C on Au(111), and at 300°C on Ag(111). On Cu(111) the networks form dendritic structures predominantly of single molecule wide branches, as shown in the STM image in Figure 2-8a. On the Au(111) surface small islands of close packed hexagonal networks with short branches are observed, as shown in Figure 2-8b. Figure 2-8c shows an STM image of the molecules on Ag(111). Here large islands of highly ordered and dense hexagonal networks prevail.

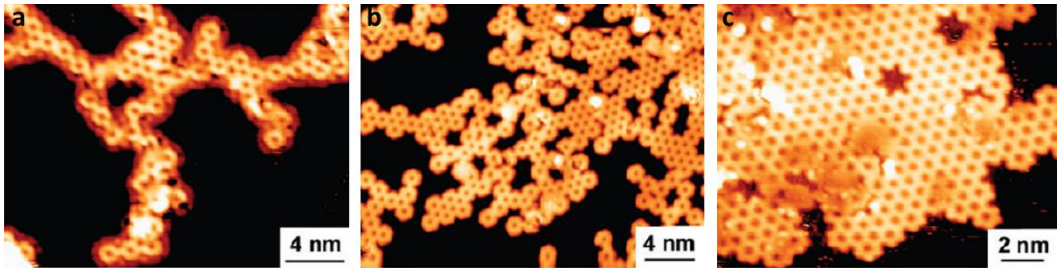

Figure 2-8: STM images of polyphenylene networks on Cu(111) (a), Au(111) (b), and Ag(111) (c) [18].

Using DFT the authors calculate the nature of the surface stabilized CHP radicals, as well as diffusion and reaction parameters. On Cu(111) the CHP radicals encounter a high diffusion barrier, but a low coupling barrier. They form covalent bonds as soon as the first diffusion barrier is overcome. On Ag(111) the opposite is the case. The molecules are very mobile, but the intermolecular coupling has a significantly higher barrier. This leads to extended regular two-dimensional networks.

In further work using phenyl-based molecules Fasel and co-workers [19] combined the Ullmann type reaction with thermally activated cyclodehydrogenation to form well defined graphene nanoribbons. Graphene nanoribbons (GNRs) comprise narrow strips of graphene with a width below 50 nm. GNRs are predicted to exhibit interesting electronic properties that differ

from extended graphene sheets due to quantum confinement and edge effects. The authors present methods for the fabrication of atomically precise GNRs of different topologies with widths below 10 nm as shown in Figure 2-9.

Linear GNRs with a width of seven carbon atoms were fabricated from the molecule dibromo-bianthryl, as shown in Figure 2-9a. The molecules were sublimed onto a Au(111) surface. The molecules immediately dissociate on the surface to form a surface-stabilized radical. Upon thermal activation at 200°C the molecules diffuse and form covalent bonds resulting in extended polymer chains. In this process the dehalogenation, diffusion, and covalent coupling occurs at over 200°C lower than the cyclodehydrogenation, making the process easy to control and observe.

In a second thermally activated step at 400°C, cyclohydrogenation leads to fully aromatic armchair ribbons with lengths up to 50 nm, as shown in the STM image in Figure 2-9a.

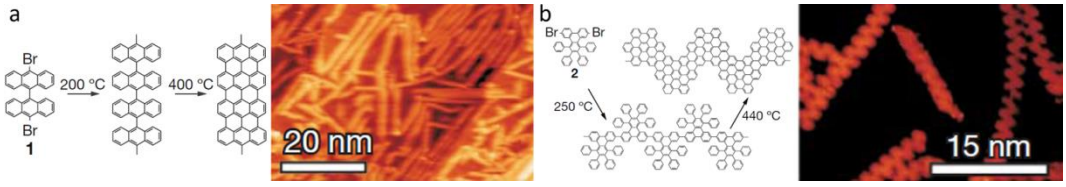

Figure 2-9a: Reaction scheme from 10,10'-dibromo-9,9'-bianthryl monomers to straight GNRs and STM image of the resulting straight GNRs on Au(111); b: Reaction scheme from 6,11-dibromo-1,2,3,4-tetraphenyltriphenylene monomer to chevron-type GNRs and STM image of the resulting chevron-type GNRs on Au(111) surface [19].

A similar approach for the formation of chevron-type (zig-zag) GNRs with alternating widths of 6 and 9 carbon atoms is depicted in Figure 2-9b. The molecule dibromo-tetra-phenyl-triphenylene was sublimed onto Au(111). For this molecule diffusion and covalent coupling occurs at 250°C. Once again the fully aromatic GNRs were produced via annealing at 440°C causing

intramolecular cyclohydrogenation. The STM image in Figure 2-9b shows chevron-type GNRs. The nanoribbons preferentially align with the herringbone reconstruction of the Au(111) surface and exhibit lengths of up to 30 nm.

2.1.2. Dehydration reaction

A dehydration reaction is a condensation reaction and usually defined as a chemical process that involves the loss of water from the reacting molecules, as depicted on the example of phenol in Figure 2-10.

Most on-surface dehydration reactions can be achieved in both UHV and solution conditions. By forming the networks in solution in some cases the water can hydrolyse the bond again and facilitate self-repair. Under UHV conditions the volatile water typically desorbs immediately after formation.

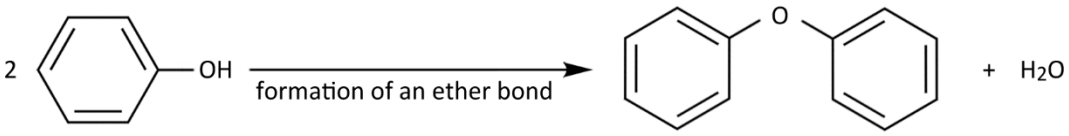

Figure 2-10: Dehydration reaction on the example of the conversion of phenol to diphenyl ether and water.

The first examples for the formation of extended covalent organic networks with near complete monolayer coverage were shown by Porte and co-workers in 2008 [20]. 1,4-benzenediboronic-acid (BDBA), a linear molecule with two hydroxyl groups on each end forms open-porous hexagonal structures as shown in Figure 2-11a. Covalent coupling of three BDBA molecules via molecular dehydration creates the three-folded junctions of the network.

The resulting open-porous network has a very high coverage across large areas of the surface, as shown in the STM image in Figure 2-11b. The coupling reaction takes place at room temperature directly after deposition of the molecules and the resulting polymer is stable up to 500°C for short annealing times.

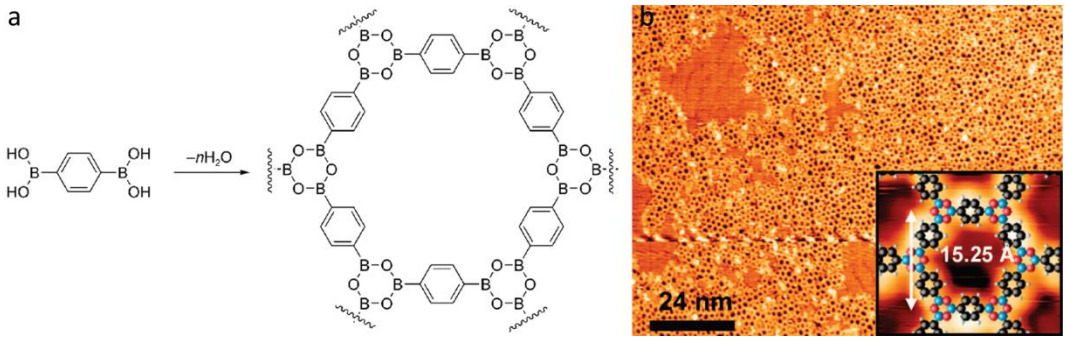

Figure 2-11a: Polymerization of BDBA by dehydration; b: STM image the BDBA network; inset: network with overlaid chemical structure obtained by DFT calculation [20].

To show the versatility and tuneability of such organic frameworks, another network was formed using the same coupling reaction with the linear BDBA and HTTP, a tri-fold monomer as shown in Figure 2-12a.

The covalent coupling via dehydration of 1,4-benzene-di-boronic-acid (BDBA) and 2,3,6,7,10,11-hexa-hydroxy-tri-phenylene (HHTP) leads to an equally stable framework connected by ester bonds with a larger pore size compared to the pure BDBA polymer.

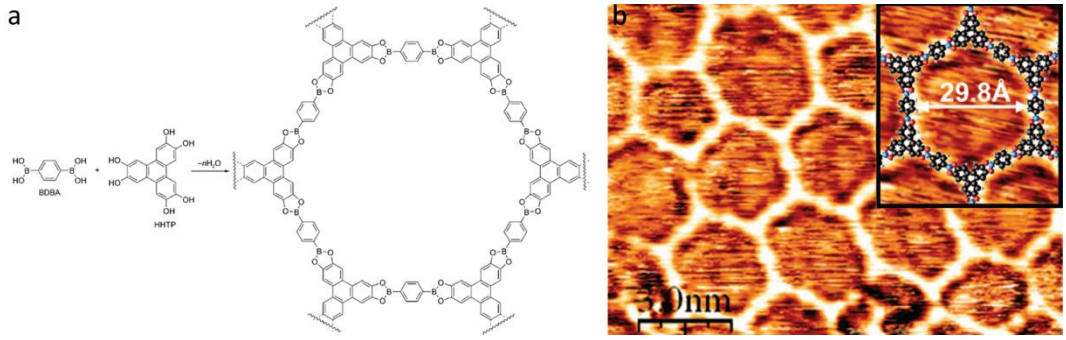

Figure 2-12a: Polymerization by esterification of BDBA with HHTP; b: STM image of the BDBA – HHTP network showing hexagonal and other polygon structures; inset: network with overlaid chemical structure obtained by DFT calculation [20].

In this system the three-folded HHTP sits at the junctions of the network with the linear BDBA linking. It is also notable that the larger framework built of two different molecules shows fewer defects than the smaller framework consisting only of BDBA. The authors attribute this to the former being a bimolecular reaction opposed to the latter being a reaction including three molecules.

2.1.3. Imine (Schiff base) and imide formation

The imine (Schiff base) and imide formations are specific dehydration reactions. A Schiff base, named after Hugo Schiff, is a compound with a functional group that contains a carbon-nitrogen double bond with the nitrogen atom connected to an aryl or alkyl group. The reaction typically takes place when an aldehyde group and an amine group react to form an imine bond (red) under the dissociation of water, as shown in Figure 2-13.

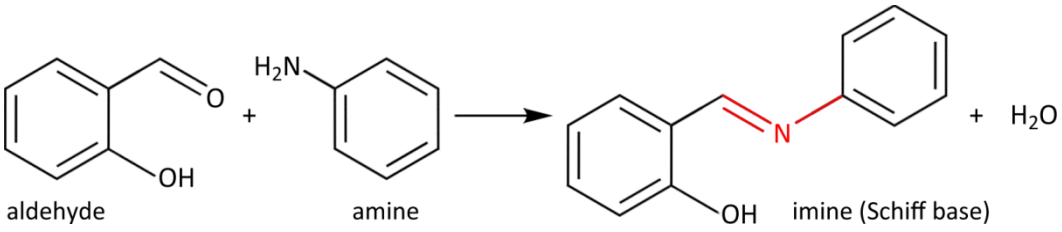

Figure 2-13: Schiff base formation on the example of salicylaldehyde and phenylamine reacting to an imine (Schiff base, red) and water.

Although not forming extended covalent frameworks, Linderoth and co-workers [21] described the interesting on-surface reaction of an aldehyde and an amine to form an imine, as depicted in Figure 2-14a. The biimine is coadsorbed on a Au(111) surface under UHV conditions by subsequent adsorption of dialdehyde and octylamine.

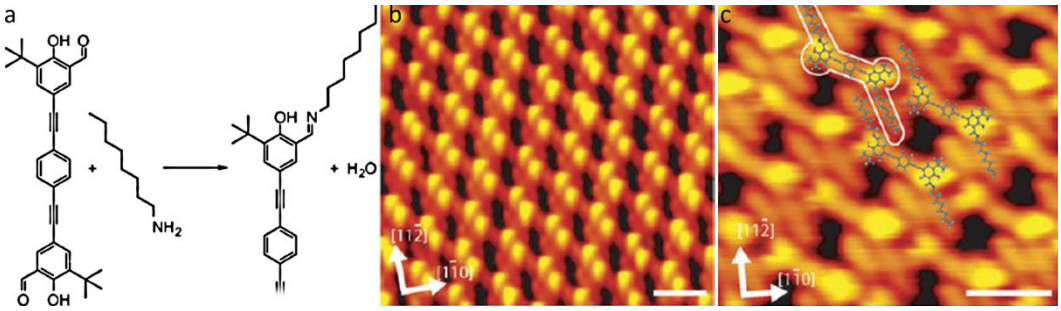

Figure 2-14a: On-surface formation of an imine; b: STM image of a large ordered domain formed by the diimine prepared in situ and annealed at 180°C; scale bar: 4 nm; c: STM image of a self-assembled structure formed by the diimine prepared ex situ; scale bar: 2 nm [21].

An imide is a functional group where two acyl groups bind to one nitrogen atom as depicted in Figure 2-15 (red). Most imides are synthesised via condensation of a dicarboxylic acid or an anhydride and an amine group.

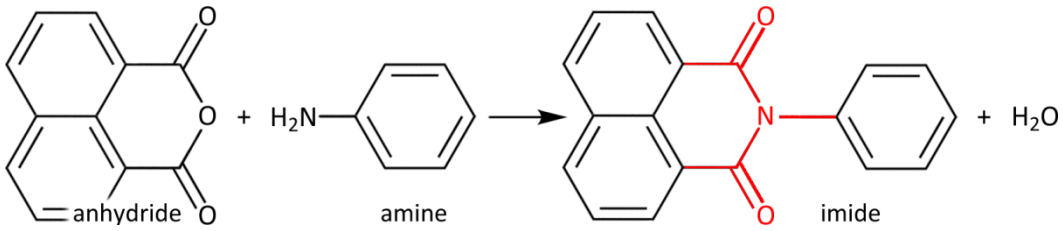

Figure 2-15: Imide formation on the example of naphthalic anhydride and phenylamine reacting to an imide (red) and water.

In 2008 Fasel and co-workers reported the thermally initiated formation of a polyimide network of amine and anhydride building blocks [22]. The linear dianhydride perylenetetracarboxylic-dianhydride (PTCDA) was combined with the linear amine diamino-terphenyl (DATP) or the three-fold amine tri-(aminophenyl)-triazine (TAPT) to form polymer chains or a two-dimensional polymer, respectively. The dianhydride and amine molecules were deposited onto a clean Au(111) surface at room temperature in UHV and subsequently annealed at 300°C to initiate imide formation. The resulting polymer structures were imaged with an STM, as shown in Figure 2-16.

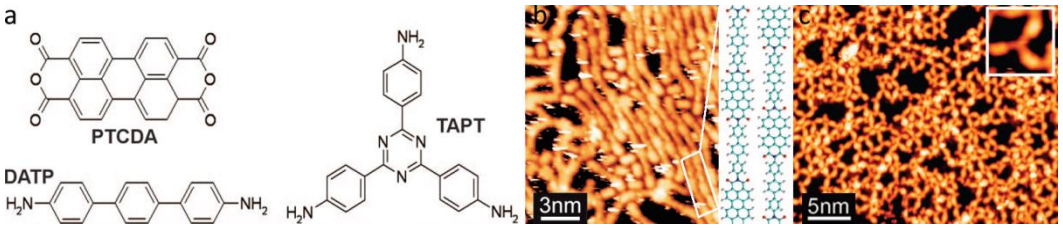

Figure 2-16a: Chemical structure of perylenetetracarboxylic-dianhydride (PTCDA), diamino-terphenyl (DATP), and tri-(aminophenyl)-triazine (TAPT), the compounds used for surface polyimide formation; b: STM image of linear polyimide chains formed from PTCDA and DATP after annealing at 300°C; inset: structure of the polyimide; c: STM image of a porous polyimide network formed from PTCDA and TAPT after annealing at 330°C [22].

Covalently linked one- and two-dimensional polymers of submonolayer coverage are formed depending on the precursor molecules. The linear oligomers have a length of 5 to 10 nm and form islands of parallel assembled strands, where individual strands are stabilized by hydrogen bonds, as shown in Figure 2-16b. The ratio of amine and anhydride building blocks determines the identity of the molecule that predominantly terminates the chains. When substituting the linear DATP with the 3-fold TAPT, a highly porous disordered network is formed. It is interconnected over large areas of the sample, although the expected hexagonal symmetry can only be observed locally and no long-range order was achieved.

2.1.4. Acetylenic (Glaser-Hay) coupling

In 1869 Carl Andreas Glaser first described the acetylenic coupling reaction linking two alkyne groups in a basic solution with copper and oxygen as catalysts, as depicted in Figure 2-17 [23]. The related Hay coupling, first described by Allan Hay in 1962, has several advantages as compared to the Glaser coupling [24]. The copper-TMEDA complex used is soluble in a wider range of solvents, so that the reaction is more versatile.

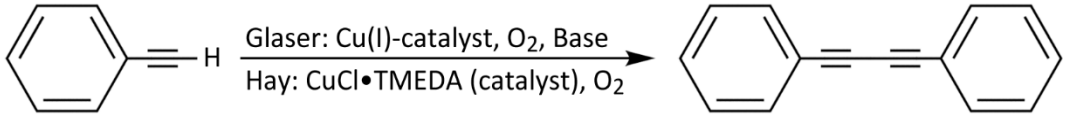

Figure 2-17: Glaser-Hay coupling for the example of ethynyl-benzene.

In 1994 Francois Diederich described a range of different acetylenic polymeric carbon allotropes and carbon-rich networks synthesised using Glaser-Hay coupling reactions [25]. Although the synthesis was still solution based, his research on carbon scaffolding includes one and two dimensional structures, a precursor of on-surface synthesised architectures, some of which are shown in Figure 2-18.

By synthesising tailored carbon allotropes a vast variety of all-carbon structures with varying pore size, stiffness, and stability could be created. However, until 2012 Glaser-Hay coupling was exclusively used for solution-phase synthesis.

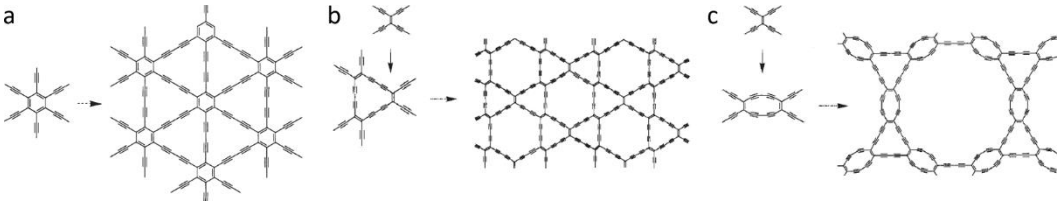

Figure 2-18a: Planar carbon network from hexaethynylbenzene; b: Planar carbon network from tetraethylene via aromatic perethyylated hexadehydro[18]annulene; c: Alternative planar carbon network from tetraethylene via antiaromatic perethyylated hexadehydro[12]annulene [25].

In 2012 Barth and co-workers [26] described the surface-assisted acetylenic coupling reaction of the molecules tri-ethynyl-benzene (TEB) and tri-(ethynyl-phenyl)-benzene (ext-TEB) on Ag(111). The molecules, as depicted in Figure 2-19, consist of a benzene core with ethynyl or ethynyl-phenyl substituents in tri-fold symmetry and form ideally hexagonal networks very similar to the polyphenylene networks described in section 2.1.

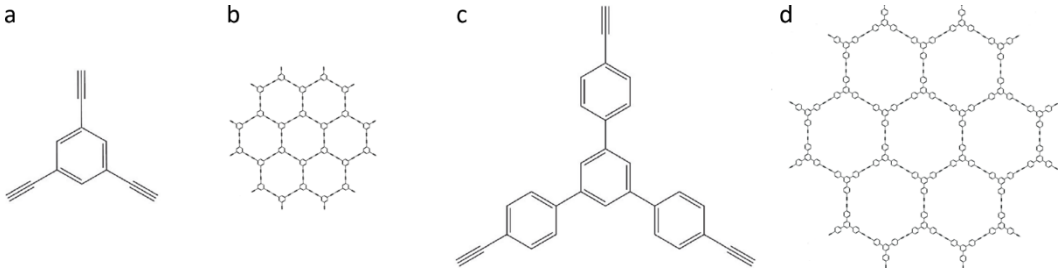

Figure 2-19a: structure of tri-ethynyl-benzene (TEB); b: ideal honeycomb network formed of TEB; c: structure of tri-(ethynyl-phenyl)-benzene (ext-TEB); d: ideal honeycomb network formed of ext-TEB.

The molecules form after deposition onto Ag(111) at low temperatures dense packed self-assembled monolayers as shown in Figure 2-20a and c. Thermal activation combined with a metal substrate catalyst enable Glaser-Hay (acetylenic) coupling with volatile H_2 as the only by-product.

Annealing at relatively low temperatures of 60°C/30°C for TEB/ext-TEP respectively leads to the formation of dimers and small polymeric clusters. The dimers are observed to arrange in small islands of close packed ordered structures co-adsorbed with islands of disordered polymers. Further annealing at 100°C for TEB and 130°C to 250°C for ext-TEB results in the formation of extended disordered polymer networks as shown in Figures 2-20b and d.

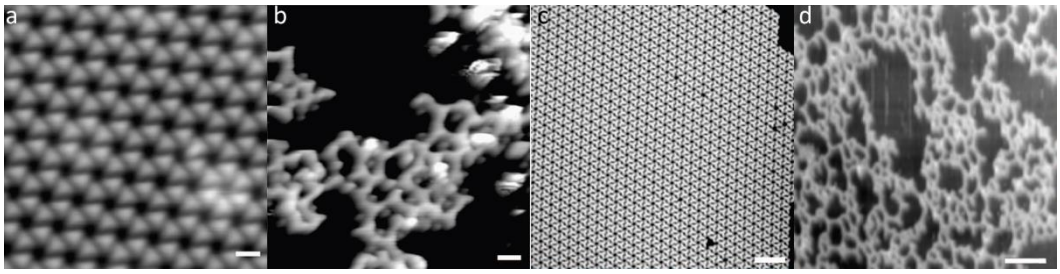

Figure 2-20a: STM image of dense packed TEB molecules at -100°C; scale bar 1 nm; b: STM image of polymerised TEB after annealing at 100°C; scale bar 1 nm; c: STM image of dense packed ext-TEB molecules at -150°C; scale bar 5 nm; b: STM image of polymerised ext-TEB after annealing at 250°C; scale bar 5 nm [26].

The polymers resemble the polyphenylene networks described in sections 2.1.1 and 4.2. However, ethynyl linked polyphenylene networks, as shown in the STM image in Figure 2-20, seem to deviate more from the expected hexagonal pattern than polyphenylene networks formed via Ullmann coupling do [3, 7].

In 2013 Fuchs and co-workers described the formation of π-conjugated linear polymers via Glaser-Hay coupling on metal surfaces [27]. Two different di ethynyl benzene monomers on copper, gold, and silver surfaces were investigated. One is di-(di-ethynyl-phenyl)-di-aryl-benzene (EPAB), the other molecule used is di ethynyl-di-aryl-benzene (EAB), as depicted schematically in Figure 2-21a and b.

The molecules were deposited onto Cu(111), Au(111), Ag(111) at room temperature and investigated with UHV-STM. The molecules form a close packed regular pattern on all surfaces. Upon annealing at about 130°C both molecules polymerise on all investigated substrates. However, the resulting structure differs significantly.

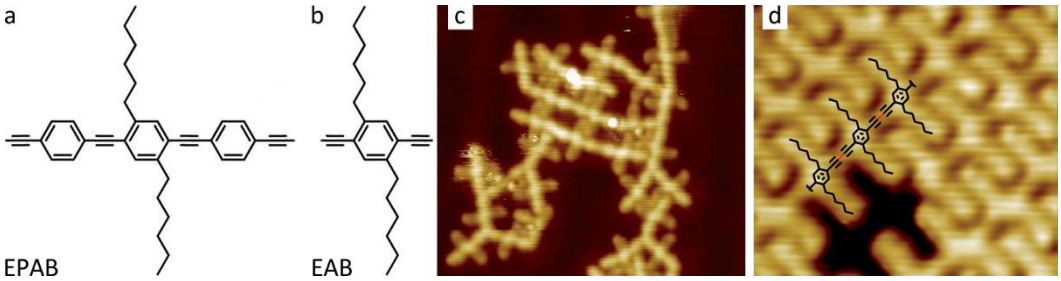

Figure 2-21a: Structure of a di (di ethynyl phenyl) di aryl benzene monomer (EPAB); b: structure of a di ethynyl di aryl benzene monomer (EAB); c: STM image (15 nm x 15 nm) of EPAB on Au(111) after annealing; d: STM image (5 nm x 5 nm) of alkyne on Ag(111) after annealing [27].

The larger EPAB molecule forms short polymerised chains on Au(111) and Cu(111). Other coupling reactions, such as trimerised alkynes, as shown in Figure 2-21c are also observed. On the Ag(111) surface however a much greater selectivity towards the Glaser-Hay coupling of the ethylene linker groups was

observed. The smaller EAB molecules show similar behaviour, although even on a Au(111) surface the polymerisation resulted in short polymer chains with a greater selectivity towards acetylene links compared to the lager EPAB molecule. The best result in terms of long acetylene polymer chains was achieved with the small EAB molecule on Ag(111), as shown in Figure 2-21d. In summary, Glaser-Hay coupling is more efficient on silver surfaces than on gold and copper. The surface possibly mediates the reactions, and the substituents of the organic molecules can influence the frequency of side reactions.

2.1.5. Tautomerisation

Gade and co-workers were first to report the on-surface formation of covalent bonds via tautomerisation on the example of thermally induced one-dimensional polymerisation of tetraazaperopyrene (TAPP) on a copper surface [5]. Tautomerisation is a chemical reaction defined by the switching of an organic compound between two constitutional isomers. This reaction typically results in the formal migration of a hydrogen atom or proton together with a switch of a single bond and adjacent double bond, as depicted in Figure 2-22a.

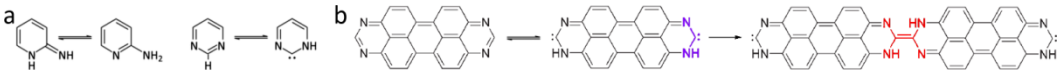

Figure 2-22a: Examples of tautomers; left: Imine and amine; right pyrimidine and diazacyclohexatriene-ylidene; b: Tautomerisation of tetraazaperopyrene (TAPP) and the formation of a dimer linked via a tetra amino ethylene bond (red) coupling two ylidene functional groups (purple).

The covalent coupling reaction of TAPP is shown in Figure 2-22b. The tautomer with the ylidene (purple) functional group polymerises through tetra amino ethylene linkages (red). The coupling of carbene intermediates following the tautomerisation of N-heterocyclic end units is called a Wanzlick-type dimerization [28]. DFT calculations show that the tautomer containing the

ylidene groups is energetically unfavoured. The coupling process however is exothermal so that the overall process is thermoneutral.

Deposition of the TAPP molecules onto a Cu(111) substrate and subsequent annealing at 150°C leads to a metal-coordinated open-porous square network as shown in Figure 2-23a and b.

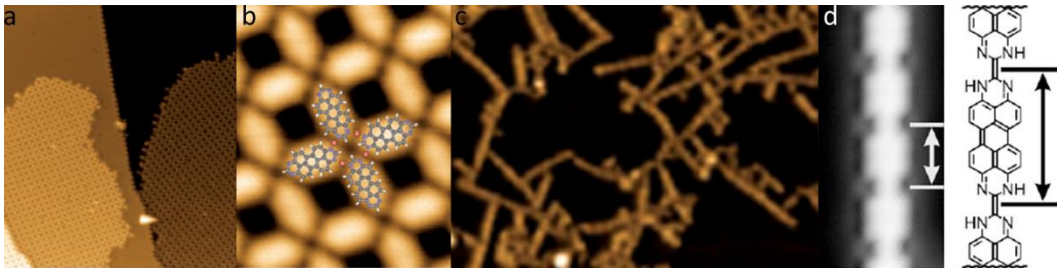

Figure 2-23a: STM image of a submonolayer of TAPP on Cu(111) after annealing at 150°C; b: Zoom of (a) with proposed structure of the metal-coordinated network; c: STM image of polymer chains of TAPP on Cu(111) after annealing at 250°C; d: High resolution STM image and schematic model of a TAPP polymer chain, the distance between the monomers was determined to be 1.23±0.12 nm (STM) and 1.27 nm (DFT, in gas phase) [5].

Annealing the substrate to 250°C induces the formation of extended TAPP polymer chains, as shown in Figure 2-23c. High resolution STM images, as shown in Figure 2-23d, allow for determination of the bond length between adjacent TAPP subunits in the polymer chain. The authors find a distance of 1.23±0.12 nm, which agrees well with their DFT calculated bond length for TAPP oligomers in the gas phase of 1.27 nm.

2.2. Porphyrin

2.2.1. Porphyrin monomers

Porphyrins are heterocyclic macrocycle organic dyes consisting of four pyrrole rings that are linked via methine groups. The most basic porphyrin structure, porphine, is depicted in Figure 2-24a.

The structure supports a stable configuration of single and double bonds with two different sites suitable for substitution that exhibit different reactivity [29]. Positions 2, 3, 7, 8, 12, 13, 17, and 18 are called β-pyrrole positions and are widely substituted in natural products. Positions 5, 10, 15, 20 are called *meso* positions. *Meso* substituted porphyrins have no counterpart in nature and were developed as functional artificial compounds in the 1930s [30]. The porphyrin macrocycle has 22 delocalized π-electrons. This makes it an aromatic compound according to Hückel's 4n + 2 rule for aromaticity [31]. Therefore porphyrins usually exhibit intense absorption bands and are of dark colour. Porphyrins and its derivatives are important building blocks in the metabolism of living organisms. Prominent examples are heme, as depicted in Figure 2-24b, the cofactor of the protein haemoglobin, that gives blood its characteristic red colour and chlorophyll, shown in Figure 2-24c.

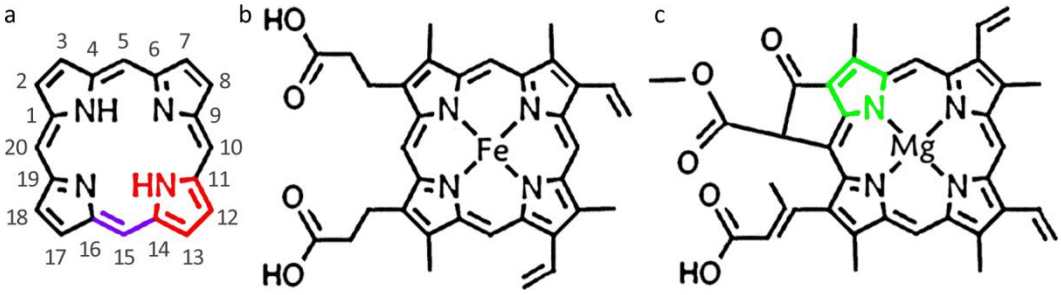

Figure 2-24a: Structure of porphine, the simplest porphyrin with numeration; a pyrrole subunit is marked in red, a methine bridge is marked in purple; b: Structure of the heme B group of haemoglobin; c: Structure of chlorophyll c2, a porphyrin derivate in which one of the pyrrole subunits is replaced by a pyrroline (green).

Chlorophyll is an example of a porphyrin derivate with one of the pyrrole subunits replaced by a pyrroline. Figure 2-24 also shows that the free base porphyrin macrocycle can bind metal ions in its centre to form metal complexes. The chemical properties of the substituents control the water or solvent solubility of the porphyrins.

In 1935 Paul Rothemund [30] developed the basis of modern porphyrin synthesis. The Rothemund synthesis has pyrrole and benzylaldehyde as basis, these compounds react in a sealed bomb at 150°C for 24 h to form tetra-phenyl-porphyrin (TPP), as shown in Figure 2-25a.

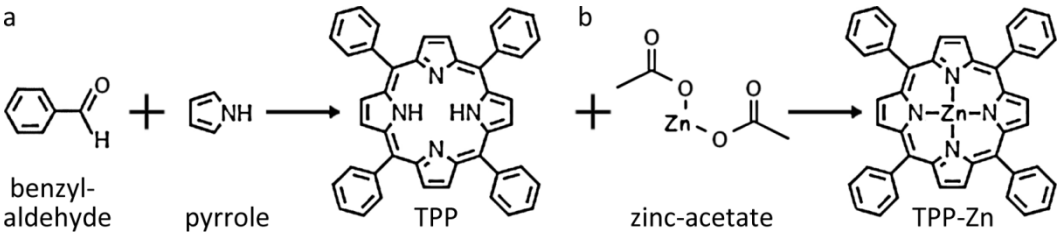

Figure 2-25a: Synthesis of free-base tetra-phenyl-porphyrin (TPP) from benzylaldehyde and pyrrole; b: further reaction to tetra-phenyl-porphyrinato-zinc (TPP-Zn) with zinc acetate.

Unlike natural porphyrins, TPP is substituted at the *meso* carbon positions, and hence the compound is sometimes called *meso*-tetraphenyl porphyrin. The synthesis was later modified by Adler and Longo in 1967 [32]. Their high-temperature approach increased the yield by about 30% and decreased the reaction time from 24 h to 30 min.

The synthesis was optimized by Marguerettaz and co-workers in 1987 [33]. They developed a two-step room-temperature synthesis to enlarge the number of aldehydes exploitable for the synthesis, allowing for a much greater variety in porphyrins available. Even though they decoupled condensation and oxidation in their synthesis, the educts remain aldehyde and pyrrole.

To add a metal (II) ion to the centre of the porphyrin macrocycle, hydrated acetates or other acids of the chosen ion are commonly used [34], i.e. Zn (II) acetate as shown in Figure 2-25b. The –R of the aldehyde can be modified and tailored to synthesize a variety of different monomers as described in sections 4.3, 5.3 and 7.

2.2.2. Synthesis of porphyrin oligomers

Two or more porphyrin monomers can be connected via different linkers to form well defined macromolecules [35]. The synthesis of oligomers out of the monomer building blocks uses templates to arrange the monomer components before linking them covalently to form complex structures. An example of how the synthesis works in general is shown in Figure 2-26.

Figure 2-26: Formation of a trimer from three monomers and a template with three binding sites; first the molecules bind to the template, next covalent coupling of the monomers is induced, finally the template is removed.

In the example in Figure 2-26 a template with three binding sites (black) is used in combination with monomer building blocks (red). Three building blocks attach to the template, typically via metal coordination or weaker interactions in a reversible process. Depending on the specific system, covalent coupling of the monomers is induced thermally and/or with a catalyst. After covalent coupling of the monomers into a trimer (purple), the template may be removed using solvents leaving the polymer isolated.

The formation of small porphyrin oligomers via butadiene linker groups was first described by Sanders and co-workers in the early 1990s [36, 37, 38]. They extended the concept of guest molecules as templates for the formation of complex host structures to ligand-templated synthesis.

Figure 2-27 shows early work done on the synthesis of porphyrin oligomers. The authors differentiate between positive and negative templating. A negative template encourages intermolecular coupling with the target result of extended linear macromolecules. Positive templating on the other hand facilitates intramolecular coupling, which usually results in the formation of cyclic macromolecules. On the example of the synthesis of a dimer, as depicted in

Figure 2-27b, they show how a scavenger template can increase the yield of the dimer, while synthesising the potentially useful cyclic molecule.

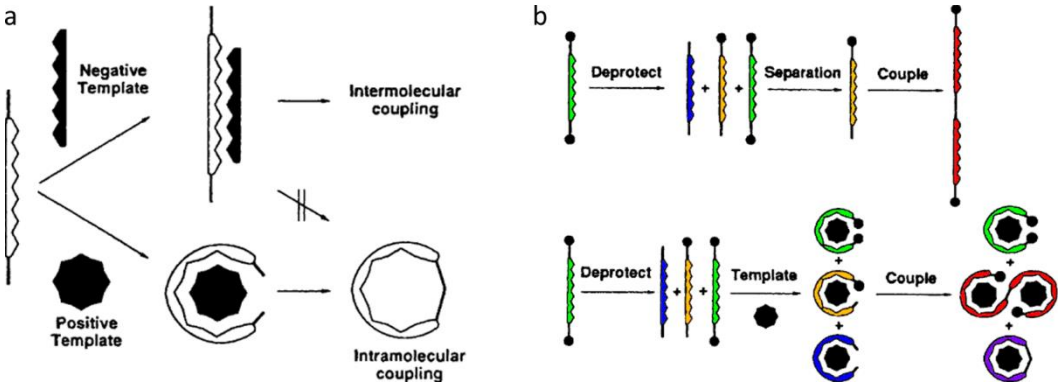

Figure 2-27a: Schematic illustration of positive and negative templating; b: General strategy for the formation of a linear dimer (red) from a symmetrically protected monomer (green); deprotection leads to a mixture of di-reactive monomers (blue), semi-protected monomers (orange) and residual fully protected monomers; a scavenger template (black) induces molecules with two reactive ends to cyclise (purple), increasing the yield of mono-protected material for dimerization [37].

The educt molecule (green) has two protecting groups at opposite ends to prevent initial polymerisation. Upon deprotection a mixture of molecules with two reactive ends (blue), molecules with one reactive and one protected end (orange), and molecules remaining fully protected is formed. The target molecule – a dimer (red) – is only formed when two mono-protected molecules react. However, the presence of fully deprotected molecules leads to a complex mixture of oligomers with only low numbers of the desired dimers. To prevent the oligomerisation from happening the authors introduce the use of a scavenger template. Before intermolecular coupling is initiated, the scavenger templates cause the doubly reactive molecules to cyclise (purple). Subsequently intermolecular coupling causes the mono-protected monomers to form dimers. The resulting products of the reaction can easily be separated because they

consist predominantly of protected and cyclic monomers and the heavier dimers.

Using this concept Anderson and co-workers developed the synthesis of butadiene linked porphyrin oligomers using Glaser-Hay coupling (see section 2.1.4). The nature of the template directs the synthesis of cyclic porphyrin oligomers with 2, 3, or 4 porphyrin subunits as shown in Figure 2-28.

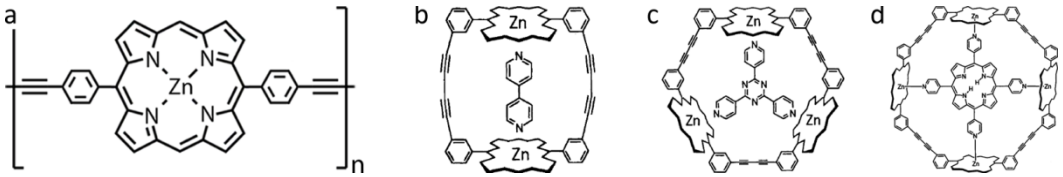

Figure 2-28a: Structure of the porphyrin monomer used for the synthesis of (b), (c) and (d); b: Structure of a cyclic porphyrin dimer around a bipyridine; c: Structure of a cyclic porphyrin trimer around a tri pyridine triazine; c: Structure of a cyclic porphyrin tetramer around a tetra-pyridine-porphyrin [38].

Acetylenic (Glaser-Hay) coupling is chosen for its controllable reactivity, selectivity, and lack of side reactions. The non-covalent self-assembly of template and porphyrin building blocks controls the conformation of porphyrin based molecular wires. The template directed synthesis of butadiyne linked porphyrin oligomers is facilitated by pyridine-zinc ligation. Therefore templates of a chosen symmetry and geometry are synthesised with terminating pyridine ligand groups that form a complementary coordination with the zinc atom at the centre of the porphyrin. After the complex is formed oxidative coupling of porphyrin under palladium/copper catalysis results in butadiene-linked oligomers. Subsequently the template is removed using pyridine or similar amines [38].

Later, in the mid-2000s Anderson and co-workers described the synthesis of larger porphyrin nanorings by bending molecular wires around six and eight-spoked templates respectively as depicted in Figure 2-29 [39, 40].

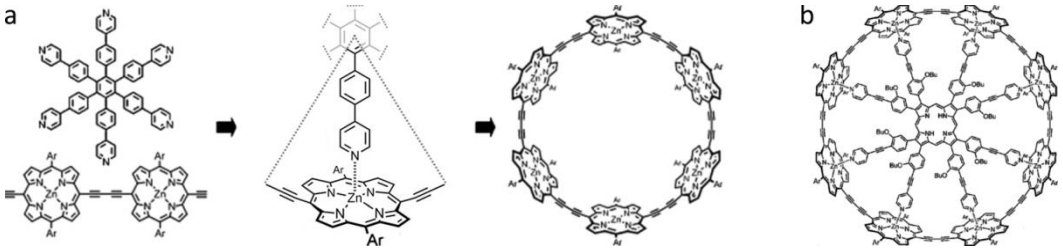

Figure 2-29a: Formation of a 6-membered porphyrin nanoring from a hexa (pyridine phenyl) benzene template and porphyrin dimers [39]; b: 8-membered porphyrin nanoring around a complex octadentate template with a β-pyrrole substituted porphyrin core [40].

The template molecules used for the synthesis of these larger nanorings were specifically designed to accommodate for the expected dimensions of the oligomer. The template for the six-membered nanoring is hexa-(pyridine-phenyl)-benzene, where the nanoring follows the natural symmetry of the benzene core. The template for the eight-membered nanoring is based on a β-pyrrole substituted porphyrin with pyridine terminated branches. The resulting belt-shaped porphyrin nanorings exhibit strained π-conjugation, similar to their natural counterparts, the bacterial light harvesting complex LH2 or light-harvesting chlorophyll arrays [39].

Linking porphyrin monomers into even larger and more complex macromolecules is a challenging task for organic synthesis. A limiting factor of the method described above is the availability of the templates. The synthesis of large enough, rigid, and stable templates becomes synthetically difficult itself and thus the formation of molecules built of monomeric or dimeric building blocks is capped at few-member oligomers. To solve that problem Anderson and co-workers introduced the use of Vernier complexes as a route to the synthesis of large, well defined molecules out of relatively small building blocks, which can readily be synthesised using conventional templating methods.

Vernier systems use the concept of moiré patterns for the synthesis of large monodisperse macromolecules. A moiré pattern occurs when two non-

commensurate periodic structures are superimposed. For Vernier systems in organic synthesis the mismatch is usually tailored so that the lowest common multiple of both periodicities is an integer number within the same order of magnitude as the template and the molecular building block, as depicted schematically in Figure 2-30.

Figure 2-30: Formation of a molecular 4:3 Vernier complex from a trimeric molecular building block (red) and a tetrameric template (black).

For example, in the case of Figure 2-30 the number of binding sites on a small Vernier template (black), 4, is not a multiple of the number of binding sites on the molecular building block (red), 3, resulting in a number of binding sites in the macromolecule equal to the lowest common multiple of both: 12.

The first example of a molecular Vernier was described by Bregant and co-workers in 1998 [41]. They used molecules as shown in Figure 2-31. They combined dicarboxylate with triguanidium to synthesise a pentameric macromolecule. In this synthesis both educt molecules are part of the target macromolecule, unlike conventional templating methods there is no reusable template facilitating the reaction.

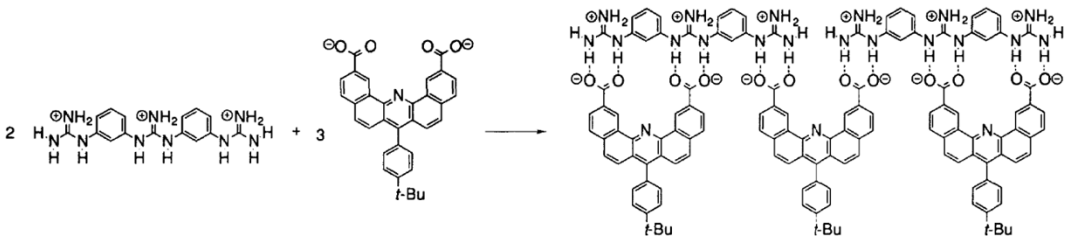

Figure 2-31: Molecular details of the Vernier and its subunits; tribenzonate salt and dicarboxylic acid form a pentamer (2:3) Vernier complex via hydrogen bonding [41].

Vernier formation was found to proceed until all of the limiting component was used up and gave >95% yield independent of the stoichiometry of the two components.

Combining the Vernier templating method with their earlier work on porphyrin oligomer formation [39, 40], Anderson and co-workers have synthesised a range of linear and circular porphyrin oligomers [42, 43], some are shown in Figure 2-32.

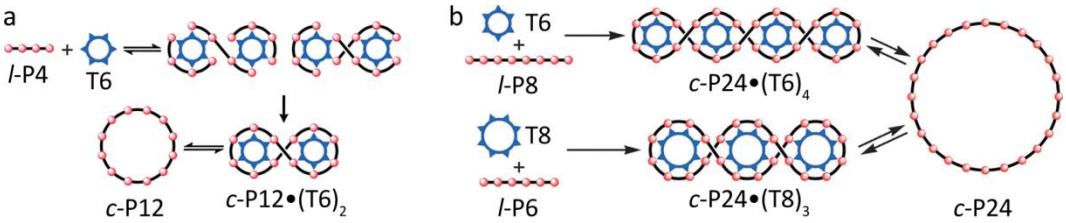

Figure 2-32a: Vernier-templated synthesis of a c-P12 porphyrin nanoring using linear 4-membered porphyrin chains (l-P4) and a 6-membered circular template (T6) [42]; b: two different approaches to a Vernier-templated c-P24 porphyrin nanoring; top: 8-membered linear porphyrin oligomers (l-P8) combined with 6-membered cyclic templates (T6); bottom: 6-membered linear porphyrin oligomers (l-P6) combined with 8-membered cyclic templates (T8) [43].

Anderson and co-workers synthesised cyclic porphyrins consisting of up to 50 porphyrin subunits, and linear porphyrin chains with up to 12 porphyrin subunits. Some of these porphyrins will be investigated in Chapters 6 and 7 using STM and Raman spectroscopy.

2.2.3. Porphyrin and spectroscopy

Porphyrins play an important role in nature due to their distinct absorption, emission, charge transfer and complexing properties because of their characteristic aromatic ring structure of conjugated double bonds [44].

That the deep colour of porphyrins originates in the highly conjugated π-electron system was discovered in the early days of research into these systems

[45]. An interesting feature of porphyrins is their characteristic UV-visible spectrum and its two distinct absorption regions, as shown in Figure 2-33a. Porphyrins display a very intense band in the 350 – 450 nm range, the so-called B-band or Soret band, named after its discoverer Jacques-Louis Soret [46]. A Soret band is an intense peak in the blue wavelength region around 400 nm. It is very common in porphyrins and their compounds and originates mainly in an electron dipole movement allowing a π-π* transition. Around 450 – 700 nm in the visible region between two and four weaker peaks can be observed, the so-called Q-bands. In porphyrins the Soret band corresponds to the ground state to second excited state ($S_0 \rightarrow S_2$) transition and the Q band corresponds to the ground state to first excited state ($S_0 \rightarrow S_1$) transition.

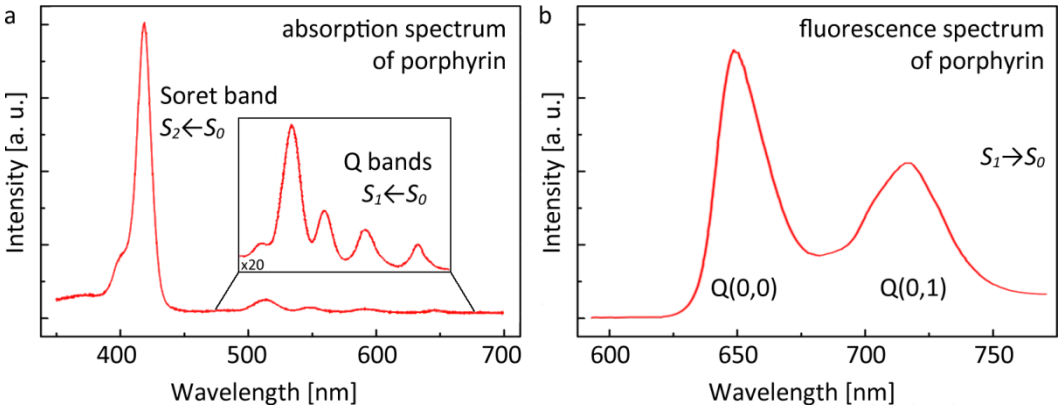

Figure 2-33a: Absorption spectrum of free-base tetra phenyl porphyrin [47]; b: Fluorescence spectrum of free-base tetra phenyl porphyrin.

In the 1930s Fischer and co-workers showed that the location, intensity and number of those bands are related to the core and substituents of the porphyrin [48]. The range and intensity of the Soret band depends on both the core (free-base or metal) and whether the porphyrin is β- or *meso*-substituted. The general shape of the Q-band is predominantly influenced by the core of the porphyrin. Porphyrins with a metal core have a higher symmetry than free base porphyrins resulting in a simplification of the Q band patterns. Minor changes in the location and intensities of the Q band shifts are influenced by the nature of the ligands of the porphyrin [49, 50].

Gouterman proposed a four-orbital model in the 1960s to explain the absorption spectra and their differences, as shown in Figure 2-34a [51].

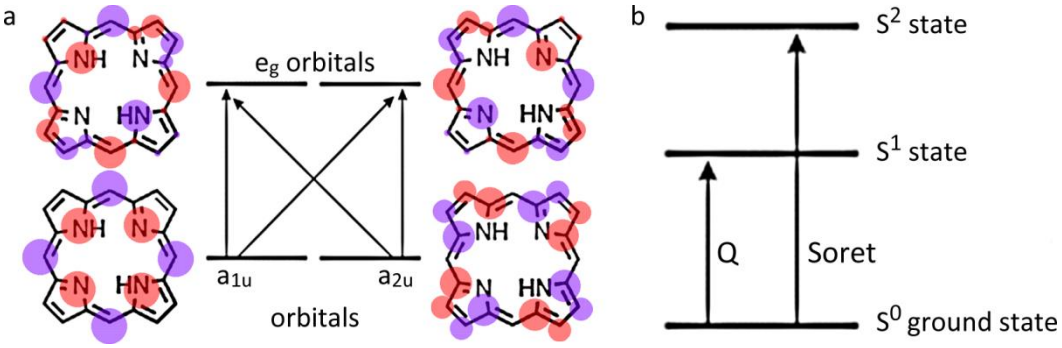

Figure 2-34a: Orbital diagram showing possible transitions for porphyrins; b: State diagram showing possible excites states for porphyrin leading to Soret- and Q-bands.

He attributed the absorption bands to transitions between two HOMOs and two LUMOs. The identity of the metal centre of the porphyrin macrocycle and its substituents affect the relative energies of the transitions. The HOMO was calculated to comprise the a_{1u} and a_{2u} orbitals and the LUMO was calculated to consist of two degenerate e_g* orbitals. π-π* transitions from the HOMOs to the LUMOs results in two excited singlet states S_1 and S_2, as shown in Figure 2-34b. The model was later refined by Baker and co-workers. The authors attribute Soret absorption to an a_{2u}→e_g transition and the Q bands to a_{2u}→e_g transitions. They ascribe the high intensity Soret band transition to a stereoelectronic effect [52]. Shifts in the Soret band are influenced significantly by the metal ligand distance of metalloporphyrins.

Due to the rigid structure of the porphyrin macrocycle, these compounds show strong fluorescence. A typical fluorescence emission spectrum of free base porphyrin shows two strong emission bands in the red region of the electromagnetic spectrum. The emission originates in the S_1→S_0 transition [53, 54]. The dominant features of the fluorescence spectrum of Figure 2-33b are the Q(0,0) and Q(0,1) peaks, which are located at about 650 and 720 nm. Extensive

research on the fluorescence of porphyrins and their derivatives over 80 years shows that the intensity, shape, and location of the emission bands in the spectrum can vary significantly and depends on a variety of factors. Holmes-Smith and co-workers studied the fluorescence emission spectra of different porphyrins [55]. The intensity and position of the peaks depends on the core and substituents of the porphyrin. Metalloporphyrins are blue-shifted compared to their free-base counterparts, as are β-pyrrole substituted porphyrins. The relative intensities of the two bands vary with the chemistry of the substituents, in agreement with earlier studies reported by Connolly and co-workers [56]. They also find that the wavelength influences the fluorescence lifetime and thus the intensity of the bands, but not the position of the Q(0,0) and Q(0,1) bands.

Lindgren and co-workers investigated dendrimer substituted porphyrins [57]. They find that substitution of the *meso* positions with long acid dendrimers leads to a broadened Q(0,1) band and the appearance of shoulders and new bands around the Q(0,1) band. The authors attribute this to strong vibronic interaction and increased Jahn-Teller distortion of the porphyrin core. This effect is more severe for metalloporphyrins since they are originally of higher symmetry than free-base porphyrin. Some substituents, for example furyl groups in the meso-positions, result in a significant red-shift of the Q(0,0) band and disappearance of the Q(0,1) band into the shoulder of the Q(0,0) band, as reported by Ravintash and co-workers in 2007 [58]. Donohoe and co-workers synthesised ethyne-linked tetraarylporphyrin arrays and investigated them with absorption and fluorescence spectroscopy [59]. They find a red-shift of the Q(0,0) band and a relative increase in intensity of the Q(0,1) band in the dimer compared to the monomer building block. In all of the reported studies the porphyrin molecules were dissolved in various solvents, which influences the position and relative intensities of the fluorescence signal as well, as shown by Ion and co-workers [60]. In summary, the presence of a double-peak in the yellow/red region of the electromagnetic spectrum is observed for all investigated porphyrin derivatives, its shape and position is influenced by the core and substituents of the

porphyrin, as well as experimental parameters such as excitation wavelength and solvent.

Aside from UV-vis absorption and fluorescence spectroscopy, there have been several studies focussing on Raman spectroscopy of porphyrins. Porphyrin monomers and their derivatives have a characteristic, although weak, Raman spectrum. Therefore most studies were conducted using resonance Raman (RR) spectroscopy to enhance the resolution of the spectra. Bell and co-workers reported on the RR spectra of tetra phenyl porphyrin in 2003 [61]. They assigned Raman shifts of H_2TPP and its isotopomers in its ground state and excited triplet state to various modes and later verified their findings by DFT [62]. In the late 1980s Bocian and co-workers compared the RR spectra of free-base and zinc porphyrins and assigned observed peaks to specific vibrational modes [63]. They find, analogous to absorption spectroscopy, that metalloporphyrins exhibit a simplified spectrum due to their higher symmetry. The type and location of the substituents on the porphyrin give rise to additional Raman modes depending on their structure. Additionally substituents may change the vibrational properties of the porphyrin macrocycle [64].

In 2000 Bocian and co-workers investigated RR spectra of *meso,meso*-linked copper porphyrin oligomers [65]. They observed a red-shift in some of the existing bands as well as new Raman modes appearing. They attribute those to strong excitonic interactions between neighbouring porphyrins. Osuka and co-workers confirmed this observation. In 2002 they published a RR study on the optical properties of *meso,meso*-linked linear zinc porphyrins range from dimers to extended chains constituted of 128 porphyrin monomers [66]. They find evidence of vibrational splitting originating in the strong excitonic interactions of the porphyrin arrays.

In a similar study, Brédas and co-workers investigated the optical properties of butadiene linked zinc porphyrin oligomers [67]. Those chains exhibit a completely different RR spectrum compared with zinc tetraphenyl porphyrin

monomers, as shown in Figure 2-35. Similar results were published by James and co-workers in 1999 [68]. They investigated porphyrin dimers with different metal cores, the example of a butadiene-linked nickel porphyrin dimer is depicted in Figure 2-35c.

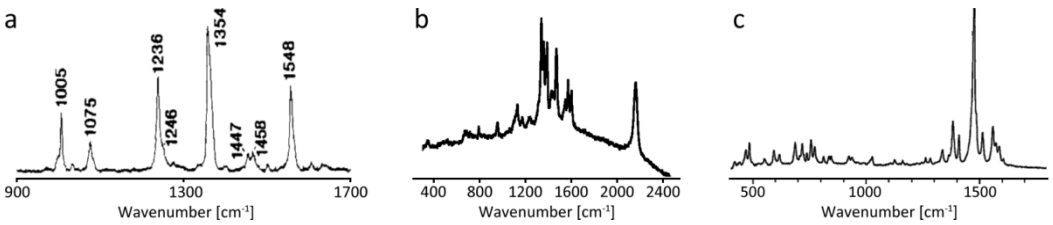

Figure 2-35a: RR spectrum of ZnTPP [63]; b: RR spectrum of a butadiene-linked zinc porphyrin polymer [67]; c: FT Raman spectrum of a butadiene-linked nickel porphyrin dimer [68].

Both spectra of butadiene-linked porphyrins exhibit a range of Raman shifts around 1500 cm^{-1}, accompanied by low intensity features at 700 – 800 cm^{-1}. Similar Raman shifts were observed by Lindsey and co-workers upon investigating a cyclic zinc phenyl porphyrin tetramer linked by ethylene bridges with RR spectroscopy. They find the location of the major Raman shifts located at 1490, 1550, and 1600 cm^{-1} [69].

2.3. Template stripping and transfer printing techniques

The mechanical removal of thin films, molecular layers and nanostructured semiconductors from the substrates on which they are grown has been developed over several decades. In this work the term template stripping is used to describe techniques that aim at removing a target layer from its substrate. The removing medium is also the new substrate of the final layer stack, as depicted in Figure 2-36a. Typically the metal layer is removed using a combination of an adhesive such as epoxy and a support layer. The term transfer printing is used for techniques where the removing medium is only used to transport the transferable layer onto a separate target substrate, as shown in Figure 2-36b.

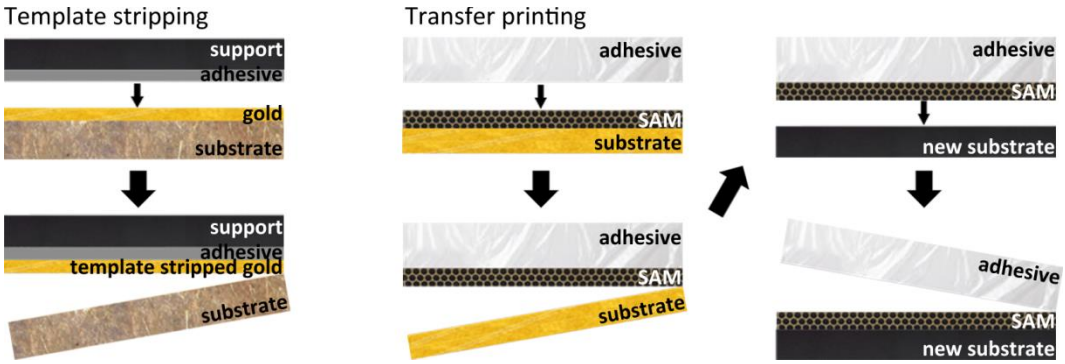

Figure 2-36a: Schematic process of template stripping involving a template stripped gold layer; b: Schematic process forf transfer printing on the example of a transferred self-assembled monolayer (SAM).

Another key difference is that template stripping techniques generally have an ultra smooth metal layer as target, while transfer printing techniques aim at moving semiconductor microstructures, graphene, or self-assembled mono-layers (SAMs) of organic material. In alternative approaches a stable SAM or graphene sheet is transferred without the use of an adhesive by floating it off its initial substrate and placing it onto a target substrate. In this case the adhesive is replaced with a liquid medium.

2.3.1. Template stripped metal surfaces

In early work during the 1990s the focus of template stripping approaches was on the formation of ultra-smooth metal surfaces for the study of thiolate self-assembled monolayers (SAMs). Semenza and co-workers were the first to report on extended atomically flat template-stripped gold surfaces in 1993 [70]. This was achieved by applying epoxy to the top surface of a gold thin film grown on a mica substrate and covering it with a silicon wafer for stability and support. The combined silicon/epoxy/gold layer can then be detached by mechanical peeling, as shown in Figure 2-37a. The roughness of the resulting free surface is comparable with that of the mica substrate. STM images show that the surfaces exhibit a roughness of 0.2 nm over 2 μm^2. Subsequently, a monolayer of thiolate

is deposited onto the template-stripped gold substrate and the self-assembled structures imaged with STM.

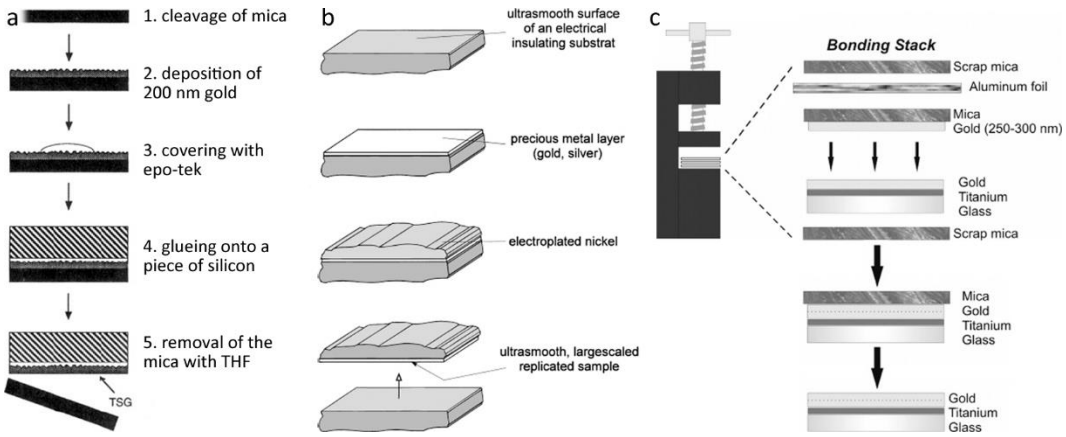

Figure 2-37: Different approaches to template stripping; a: Transfer of thermally evaporated gold from mica to silicon using an epoxy as adhesive [71]; b: Transfer of thermally evaporated gold from insulating substrates like glass, mica, or silicon to electroplated nickel [72]; c: Fabrication of template-stripped gold via diffusion bonding using a titanium adhesion layer [73].

In a continuation of their work Semenza and co-workers show that the epoxy adhesion mediator they first used can be substituted by resin cements in combination with thin interlayers of either tin or titanium to overcome the relatively low adhesion of the ceramics [71]. The advantage of this substitution is that ceramics have a much higher stability in organic solvents compared to epoxy. Disadvantages include a longer preparation time, since these resin cements have to be stripped layer by layer, and a higher cost.

Half a decade later, in 1999 [74], Rabe and co-workers introduced template stripping using electroplated nickel as adhesive and new substrate to strip a polycrystalline 200 nm thin film of Au(111) from a mica substrate as depicted in Figure 2-37b. The advantage of using nickel as adhesive and reinforcement for the gold thin film is the lack of epoxy glue. This leads to an increased chemical and thermal stability combined with a smaller substrate thickness. In 2001 they adapted their technique to produce both crystalline and amorphous surfaces of

gold and silver with varying morphologies and roughnesses by using different substrates (mica, glass, polymer/silicon), substrate temperatures, and deposition rates [72].

Other approaches to template stripping use cold welding or thermal bonding. Blackstock and co-workers reported in 2004 a method for cold-welding extended gold surfaces using silicon wafers to produce template stripped platinum [75]. Hereby the template stripped metal, platinum, is deposited onto a silicon wafer and covered by a titanium adhesion layer and a gold cold-welding layer. An analogous silicon wafer is produced with only the titanium adhesion layer and the gold cold-welding layer. These two layer stacks are then welded together in a hydrostatic press. Cleaving of the top silicon layer exposes an ultra-flat platinum surface.

In 2006 Jacobson and co-workers addressed and improved the main draw-backs of Blackstock's technique in their work [73]. The choice of silicon as template for template-stripped metals is unfavourable compared to mica. The latter yields much improved surface orientation and terracing for the Au layer. Also, the sublimation of different metal layers in vacuum is time consuming and expensive. Figure 2-37c depicts the fabrication of a template-stripped gold layer using thermal bonding. The bonding stack consists of a gold on mica film and a gold on glass film with a titanium adhesion layer. To even the pressure and protect the glass slide in the vice, the stack is enclosed by aluminium foil and additional pieces of mica. After baking the vice assembly for 2 h at 300°C the top mica layer can be removed mechanically and a fresh ultra-flat Au(111) surface is exposed.

2.3.2. Transfer printing

When the adhesive/support layers used in the template stripping process are not the final substrate for the transferred layers, another step, the printing onto a target surface, is introduced. Transfer printing was first used in the early 2000s

to transfer larger molecules like carbon nanotubes or silicon microstructures by covering the transferable objects with a polymer or epoxy, peeling it off the original substrate, and stamping it onto the new substrate.

In 2006 Rogers and co-workers took the principle of template stripped metal surfaces described earlier and applied it to thin ribbon silicon device elements, as shown in Figure 2-38a [76].

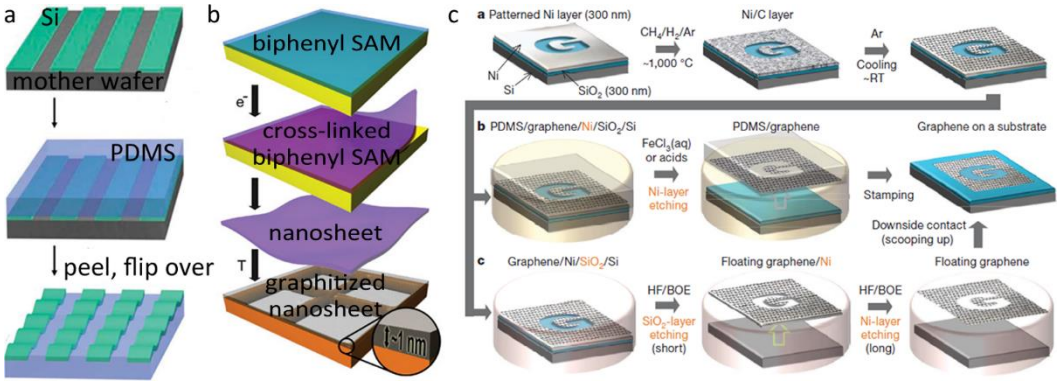

Figure 2-38: Different approaches to transfer printing; a: Template stripping process applied for building stretchable single-crystal Si devices on an elastomeric substrate (PDMS) [76]; b: Fabrication process for ultrathin complementary metal-oxide semiconductors (CMOS) circuits that enable bendability (third frame from top) or stretchability (bottom frame) [77]; c: Synthesis of patterned graphene sheets on a nickel/silicon substrate (top); subsequent etching of the nickel layer with $FeCl_3$ and transfer of the released graphene to a target substrate using PDMS as a stamp (centre); alternatively etching of the silicon oxide and nickel layer using BOE or HF and scooping the floating graphene sheet up with a target substrate (bottom) [79].

They fabricated submicrometer single-crystal silicon devices or complete integrated devices like transistors or diodes on a wafer substrate using conventional lithographic methods. Subsequently these structures were transferred onto an elastomeric substrate, PDMS, via mechanical peeling. This introduces a high level of stretchability and flexibility in the device, an unusual and novel property of high-performance electronic circuits.

Two years later, in a variation of this approach Rogers and co-workers demonstrated that nano- and microstructured semiconductors could not only be removed from a substrate, but also transferred to target specific and more technologically relevant substrates, as depicted in Figure 2-38b [77]. A clean carrier wafer is coated first with a sacrificial layer of polymethylmethacrylate (PMMA), subsequently a thin layer of polyimide (PI) is cast onto a desired layout of silicon nanoribbons to form electronic circuits is then printed onto the polymer layer. The sacrificial PMMA layer can be dissolved in acetone, releasing ultrathin flexible circuits on PI. These can then either be implemented as flexible, free-standing sheets with extreme levels of bendability, or be transferred onto a PDMS later for fully reversible stretchability and compressibility.

In 2009 Gölzhäuser and co-workers demonstrated a process to produce ultrathin conducting carbon nanosheets [78]. They deposit biphenylthiol molecules onto a gold substrate, where they form a regular self-assembled pattern that constitutes a precursor in a pyrolytic reaction [80]. To prevent thermal desorption before the pyrolytic reaction can take place, the molecules are cross-linked by electron irradiation with electron beam lithography. This has the advantage that any pattern can be applied and thus the size and shape of the final conducting graphitic nanosheet may be controlled. The self-assembled molecules form a molecular sheet that is thermally stable. These sheets are transferred by application of a polymeric transfer medium and subsequent dissolution of the gold substrate. The polymer with the attached nanosheet is then applied to another substrate, for example a TEM grid, and the polymer is dissolved leaving the nanosheet exposed on the target substrate. Upon thermal activation at 500°C to 1000°C the molecular sheet is transformed into a stable, conducting graphitic nanosheet.

Most recently the transfer and removal of monolayer films has been widely adopted by graphene researchers through exfoliation and, for samples grown by chemical vapour deposition, by etching the underlying metal thin film or foil

used as a growth substrate. Hong and co-workers developed two different approaches to the formation of patterned graphene films and transfer to arbitrary substrates, as shown in Figure 2-38c [79]. Patterned graphene sheets are grown on a Ni/Si substrate using conventional methods, where the pattern of the nickel layer determined the pattern of the resulting graphene sheet. Subsequently PDMS is deposited onto the graphene and the nickel is etched using aqueous $FeCl_3$ or similar acids, releasing the PDMS/graphene sheet. The patterned graphene sheet may then be stamped onto an arbitrary substrate.

Alternatively, avoiding the use of PDMS, the SiO_2 layer within the graphene/Ni/SiO2/Si sandwich is etched in a buffered oxide etchant (BOE) or hydrogen fluoride (HF), releasing a floating graphene on nickel layer. Longer etching dissolves the nickel layer and the floating graphene sheet can be scooped up with a target substrate.

An alternative method of transferring graphene is depicted schematically in Figure 2-39 [81].

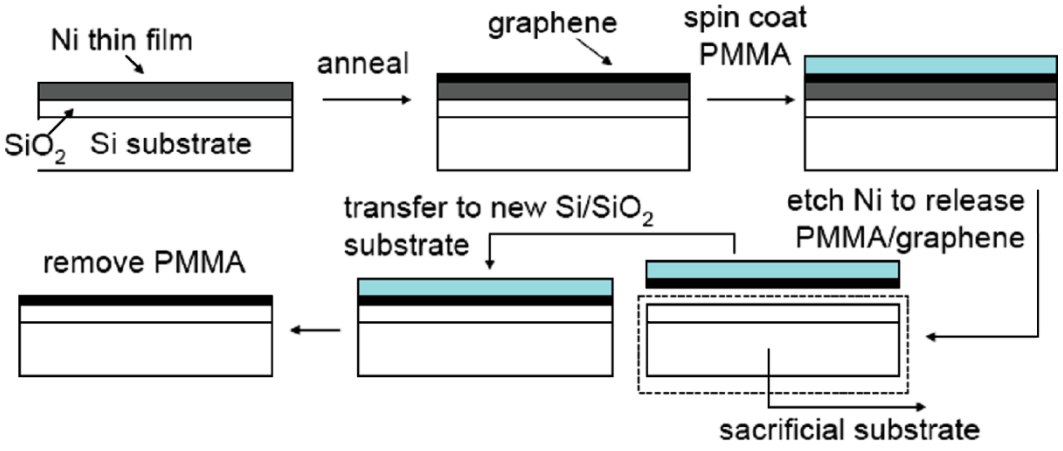

Figure 2-39: Schematic process of the formation of graphene on nickel and subsequent transfer to a separate substrate [81].

A graphene layer is grown on a nickel substrate by surface segregation and controlled cooling [82]. Subsequently, a PMMA support is spin-coated onto the graphene. The PMMA/graphene layer is released from the silicon substrate by

etching of the nickel thin film in $FeCl_3$. The PMMA/graphene is transferred onto a separate surface and the PMMA is dissolved in acetone, leaving the graphene exposed on the new substrate.

Variations of this process were developed Kong and co-workers [83], where the graphene is directly grown on SiO_2/Si and transferred in a similar fashion using PMMA as support and aqueous NaOH is used to etch the SiO_2 layer.

Chapter 3

Experimental techniques

3.1. Introduction

In this chapter, an overview of the experimental techniques used in this work is presented. The basic principles and set-up of the ultra high vacuum chambers used for the experiments is given. Scanning tunnelling microscopy, fluorescence spectroscopy, and Raman spectroscopy are the main techniques used for the experiments. Thus a brief overview of the basic theory and experimental set-up with common examples is given for these techniques.

3.2. Ultra high vacuum and deposition techniques

3.2.1. Ultra high vacuum

A major part of the experiments in this thesis were conducted under ultra high vacuum (UHV) conditions. Ultra high vacuum is defined by a base pressure of 10^{-9} mbar or lower [84]. There are two main reasons why ultra high vacuum is of great importance to many techniques in the field of surface science. A vacuum environment is fundamental for the use of physical vapour deposition of atoms and molecules without interference from gas phase scattering or chemical reaction with residual gas. Two parameters are relevant for typical UHV experiments: the mean free path and the rate at which molecules impinge on a surface in the vacuum system. Both can be calculated by using kinetic gas theory. The mean free path is the mean distance molecules in the system travel before they bump into each other. The mean free path of particles in a molecular beam for deposition should be higher than the distance between source and substrate. The mean free path *l* can be calculated from the kinetic gas theory,

$$l = \frac{k_B T}{4\pi r^2 p}$$

(Equation 3-1)

where *r* is the molecular diameter, *p* is the pressure of the gas and *T* is the temperature.

The mean free path increases with decreasing pressure, as shown in Figure 3-1a. Assuming the distance between source and substrate ranges from a few millimetres up to several decimetres, depending on the experimental set-up, a base pressure of at least 10^{-8} mbar is necessary for the experiment.

Furthermore, to study surface properties at the atomic level, the composition and structure of the surface should be stable during the experiments. Therefore ultra high vacuum is required to obtain a sufficient period of time to investigate the surface. This can be achieved only if a very low number of atoms of the surrounding gas phase adsorb at the surface per time. The rate of impinging molecules *R* is approximated by

$$R = \frac{\sqrt{2\pi m k_B T}}{p}$$

(Equation 3-2)

where *p* is the pressure of the rest gas, *m* is the mass of the molecule, and *T* is the temperature.

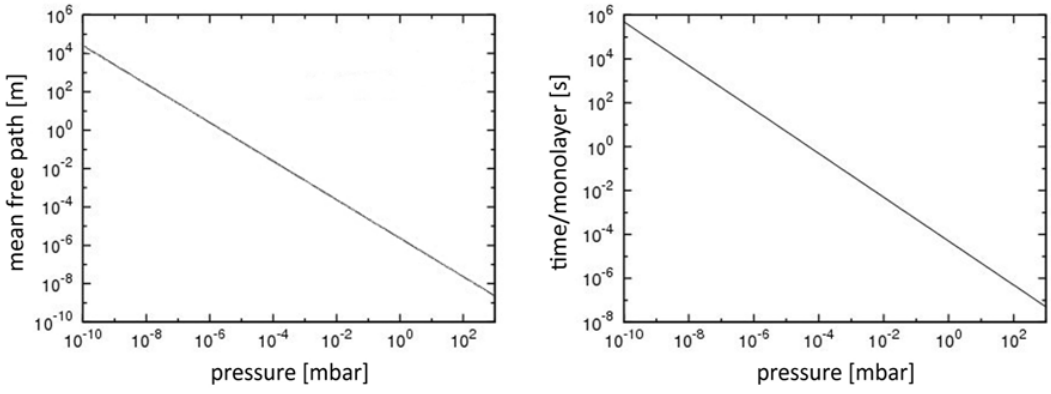

Figure 3-1a: pressure dependence of mean free path; b: pressure dependence of the time needed to adsorb one monolayer with an assumed sticking coefficient of one [84].

From this approximate rate of adsorption one can assume that, at atmospheric conditions and with a sticking coefficient of 1, only nanoseconds

are needed to assemble one monolayer of foreign atoms on a clean surface. Given a time of a few hours for experiments, it becomes obvious why a base pressure of less than 10^{-9} mbar is required, as shown in Figure 3-1b.

The experiments described in this thesis were conducted in two different UHV systems. The experiments on Ullmann coupling (Chapter 3), the UHV steps of the transfer printing experiments (Chapter 4), and the Glaser-Hay coupling experiments (Chapter 7) were performed in the three chamber UHV system 'A123' shown in Figure 3-2.

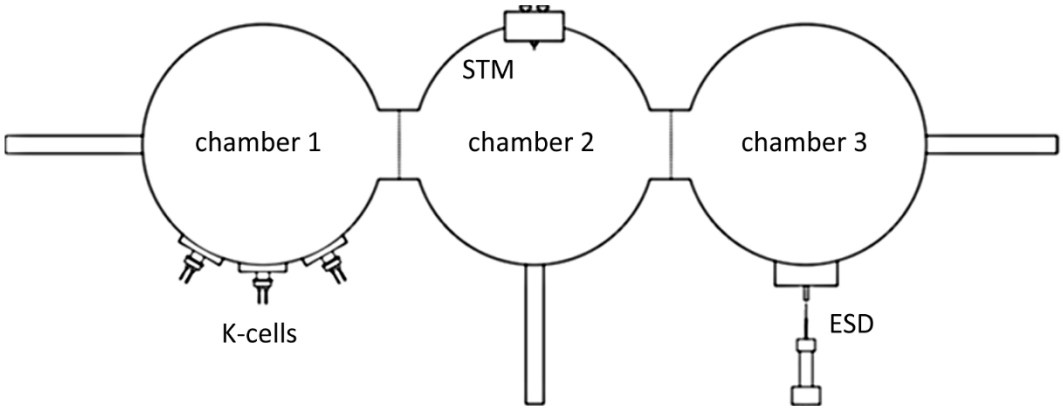

Figure 3-2: Schematic diagram of the 'A123' UHV system; chamber 1 is the main deposition chamber with nine K-cells attached to it; chamber 2 houses the STM; chamber 3 has the electrospray system mounted.

Chamber 1 houses nine Knudsen cells (K-cells), a quartz microbalance, and connections for direct heating of the samples using pieces of silicon. Chamber 2 is the central chamber of the system and is connected via gate valves to chambers 1 and 3 and the top chamber. It houses the STM. An electrospray system and another K-cell can be attached to chamber 3. Above chamber 2 sits the top chamber. It comprises the load lock for sample exchange and includes the facilities for argon sputtering of sample surfaces and electron bombardment of STM tips.

The experiments on molecular trapping in stacked cyclic nanorings (Chapter 6) were conducted in the 'A126' UHV system shown in Figure 3-3. This system is

slightly smaller than 'A123'. It is composed of a preparation chamber and a STM chamber. The preparation chamber houses the electrospray deposition system, two K-cells, a sputter gun, and an electron bombardment set-up for STM tip preparation.

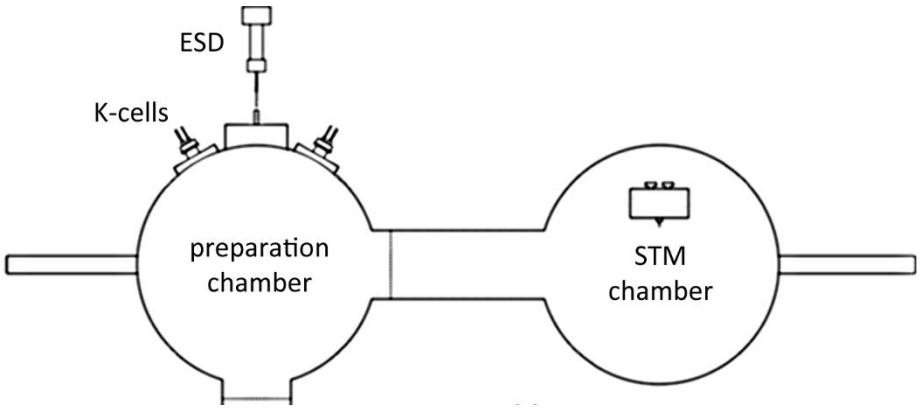

Figure 3-3: schematic diagram of the 'A126' UHV system; the preparation chamber is the main preparation and deposition chamber with the sputter gun, two K-cells, and the electrospray system (ESD) attached to it; the STM chamber houses the STM.

It is also connected to the load lock for sample exchange. The space in between the preparation chamber and the STM chamber contains connections for sample heating. The STM and a carousel for sample and tip storage are located in the STM chamber.

Sample preparation on the example of a Au(111) surface and two different deposition techniques, sublimation from a Knudsen cell and electrospray deposition, will be described in the following sections.

3.2.2. Sample preparation via argon ion sputtering and annealing

The ultra high vacuum experiments in this work were conducted on (111) terminated gold thin films deposited on mica (commercially supplied by Georg Albert GmbH). Pieces with typical dimensions of 0.5 to 1 cm^2 are mounted on the sample holder on top of a piece of highly doped silicon wafer used for

annealing, and loaded into the UHV system. Samples which enter the UHV chamber are contaminated with gases from ambient conditions and thus prepared by repeated cycles of sputtering and annealing before they are used for the experiments [85].

Figure 3-4 depicts schematically the process of argon ion sputtering. Argon atoms are ionised are accelerated towards the surface with a kinetic energy of about 1 keV. This bombardment erodes the top layers of the gold surface along with foreign atoms and molecules adsorbed prior to entering the UHV system.

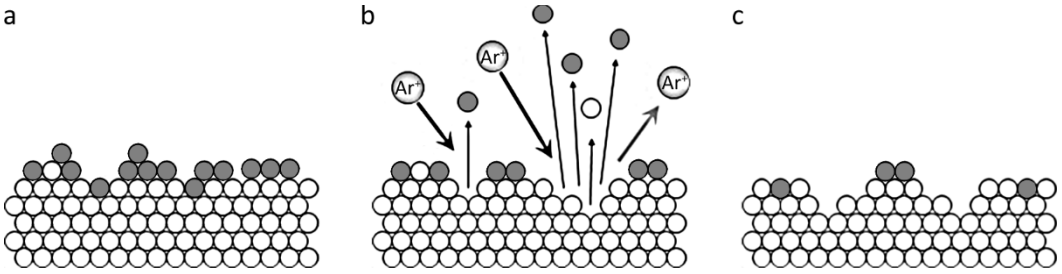

Figure 3-4a: Schematic of the gold surface (white) and adsorbed foreign atoms (grey) after entering the UHV system; b: Argon ion bombardment removes foreign atoms and gold atoms from the top; c: Gold surface after sputtering;

After argon ion bombardment most of the contaminants are removed from the surface. The surface however, is left in an uneven, amorphous state.

To heal the damage caused by sputtering and to desorb embedded argon atoms and other adsorbed contaminants that were not removed during the sputter process, the sample is annealed at roughly 450°C. This causes desorption of foreign atoms, as well as surface reconstruction. Surface reconstruction is the reorganisation of surface atoms with respect to bulk atoms to minimise their surface energy. After repeated sputter-anneal samples the surfaces structure of (111) terminated gold usually shows a (22 x √3) reconstruction pattern. This so-called herringbone reconstruction of the gold surface will be discussed in section 2.3.3.

3.2.3. Deposition via sublimation from a Knudsen cell

In UHV surface science, solid compounds such as organic molecules or metals are typically deposited via sublimation from a Knudsen cell or K-cell, named after M. Knudsen [86]. A schematic diagram of a basic Knudsen cell is shown in Figure 3-5. The material to be deposited is put into a clean crucible typically made of tantalum or boron-nitride located in the head of the K-cell. Once under vacuum, the crucible is heated by passing current through a filament located at the bottom of the crucible to its sublimation temperature. Once the substance reaches its sublimation temperature the molecules or atoms sublime, i.e. they change state from the solid phase directly to the gas phase.

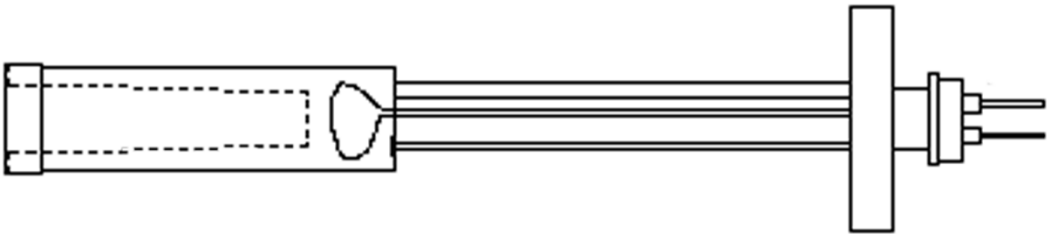

Figure 3-5: Schematic set-up of a Knudsen cell as used in the experiments for deposition of organic molecules

As described earlier, material can travel through ultra high vacuum in straight lines if its mean free path is longer than the distance between the K-cell and the substrate. Molecules or atoms with the correct trajectory will reach upon the sample surface unperturbed. The temperature is kept constant during the deposition using a PID controller to ensure a constant deposition rate.

The main advantage of this deposition technique is that it can be performed under UHV conditions. Therefore the sample surface remains UHV-clean. It also enables precise control over the deposition rate, and the deposition is even across the exposed sample surface.

There are several ways of determining the deposition rate to varying levels of accuracy, and the choice mostly depends on the analytical techniques

available in the UHV system used. For the experiments described in this thesis a combination of quartz monitor and STM is used.

Prior to deposition of material of unknown sublimation temperature the deposition rate was measured via a quartz micro balance [87] located in the UHV chamber. A quartz microbalance measures mass per area by measuring the change in frequency of a quartz crystal resonator. Due to the piezoelectric effect, by applying alternating current to a quartz crystal oscillations are induced. The frequency of oscillation of the quartz crystal is partially dependent on the mass of the crystal. Since all of the other influencing variables remain constant during evaporation experiments, a change in mass correlates directly to a change in frequency.

As material is deposited on the surface of the crystal the thickness increases. Consequently the frequency of oscillation decreases from the initial value. This change in frequency can be correlated to the mass change. Frequency measurements can easily be made to high precision, therefore deposited masses down to a level of below 1 $\mu g/cm^2$ may be measured with this method.

3.2.4. Electrospray deposition

An alternative deposition technique to sublimation from a K-cell in UHV is electrospray deposition (ESD). This method is used when organic molecules that are too big or too fragile for sublimation are to be deposited onto a surface in vacuum conditions.

This technique has its origin in mass spectroscopy. In the 1980s Fenn and co-workers [88] developed electrospray ionization, a method of ionizing molecules in the gas phase without fragmentation. Hereby the molecules in solution are passed through a thin, charged capillary. A jet of highly ionized molecules exits the capillary and is sent through a mass spectrometer.

In the early 2000, this method was adapted for ambient deposition of organic macromolecules such as proteins [89]. Since then the method has been developed at Nottingham and elsewhere to deposit molecules at lower pressures, down to ultra high vacuum set-ups. This allows for deposition and investigation of molecules onto UHV-clean surfaces without contamination from ambient conditions [90, 91].

Figure 3-6 shows the set-up of a 4 stage electrospray deposition system. The molecules which will be deposited are first dissolved in a polar solvent (or solvent mixture) such as methanol. This solvent is then passed through tubing into a hollow stainless steel needle, the emitter. A large positive bias of the order of 2 kV is applied to the emitter, ionizing the solvent molecules passing the emitter. This causes the molecules to repel each other, as well as the emitter and they exit the emitter as a jet of small droplets. While travelling a short distance through air, the droplets split repeatedly into smaller droplets and the jet of droplets becomes a plume of very small droplets.

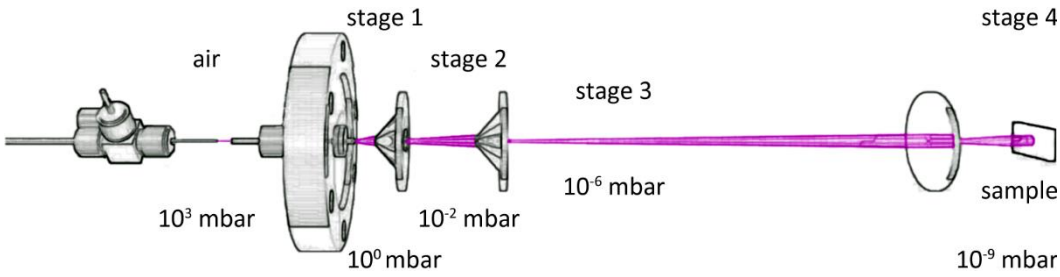

Figure 3-6: Schematic set-up of a 4 stage electrospray deposition system (ESD) showing molecules (purple) travelling from left to right from the emitter onto the sample.

This plume of small droplets (purple in Figure 3-6) enters vacuum. A series of differentially pumped chambers separated by small apertures allows for reduction of pressure from atmosphere down to UHV where the sample is located.

The apertures are aligned so that the solvent and molecules travelling with the correct trajectory pass through the different stages of pressure into the vacuum chamber where they impinge on the sample. Large and fragile molecules are protected by the solution, so they reach the surface mostly without fragmentation or corruption. The deposition spot size on the sample has a diameter of approximately 3 mm with a Gaussian-like spatial distribution of the molecules.

The base pressure in the chamber is 10^{-9} to 10^{-10} mbar. During deposition the pressure may rise up to 10^{-5} mbar. This is due to solvent molecules is the molecular beam. Any residual solvent molecules that are incident on the sample desorb immediately. The surface coverage of ESD can be controlled via deposition time and gas pressure in the UHV chamber during deposition.

3.3. Scanning tunnelling microscopy

The underlying principle of scanning tunneling microscopy (STM) is the quantum mechanical tunneling effect. STM is a method that enables real space imaging of conductive surfaces with atomic resolution. STM experiments are based upon scanning a sample with a conducting tip positioned just above a surface. When a voltage bias is applied across the tip-sample junction electrons can travel across the gap due to quantum mechanical tunneling. Thus the electronic structure of the surface may be imaged by monitoring the tunneling current between the probe and the surface.

STM was the first scanning probe technique developed in 1981 by Gerd Binning and Heinrich Rohrer at the IMB laboratories in Zürich [92]. Other scanning probe techniques such as the atomic force microscope or the near-field scanning optical microscope were developed later in the late 1980s. The main physical principle that enables the functionality of an STM is the quantum mechanical effect of vacuum tunneling. This effect provides the possibility to image the electronic structure of a surface without direct contact.

3.3.1. Quantum mechanical tunneling

The physical principle on which scanning tunneling microscopy is based is vacuum tunneling. A precise theoretical treatment of the tunneling mechanics in an STM experiment is often not possible, as this would require exact knowledge of the sample and tip states. Particularly the shape of the tip at atomic level is unknown for metallic tips, since their structure may change frequently during an experiment.

Therefore different approximations have been developed since the invention of the STM. A simplified quantum mechanical consideration of quantum tunneling sets out from the one-dimensional time-independent Schrödinger equation [93], a differential equation of the wave function Ψ, shown in Equation 3-3,

$$-\frac{\hbar^2}{2m}\frac{d^2\psi}{dx^2} + V(x)\psi = E\psi,$$

(Equation 3-3)

where m is the electron mass, $\hbar$ is Planck's constant, ψ is the time-invariant wave function of an electron, V is the potential energy at position x, and E are the energy eigenvalues. In the case of a constant potential energy barrier of finite barrier height U and width d the wave function of an electron moving in $+x$ direction inside this barrier can be approximated by

$$\psi = Ae^{-\kappa x}$$

(Equation 3-4)

where A is a constant and κ is

$$\kappa = \frac{\sqrt{2m(U-E)}}{\hbar}.$$

(Equation 3-5)

This wave function penetrates the potential energy barrier and decays exponentially therein. Therefore at the other side of the barrier a rest of the original wave emerges, as depicted schematically in Figure 3-7, showing a one dimensional quantum tunnelling through a finite barrier of width *d* and height *U*.

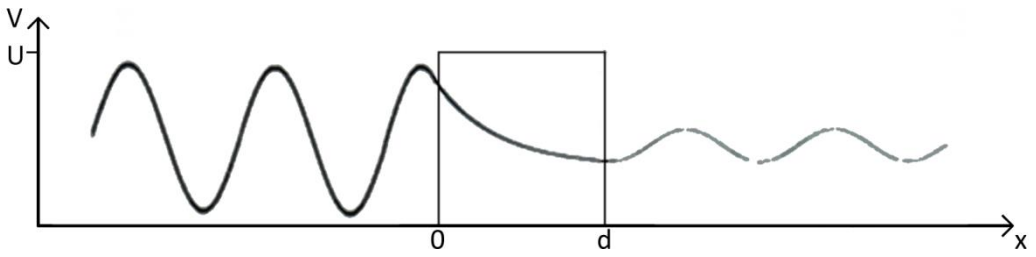

Figure 3-7: Schematic depiction of one dimensional quantum tunnelling through a finite barrier of width d and height U.

The square of the absolute value of the wave function depicts the transmission probability of a particle at position *d*,

$$|\psi|^2 \sim e^{-2\kappa d},$$

(Equation 3-6)

thus there is a finite, non-zero probability for a particle to be on the other side of the potential energy barrier. The energy of the tunneled particle remains the same, only the quantum amplitude and hence the probability of the process is decreased. Quantum tunneling is an effect generally considerable at extremely short range and short time intervals.

Taking the approximation one step further towards an actual STM set-up, the basic features of two metals in close proximity can be considered. Figure 3-8 depicts schematically the relative energies of the Fermi levels of both materials when they separated (a), in close proximity (b), and in close proximity with a voltage bias applied across the junction (c).

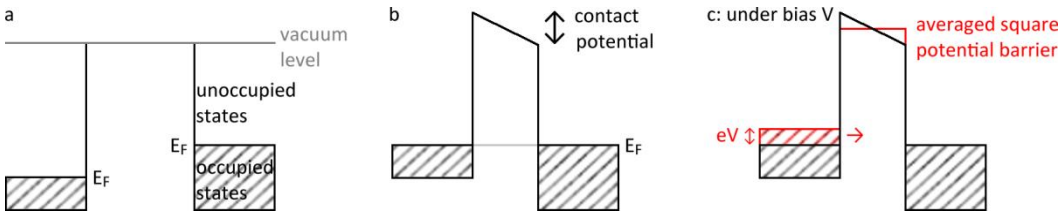

Figure 3-8: Schematic diagrams of the energy levels of two materials brought into close proximity of each other; a: Initially the two materials are separate and their Fermi levels differ; b: The materials are brought into close proximity, the Fermi levels align, and a contact potential between the two materials arises; c: With voltage bias applied across the junction the Fermi levels are shifted; electrons with energy within eV of the Fermi level (red) have a finite probability of tunnelling into the unoccupied states of the other material.

Applying a voltage bias enables a tunnel current to flow, electrons with energy between E_F and (E_F + eV) can tunnel through the gap into the empty valence band of the other material. The tunnel current arising at small bias voltages can therefore be approximated by

$$I \sim e^{-2\kappa d} n(E_F) eV$$

(Equation 3-7)

where $n(E_F)$ is the local density of states (LDOS) at the Fermi level. The tunnel current shows an exponential distance dependence on the gap between the tip and the surface. In typical materials used for STM the tunnelling current increases by about one order of magnitude for each 0.1 nm the tip is brought closer to the sample.

3.3.2. Tersoff-Hamann theory

Two decades before the invention of the STM, Bardeen presented a method of calculating the tunneling current between two flat metal plates by treating them as two separate systems, rather than attempting to solve the Schrödinger equation for one complex system [94].

Tersoff and Hamann adopted this approach in their theory for STM. They treat the electronic states of tip and surface in close proximity as independent, overlapping entities, using Bardeen's perturbation theory. The formula used to describe the probability of electron transfer from surface μ to tip ν is

$$p = \frac{2\pi}{\hbar}|M_{\mu\nu}|^2\delta(E_\mu - E_\nu),$$

(Equation 3-8)

where $M_{\mu\nu}$ is the tunneling matrix between the states ψ_μ of the surface and ψ_ν of the tip and E_μ and E_ν are the energies of the states ψ_μ and ψ_ν, respectively [93]. The tunneling matrix describes the amplitude of electron transfer and is given as

$$M_{\mu\nu} = \frac{\hbar^2}{2m}\int(\psi_\mu^*\nabla\psi_\nu - \psi_\nu^*\nabla\psi_\mu)dS$$

(Equation 3-9)

with the integral being over an arbitrary surface within the barrier region [96]. Tersoff and Hamann show that when a bias voltage is applied, the tunneling current is given by

$$I = \frac{2e\pi}{\hbar}\sum_{\mu,\nu} f(E_\mu[1 - f(E_\nu + eV)]|M_{\mu\nu}|^2\delta(E_\mu - E_\nu).$$

(Equation 3-10)

Considering only low temperatures (where Fermi functions become unit step functions), small bias voltages and elastic tunneling, Tersoff and Hamann show that Equation 3-10 can be reduced to

$$I = \frac{2e\pi}{\hbar}e^2V\sum_{\mu,\nu}|M_{\mu\nu}|^2\delta(E_\nu - E_F)\delta(E_\mu - E_F).$$

(Equation 3-11)

Tersoff and Hamann further developed a model for the unknown shape of the tip by using an ideally shaped tip to determine the matrix element. They describe the tip as a sphere of radius *R*. Thus the matrix element for materials with equal work functions can be described as

$$M_{\mu\nu} \propto \kappa R e^{\kappa R} \psi_\nu(r_0),$$

(Equation 3-12)

considering only tip wave functions in the s-wave state. Including all these assumptions the tunnel current for small bias voltages can be described as

$$I \propto \sum_\nu |\psi_\nu(r_0)|^2 \delta(E_\nu - E_F) \equiv \rho(r_0, E_F)$$

(Equation 3-13)

where $\rho(r_0,E_F)$ is the LDOS at the apex of the tip at the Fermi level. Thus constant current STM images display the surface LDOS. However, because Tersoff and Hamman's model is based on several approximations, like the lack of interaction between tip and surface or the s-wave-tip model, their theory is not suitable for a quantitative explanation of most STM images, i. e. adsorbed molecules.

3.3.3. Imaging molecules on surfaces

STM investigations on molecules adsorbed on surfaces provide excellent insight to the chemistry and physics of those compounds. The exponential dependence of the tunnel current on distance implies that the adsorbed molecules contribute most to the topograph. Additionally, other effects such as molecular adsorption on the STM tip may give rise to anomalous contrast effects in STM images. Thus, identification and interpretation of the chemical nature of adsorbed molecules based solely on their apparent height with respect to the surface in STM images is not possible.

According to the Tersoff-Hamann theory the tunneling current scales with the LDOS at the Fermi level. In some counterintuitive cases adsorbed atoms or molecules may even appear as depressions on the substrate [97], demonstrating that interpretation of STM data is always an analysis of the LDOS at the surface of the sample.

3.3.4. Experimental set-up

The basic set-up on an STM encompasses a metallic tip, and a piezo element integrated into a feedback loop, as shown in Figure 3-9.

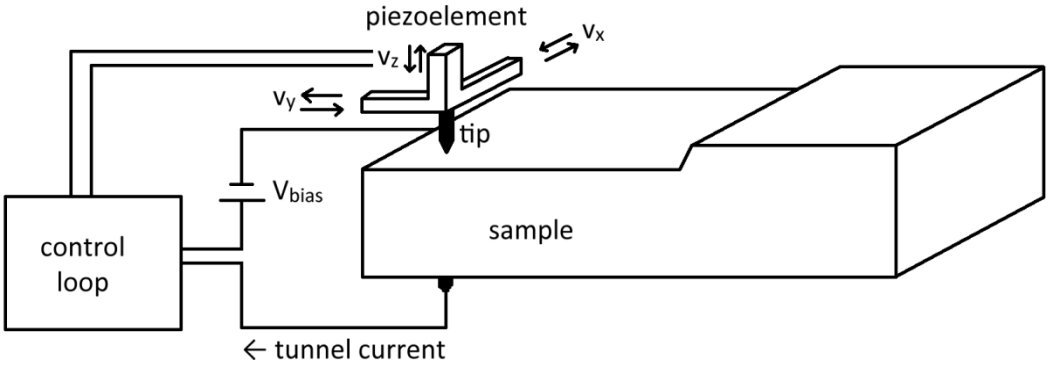

Figure 3-9: Basic scheme of a STM: Bias voltage V_Z is applied to the z piezo actuator to maintain constant tunnelling current via the control loop while the tip scans line by line over the sample surface by changing v_x and v_y.

An atomically sharp metallic tip, usually made of tungsten or platinum-iridium, is brought close to the sample with a gap between surface and tip of less than one nanometer. A small bias voltage (about 1 V) is applied to the surface or the tip so that electrons may tunnel through the gap. The direction of the electron flow is determined by the bias polarity. The vertical and lateral position of the tip is controlled precisely within Ångstrom range via a piezoelectric tube. This is possible because of another important physical principle enabling the use of an STM: the piezoelectric effect.

Piezoelectricity describes the change in electric polarization and therefore an accumulation of charge when mechanical stress is applied. Vice versa such

materials become deformed in presence of an applied electrical field. This is called the reverse piezoelectric effect. The piezoelectric effect is a linear reversible interaction that occurs only in crystalline materials with no inversion symmetry. For STM set-ups the piezo elements are usually made of lead zirconate titanate (PZT), a ceramic perowskite. Using the lateral deformation of the piezoelectric tube, the tip is scanned over an area, generating an image of the LDOS by taking typically 512 x 512 single measurements.

STM can be run in different modes: The constant current mode provides information about the work function of the surface atoms. While measuring the vertical position of the tip as a function of lateral coordinates, the feedback loop constantly monitors the tunneling current and the piezo element adjusts the vertical position of the tip to maintain a constant preset tunneling current. The constant current mode is more reliable when scanning rougher substrates, and the information about topographic height is more reliable.

In constant height mode the vertical position of the tip is constant and the feedback loop is mostly disabled. The current is measured as a function of lateral coordinates and displayed. The constant height mode works well for very flat surfaces so that the tip won't crash into the surface or move too far away for tunnel current to flow measurably. The lack of feedback loop allows for higher scanning frequencies. This is of importance for the investigation of dynamic processes, where STMs that operate at video rates of over 200 frames per second are used [98].

A third mode of the STM is called scanning tunnelling spectroscopy (STS). Thereby the tunneling current as a function of applied voltage (I/V curve) at one point is monitored. This spectroscopic mode enables further insight into the electronic properties of the sample, like the LDOS and band gap at a specific point.

The process of obtaining an STM image in UHV is explained on the example of a (22 x √3) reconstructed Au(111) surface. Typically a 1 cm^2 piece of Au(111) thin film on mica, commercially supplied, is mounted on the sample holder and inserted into the UHV chamber. The sample is subsequently Ar-ion sputtered for 30 min ($1x10^{-5}$ mbar, 0.8 keV, 1 µA) and annealed for 2 h at 500°. A more detailed description of sample preparation in UHV can be found in section 3.2.1. When the sample has cooled down to room temperature, it is moved to the STM and the surface is imaged at constant current mode resulting in a surface conformation as displayed in Figure 3-10. A clean gold surface typically exhibits the so-called herringbone surface reconstruction to minimize the energy at the surface. The atomic arrangement of the gold atoms, as displayed in Figure 3-10b, was first described by Behm and co-workers [100].

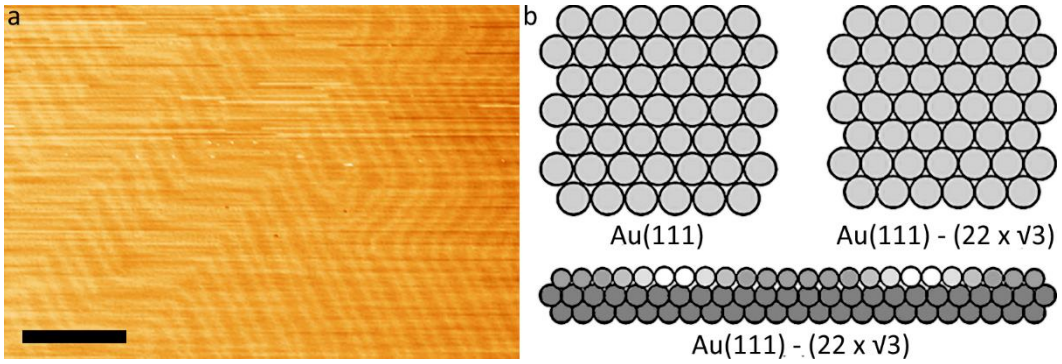

Figure 3-10a: STM image of Au(111) (-1.5 V, 0.05 nA); the apparent herringbone pattern comes from the (22 x √3) surface reconstruction; scale bar: 20 nm; b: schematic model of the atomic arrangement of the (22 x √3) surface reconstruction of the Au(111) surface [99].

The Au(111) surface is to date the only fcc metal surface observed to reconstruct in a (22 x √3) arrangement. The surface undergoes a transition between fcc packing and hcp stacking of the upper atoms on the surface. This causes an atomic corrugation that can be observed with STM. An additional superstructure exists due to a correlated bending of 120° of the corrugation lines approximately every 25 nm, indicating the surface undergoes long range

strain relief. These corrugation lines, which tend to exist in pairs, typically terminate in U-turns, so that no corrugation line ends sharply.

3.4. Spectroscopy

Spectroscopy encompasses a group of methods that investigate the interaction between matter and radiated energy. The basic formula of any spectroscopic method is the correlation between the energy E of a photon and its frequency ν

$$E = h\nu$$

(Equation 3-14)

where *h* is Planck's constant. All spectroscopic methods are based on an energy source, typically electromagnetic radiation or particles, and a spectrometer that measures that energy after its interaction with the sample. There are thus as many types of spectroscopy as there are energy sources, types of material, and nature of interaction, i.e. absorption or scattering. In the context of this thesis fluorescence [101] and Raman [102] spectroscopy will be discussed in more detail.

3.4.1. Fluorescence spectroscopy

Fluorescence is the emission of light following the absorption of a photon. UV-visible absorbance, fluorescence, and phosphorescence are electronic phenomena which occur in molecules having conjugated π-electrons. UV-visible absorbance and fluorescence spectroscopy are complementary, well established qualitative and quantitative methods in analytical chemistry. Since these phenomena involve π-electrons, the energy levels of π-electrons will be explained first with a Jablonski diagram shown in Figure 3-11. π-electrons of molecules can exist in several states. The ground state (S_0) has the lowest energy and electrons typically rest there unless excited. Excited singlet states (S_n) and triplet states (T_n) are states of higher energy. All these energy states (depicted as

thick horizontal black lines) can be divided into various vibrational energy levels within that state, shown as thinner horizontal black lines.

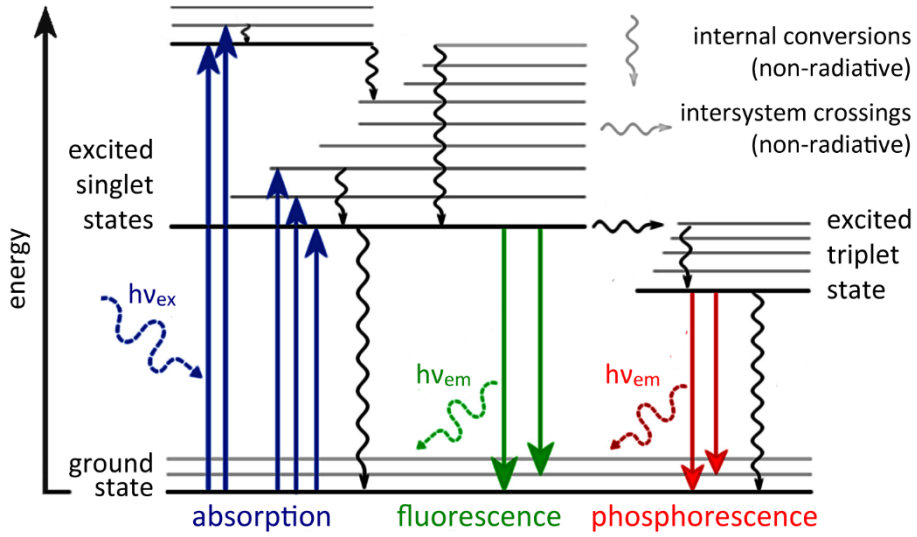

Figure 3-11: Jablonski diagram showing a number of possible routes by which an excited molecule can return to its ground state after absorption; a rapid return from excited singlet states results in fluorescence; a delayed return via unstable excited triplet states results in phosphorescence.

Absorbance, shown in blue in the Jablonski diagram, occurs when radiation energy $h\nu_{ex}$ excites electrons from the ground state to an excited energy state. The excitation is typically described via

$$excitation\text{: } S_0 + h\nu_{ex} \rightarrow S_1$$

(Equation 3-15)

where S_0 is the ground state of the molecule, $h\nu_{ex}$ the excitation energy, and S_1 the molecule's first electronically excited singlet state.

The excited electrons can drop down energy levels within the excited state or back down to a lower excited state or the ground state via non-radiative internal conversions. These are depicted as vertical squiggly lines in the Jablonski diagram. Those internal conversions cause the molecule to lose heat.

Once the electron reaches the lowest level of the excited singlet state S1 via thermal dissipation, fluorescence may occur. Thereby an excited electron relaxes from the lowest level of an excited singlet state to one of the vibrational levels in the ground state, as shown in green in the Jablonski diagram. The emission via fluorescence from an excited singlet state is calculated via

$$fluorescence\ emission: S_1 \rightarrow S_0 + h\nu_{em}$$

(Equation 3-16)

where S_1 is the molecule's first electronically excited singlet state, $h\nu_{em}$ the emission caused by fluorescence, and S_0 the ground state of the molecule. Because the electrons can jump to different vibrational levels of the ground state and each transition has a specific energy and thus frequency, it is possible by analysis of the emission spectrum to determine the structure of the different vibrational levels of the ground state of a molecule.

Phosphorescence, depicted in red in the Jablonski diagram, is related to fluorescence. After electrons are lifted to an excited singlet state, additionally to fluorescence and non-radiative internal conversions, another type of transition can occur. The excited electrons may undergo the less common process of intersystem crossing into a triplet state, depicted by a horizontal squiggly arrow in the diagram in Figure 3-11. An excited triplet state of higher spin multiplicity where the electron becomes trapped since the transition back to the ground state is classically forbidden. In quantum mechanics these transitions will still occur. The equation for emission from phosphorescence is

$$phosphorescence\ emission: S_1 \rightarrow T_1 \rightarrow S_0 + h\nu_{em}$$

(Equation 3-17)

where S_1 is the molecule's first electronically excited singlet state, T_1 being the molecule's first electronically excited triplet state, $h\nu_{em}$ the emission caused by phosphorescence, and S_0 the ground state of the molecule.

Due to its forbidden character the transition from the excited triplet state to the ground state is kinetically unfavoured. Therefore phosphorescence is an effect that occurs at much slower timescales than fluorescence. The typical lifetime of an excited electron in an excited singlet state is in the order of nanoseconds, while electrons may remain in the excited triplet state for milliseconds up to hours in the case of specifically designed so-called "glow-in-the-dark" materials.

3.4.2. Raman spectroscopy

Raman spectroscopy is an optical analytical technique based on the so called Raman effect [101]. The Raman effect is named after the Indian scientist Chandrasekhara V. Raman, who discovered the inelastic scattering of light [103].

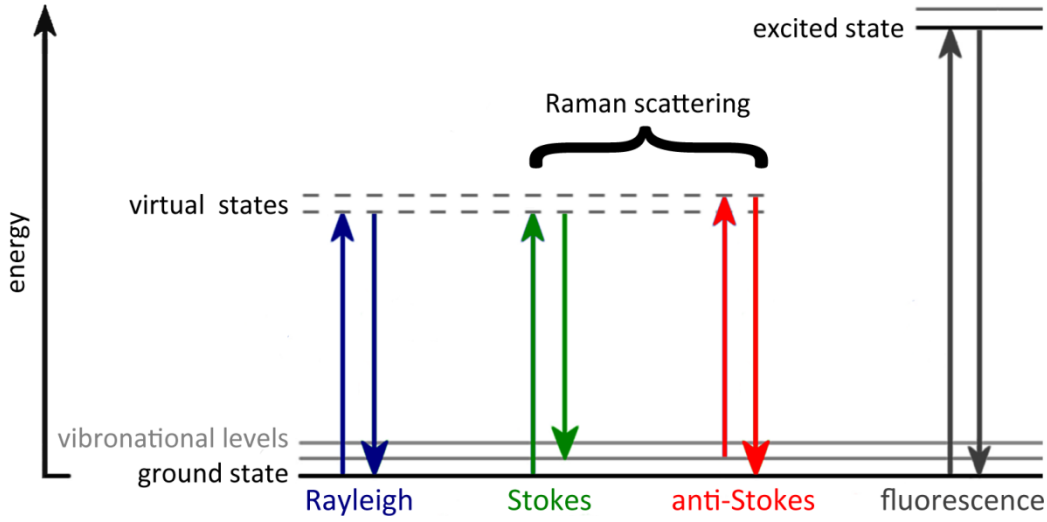

Figure 3-12: Jablonski diagram comparing Rayleigh and Raman scattering. The molecule is excited to a virtual state lower in energy than a real electronic transition; Rayleigh scattering occurs when no energy is gained or lost; a Stokes Raman shift occurs when a photon loses energy, whereas an anti-Stokes Raman shift occurs when the photon gains energy; fluorescence occurs when the photon is actually excited to another electronic state.

The interaction utilized in Raman spectroscopy is the scattering of light from material in different vibrational states, and the related energy exchange. When a

beam of electromagnetic monochromatic radiation impinges on a material, it can either be absorbed (as discussed in the previous section) or scattered. Most photons that aren't absorbed are elastically scattered, that means the scattered photons have the same energy as the incident photons. This is known as Rayleigh scattering, shown in Figure 3-12.

However, a very small proportion of the incident photons scatter inelastically, in a process known as Raman scattering [104]. In this case an energy difference between the incoming and scattered photons can be observed and measured. The Raman effect encompasses two different types of inelastic scattering: Stokes and anti-Stokes, as depicted schematically in Figure 3-12.

Stokes scattering occurs if the material absorbs part of the energy such that the scattered photon has a lower energy than the incident photon. The material is excited from its ground state to a virtual energy level and subsequently relaxes back into a vibrational excited state. The less likely of both, anti-Stokes scattering, happens when the incoming photon interacts with material that is in an excited vibrational state. The material is excited up to the virtual energy state and relaxes back into its ground state. The material loses energy and the scattered photon has more energy than the incident photon. In the case of Stokes scattering the scattered photon has a lower frequency and hence longer wavelength than the incident photon, in anti-Stokes scattering the scattered photon has a higher frequency and thus shorter wavelength than the incoming photon.

The spectrum of the scattered photons is called a Raman spectrum. It typically shows the intensity of scattered photons as a function of their frequency difference to the incident photons. As demonstrated in Figure 3-13, light that interacted with the molecule leaves it at a number of different energies that are shifted with respect to the energy of the incoming photons *E*. Stokes and anti-stokes are located symmetrically around the Rayleigh peak at $\Delta\nu=0$.

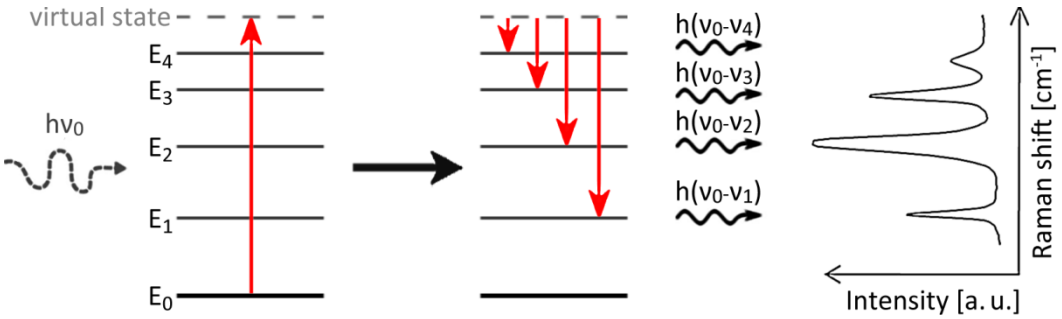

Figure 3-13: Diagram of Raman scattering; a molecule is excited to its virtual state; subsequently photons drop down to specific vibrational levels resulting in frequency shifts that may be displayed as a spectrum of peaks.

These different energy changes ΔE_n correspond to scattered photons being excited to a number of distinct vibrational energy levels. The frequency shifts correlating to these different molecular vibrational modes ($\nu_0 - \nu_n$) are displayed as a spectrum of peaks. The position and intensity of each peak relates to a specific type of molecular vibration such as the stretching, bending, torsion or deformation of a bond, combining to form a spectrum that represents the chemical fingerprint of a material. Precise interpretation of Raman spectra typically requires significant computational effort, as shown for the example of the fullerene C_{60} in Figure 3-14.

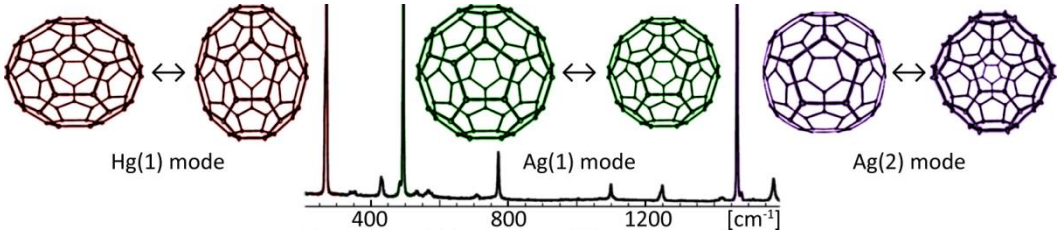

Figure 3-14: Raman spectrum of C_{60} with the vibrational modes of the three Raman shifts with the highest intensity displayed [107].

Menendez and Page calculated from first principles the values for the frequencies of all of the vibrational modes of a C_{60} molecule [105, 106]. Examples in Figure 3-14 show the three modes with the highest intensities of the Raman spectrum.

Chapter 4

Formation of extended covalent networks via Ullmann coupling

4.1. Introduction

The polymerisation of molecules on metallic surfaces enables the formation of two-dimensional tailored nano architectures. There are several approaches to covalent coupling on surfaces, which are discussed in section 2.1. The most common strategy to date is the catalysed and thermally-activated Ullmann coupling reaction on coinage metal substrates. The on-surface formation of covalent links has been achieved by many different research groups, although the size and quality of the resulting nano architectures vary significantly. The lateral dimensions of a two-dimensional polymer may be determined easily, its quality however is more subjective and hard to define.

In 1932 Zachariasen was the first to describe the structural differences between crystals and glass, as shown in Figure 4-1a and b [108].

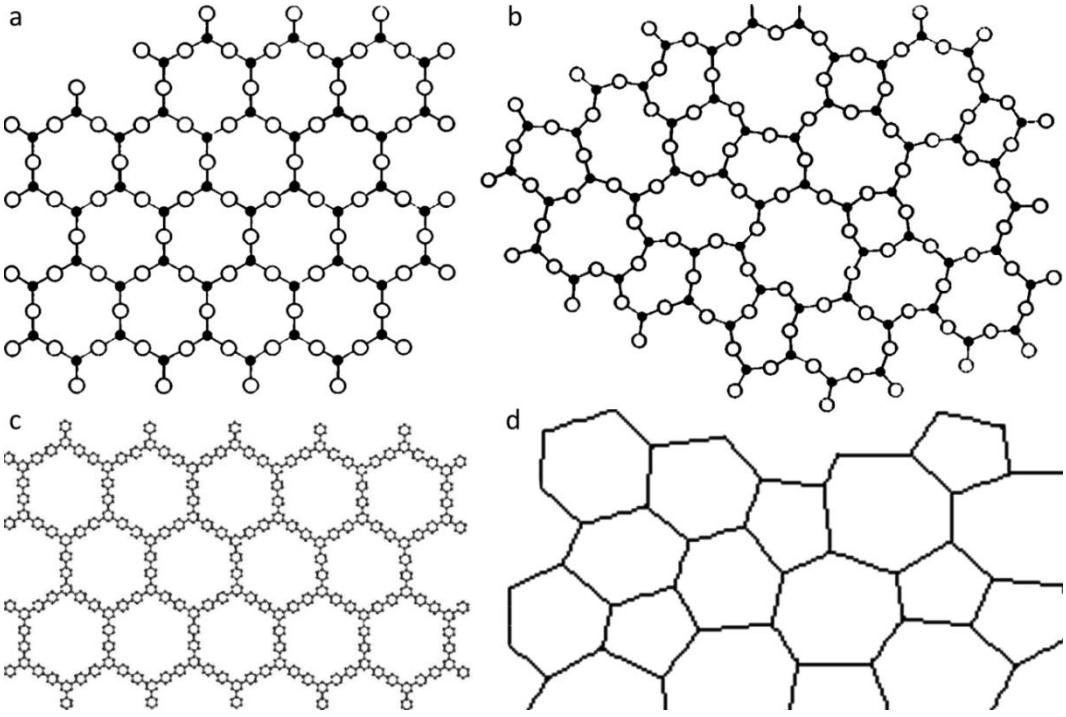

Figure 4-1a: Zachariasen's two-dimensional sketches of crystal with A_2O_3 stoichiometry; b: a glass network of the same compound [108]; c: ideal covalent honeycomb network of tri-(bromo-phenyl)-benzene (TBPB); d: "skeletonized" STM image of covalently linked TBPB.

In his continuous random network (CRN) model the transition from crystalline to amorphous structures is made by introducing variable bond angles. This leads to structural disorder without changing the chemical environment of the atoms. His two-dimensional sketch of the CRN model shows a continuous network consisting of rings of different sizes.

In Figure 4-1c an ideal hexagonal network built from tri-(bromo-phenyl)-benzene (TBPB) molecules is depicted. Figure 4-1d shows a skeletonized STM image of an actual TBPB network formed on Au(111) in UHV. The similarities between Zachariasen's model for oxides in crystalline and vitreous form and the images of two-dimensional polymers are striking. Unlike most of the CRN and paracrystal models, which have to rely on indirect information such as crystal diffraction, a two dimensional network built of molecules can be imaged easily with STM. That makes complicated mathematical interpretations of crystallinity superfluous.

Unlike self-assembled networks, where the weak molecule-molecule interactions allow for surface diffusion and thus enable self-healing processes to eliminate defects, C-C bonds, once formed, do not break under normal conditions. Therefore it is much more difficult for polymers to achieve the high level of long-range order that is typically observed in self-assembled structures.

4.2. Formation of extended polyphenylene networks

The focus of this chapter is the molecule tri-(bromo-phenyl)-benzene (TBPB) and the continuous polyphenylene networks it forms, as depicted in Figure 4-2a and b. Those networks are then briefly compared to polymerised structures formed by the larger tri-(bromo-biphenyl)-benzene (TBBB) molecules, shown in Figure 4-2c and d. Both compounds consist of phenyl rings with bromine terminated end groups. They exhibit a three-fold symmetry that ideally forms a honeycomb structured polyphenylene network of different pore sizes upon

polymerisation. The resulting polymers are purely composed of phenyl rings and sometimes dubbed porous graphene [109].

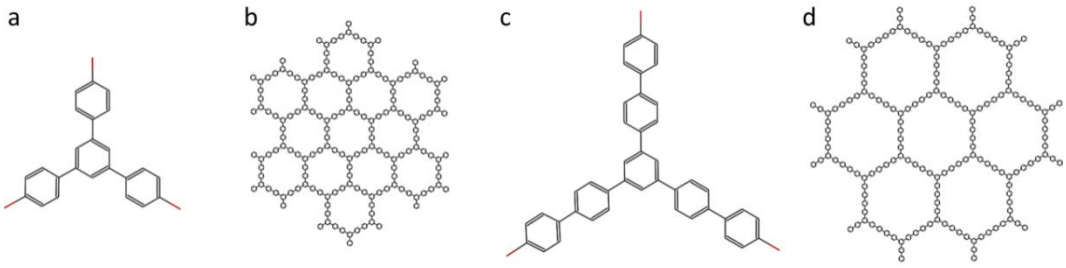

Figure 4-2a: Schematic structure of a tri-(bromo-phenyl)-benzene (TBPB) monomer; b: Honeycomb network built from TBPB molecules; c: Schematic structure of a tri-(bromo-biphenyl)-benzene (TBBB) monomer; d: Honeycomb network built from TBBB molecules.

I will first discuss TBPB and the structures it forms on an oriented Au(111) film grown on mica. The experiments were performed under ultra high vacuum conditions in a system with a base pressure of 10^{-10} mbar. The Au(111) surface was first cleaned by repeated sputter-anneal cycles. Argon sputtering at 10^{-5} mbar, 0.8 keV, 1 µA for 30 minutes removed excess material adsorbed on the surface. Subsequently the sample was annealed at 500°C using a heater formed by a Si(111) wafer placed behind the sample through which current was passed to restore the surface. This process was repeated until a clear herringbone reconstruction was observed with STM, as described in section 3.3.3. Approximately one monolayer TBPB was subsequently deposited from a K-cell at a deposition rate of 1 ML/h.

The resulting surface was investigated with STM. The molecules arrange in an extended regular pattern, as shown in Figure 4-3. Individual molecules with three-fold symmetry can be distinguished in the topographs. They form a well ordered close-packed pattern. The self-assembled structure is weakly bonded via van-der-Waals interactions. The weak nature of the bonds enables mobility and self-healing processes, resulting in a defect free extended pattern with P2

symmetry, as shown in Figure 4-4b. The herringbone reconstruction underneath the molecules is not lifted, as can be observed in Figure 4-3a.

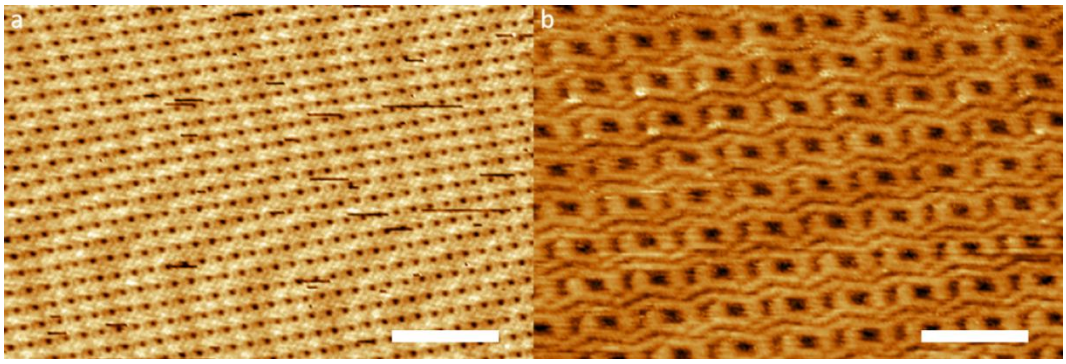

Figure 4-3: STM images (-1.7 V, 0.03 nA) of 1 ML TBPB deposited onto Au(111), the molecules form a close-packed ordered pattern, the herringbone reconstruction of the gold surface is visible through the molecules; scale bar a: 10 nm, b: 3 nm.

To initiate on-surface Ullmann coupling reaction the substrate was annealed for one hour at 250°C and, after cooling down to room temperature, investigated again with STM. The resulting surface is shown in Figure 4-4a.

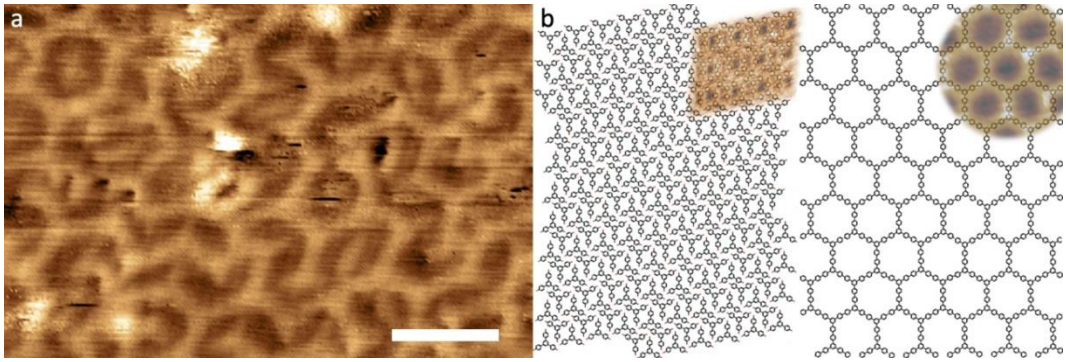

Figure 4-4a: STM image (-1.7 V, 0.03 nA) of 1 ML TBPB deposited onto a gold substrate and subsequent annealing for 1 h at 200°C; scale bar 3 nm; b: Schematics of the close-packed self-assembled structure as observed in Figure 4-3 versus the ideal covalent honeycomb network as observed in Figure 4-5.

After 1 h annealing at 200°C the TBPB molecules form covalent bonds with neighbouring molecules, resulting in a disordered network. However, the high coverage of molecules on the surface prior to annealing seems to prevent the expected open-porous honeycomb structure from forming. The schematics in Figure 4-4b show that the density of molecules in the close-packed self-assembled structure is about twice as high as the density of molecules in the ideal open-porous covalent honeycomb structure.

To prevent the formation of a close packed monolayer altogether, TBPB was deposited for 30 minutes onto a Au(111) surface held at about 180°C, and the sample was subsequently annealed at 200°C for 30 minutes. This cycle was repeated once, resulting in 1 h deposition and 1 h annealing. STM images of the resulting surface were taken after the sample had cooled down to room temperature. The STM topographs exhibit patches of covalently-linked glassy structures. The experiment was repeated for different deposition temperatures until a monolayer coverage was achieved, as shown in Figure 4-5a and b.

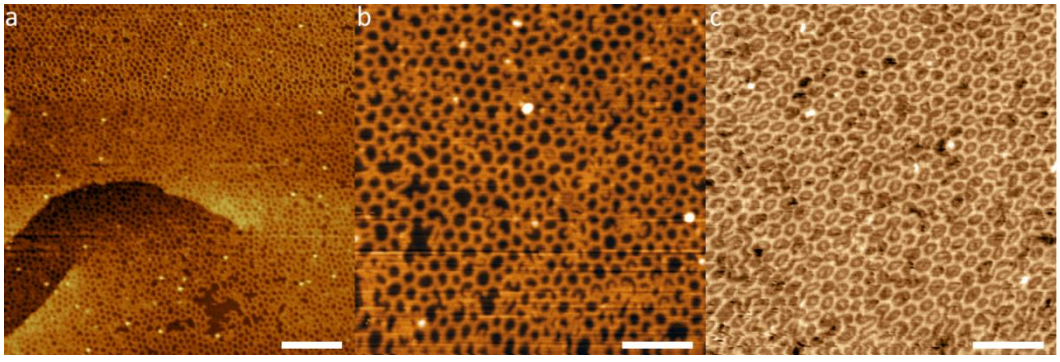

Figure 4-5: STM images (-1.7 V, 0.03 nA) of 1 ML TBPB deposited onto Au(111) held at 180°C, the molecules form a continuous network over large areas (a, b); longer deposition results in trapped monomers inside the cavities (c); scale bar a: 20 nm, b: 10 nm, c: 10 nm.

The resulting structure is a continuous network predominantly consisting of polygons with 4, 5, 6, 7, or 8 corners. Islands of continuous network extend at least over several µm. Scanning several adjacent areas with image sizes of

500 nm^2 on different locations across the whole gold sample does not reveal any extended clean gold surface. Deposition rates that exceed the coverage of one monolayer of the open porous network result in filled cavities. Single molecules become trapped inside the cavities, as shown in Figure 4-5c.

To analyse the distribution of polygons of the networks, the STM images were converted into colour-coded skeletonized vector graphics. Figure 4-7 shows the sequence of image processing steps which were used to convert experimentally attained STM images into a skeletonized vector graphic with colourised polygons. The original STM image was flattened (the gradient is subtracted for each horizontal scan line) using the open source software package WSxM [110] to enhance and standardise the overall contrast as shown in Figure 4-7a.

The image was subsequently converted into a black and white image using the Photoshop CS5 stamp filter [Adobe Photoshop CS5 Extended Version 12.1 x32]. This is an extreme contrast function which converts all bright regions above a certain threshold, in this case the covalent network and some defects, to zero intensity black areas, and below threshold dark regions, i.e. cavities, to full intensity white areas. The result is in shown in Figure 4-7b.

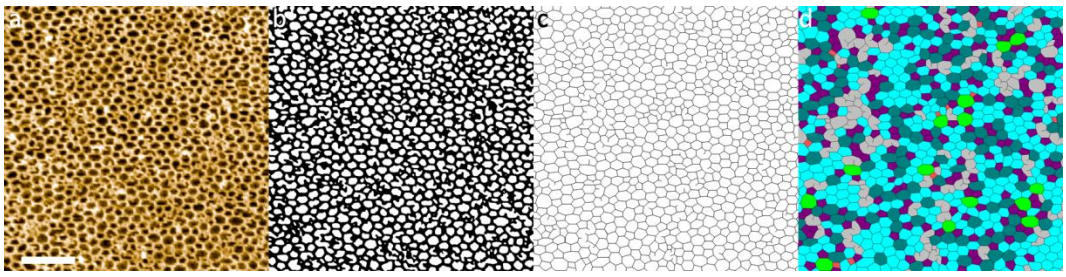

Figure 4-6: Image processing steps from an STM image to a colour-coded map of polygons (red – tetragon, purple – pentagon, cyan – hexagon, teal – heptagon, green – octagon); scale bar 10 nm.

The image was subsequently imported into FIJI [111] as an 8-bit binary image. This program allows the conversion of the dark lines with finite thickness

in Figure 4-7b into lines of single pixel width using the skeletonize tool. The network is now a simplified and compact representation of the original network that preserves its key features such as junctions and connectivity. A path following the skeleton connecting the junctions via straight lines was created in Illustrator CS5 [Adobe Illustrator CS5 Extended Version 15.1.0] using the live trace function to recreate a vectorised graphic of the original as shown in Figure 4-7c. The resulting network was checked by superimposing the network over the original image. Missing connections were appended and defective regions omitted.

Finally the polygonal cavities were coloured manually according to the scheme: red – tetragon, purple – pentagon, cyan – hexagon, teal – heptagon, green – octagon. Grey areas indicate open, imperfect, or non-determinable cavities.

Two different parameters were extracted from the colour-coded polygonal networks. The distribution of intact polygons was counted and the faction of grey area was calculated. Evaluation of five images of extended networks with monolayer coverage resulted in the following statistics depicted in Figure 4-7.

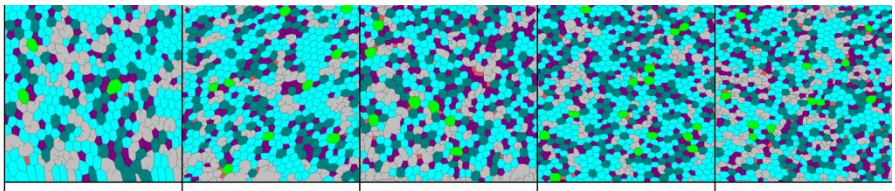

tetragons	2 (1%)	7 (1%)	17 (3%)	11 (1%)	26 (4%)
pentagons	70 (21%)	115 (23%)	172 (34%)	198 (28%)	195 (28%)
hexagons	198 (60%)	288 (57%)	228 (45%)	358 (50%)	337 (48%)
heptagons	54 (17%)	89 (17%)	87 (17%)	135 (19%)	124 (18%)
octagons	3 (1%)	9 (2%)	7 (1%)	15 (2%)	11 (2%)
SUM	327 (100%)	508 (100%)	511 (100%)	638 (100%)	693 (100%)
grey area	28%	25%	28%	19%	20%

Figure 4-7: Statistics of the distribution of polygons in five analysed STM images of TBPB networks.

In the evaluated networks hexagons make up 45 to 60% of the intact polygons, pentagons and heptagons combined the other 40 to 60%. Tetragons and octagons are a comparably rare occurrence with 1 to 4% each. Less than a third of the surface is comprised open, concave, imperfect, or non-determinable cavities and intermeshed grain boundaries.

DFT calculations conducted by Tamblyn [113] of the relative energy per TBPB molecule bound in the different observed polygons are displayed in Figure 4-8a [112]. The DFT calculations of the relative energy per TBPB molecule when bound in regular isolated polygons corroborate the numbers observed in the STM images. Hexagons are, unsurprisingly, energetically favoured, followed by heptagons and pentagons.

Based on this simple energy calculation, in equilibrium a polycrystalline network of ideal honeycomb islands joined by grain boundaries would be expected rather than the vitreous network that is observed in experiment. Thus the observed structures are probably non-equilibrium, glassy ones.

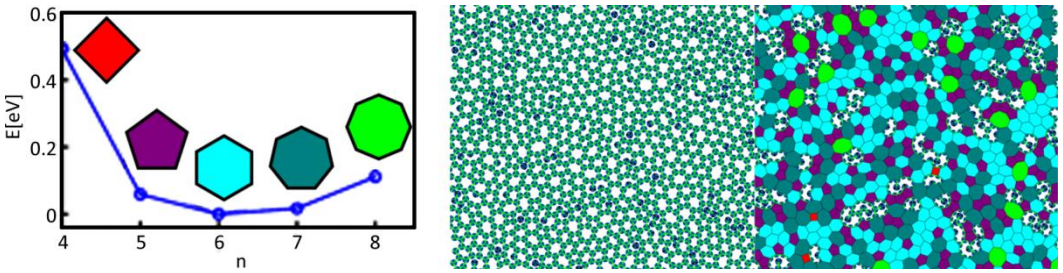

Figure 4-8a: DFT calculations showing the relative energy per TBPB molecule when bound in regular isolated polygons; b: Particle and polygon representation of calculated disk network assembled in the 'glass-forming' regime [113].

Following this observation Whitelam developed a statistical mechanical "patchy particle" model to reproduce disordered networks and simulated the TBPB networks [113]. His model only accounts for the geometry, bond flexibility, and bond strength of the molecular building blocks, indicating that those are the two most important factors for the structure of the resulting networks. In his

model a molecule is represented by a flat disk with three stripes placed regularly around the centre. The angular width of those stripes determines the bond flexibility.

The calculations show that when the binding energy between disks is high, the polygon network is kinetically trapped, resulting in the vitreous structure. High bond angles (10 - 20°) allow for the formation of a range of polygons via a diffusive dynamics on the surface. The polygons are locked in, because the bonds are too strong to be broken. DFT calculations set the bond strength of TBPB at 5 eV, effectively unbreakable at experimental conditions. The strong visual similarity between the simulated and the experimental images suggests that the model successfully reproduces the physics that determines the structure of the networks.

However the model does not fully explore the impact of other parameters that may influence the network formation. Experiments show that the surface temperature during deposition and the subsequent annealing influences the structure of the resulting network.

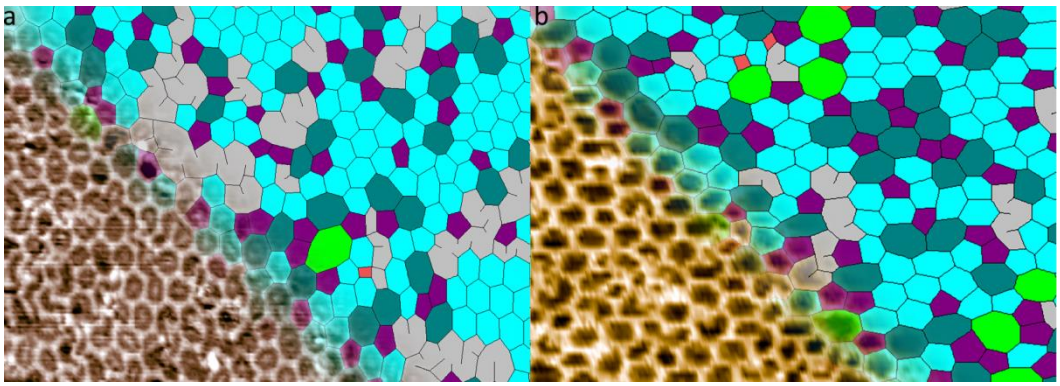

Figure 4-9: STM images of TBPB networks fading into polygon representation; a: Polycrystalline disordered structure containing patches of glassy network separated by intermeshed grain boundaries; b: Vitreous network with less grey area and a higher percentage of non-hexagonal polygons.

Depending on those values, the surface resembles more a polycrystalline surface with fairly well ordered patches joined by interwoven grain boundaries or a vitreous surface with a larger spread of non-hexagonal polygons. Two examples are shown in Figure 4-9.

The network in Figure 4-9a was formed on a surface held at 250°C with subsequent annealing at 300°C. This approach results in a more polycrystalline structure with a higher faction of hexagons (>55%) compared to the other polygons, but also in many grain boundaries (grey area, >25%).

A more vitreous network on the other hand was formed when the molecules are deposited onto a cooler sample held at 200°C with annealing at 250°C. An example is shown in Figure 4-9b. The higher surface temperature and resulting increased mobility of the molecules seems to favour the growth of islands which then join at high coverages, while a lower surface temperature favours the formation of covalent bonds over diffusion and arrangement into hexagonal structures. The faction of hexagons (<50%) is lower in favour of pentagons and heptagons, and grain boundaries are less prevalent (grey area, <20%).

Annealing the samples to temperatures up to 500°C after the networks have formed does not destroy the networks, nor does it change the structure notably. The covalent bonds don't break at this temperature, so self-healing and optimisation of the network is not possible.

Complementary to the polyphenylene TBPB networks, the formation of extended two-dimensional polymers built of the larger tetra-(bibromo-biphenyl)-benzene (TBBB) is investigated next. As shown in Figure 4-2c, the symmetry of the molecule remains the same, only the substituents on the benzene core are elongated by one phenyl group. This leads to an enlarged pore-size in the ideal honeycomb network as shown in Figure 4-2d.

Following the same recipe that results in extended covalent networks of the TBPB monomers, TBBB molecules were deposited in UHV from a K-cell onto a

clean Au(111) surface kept at 180°C at deposition rates of 1ML/h and subsequently annealed for 30 min at 200°C. This deposition/anneal cycle was repeated once. After the sample was cooled down to room temperature it was investigated with UHV-STM, as shown in Figure 4-10.

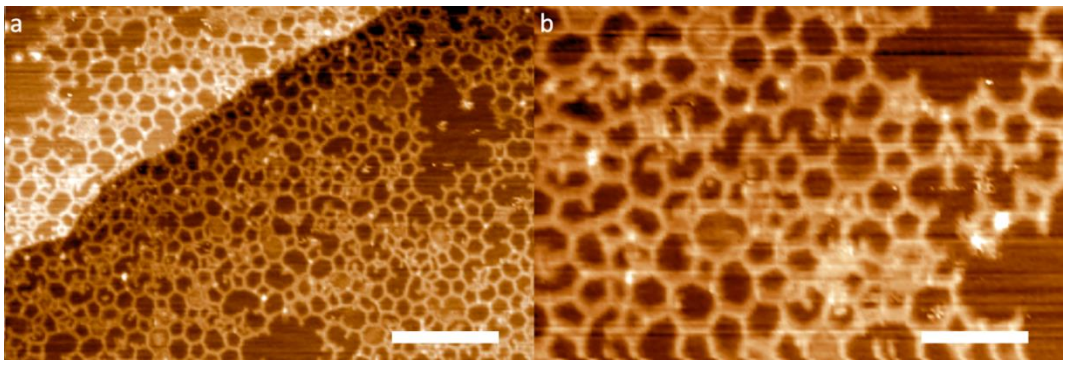

Figure 4-10: STM images (-1.7 V, 0.03 nA) of 1 ML TBBB deposited onto Au(111) held at 170°, the molecules form the molecules form a continuous random network over large areas; scale bar a: 20 nm, b: 10 nm.

Like TBPB, the larger TBBB forms open-porous disordered networks extended over large areas of the surface. Compared to the TBPB networks the coexistence of filled polygonal cavities and empty areas is more pronounced. A reason for this is that heavier molecules have a lower surface mobility, thus covalent coupling dominates over the energetically ideal arrangement of the molecules in a hexagonal network. Secondly the increased flexibility of the longer links results in a much higher percentage of tetramers, heptamers, and even octamers formed in the network

4.3. On-surface polymerisation of porphyrin monomers

Unlike the benzene-based molecules discussed in the previous section, which exhibit three-fold symmetry, porphyrin exhibits a four-fold symmetry. Therefore ideal covalent networks should form quadratic cavities. The molecules discussed in this chapter are tetra-(bromo-phenyl)-porphyrin (TBPP), tetra-(bromo-

phenyl)-porphyrinato-zinc (TBPP-Zn), and tetra-(bromo-anthracene)-porphyrin (TBAP), as depicted in Figure 4-11.

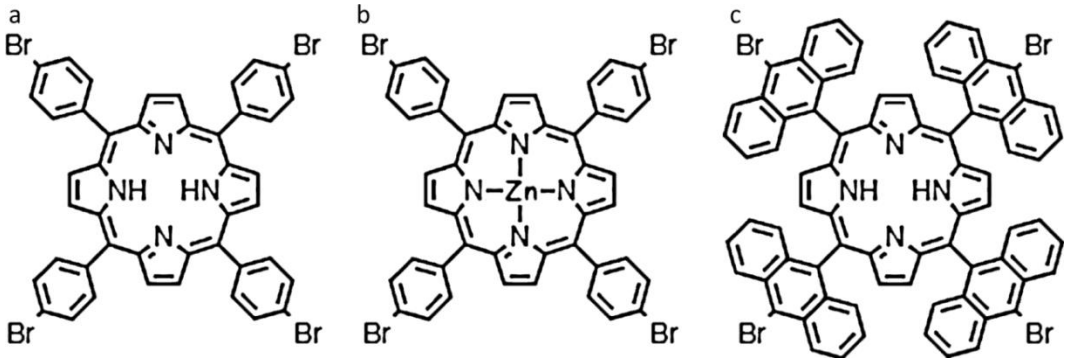

Figure 4-11a: Structure of a tetra-(bromo-phenyl)-porphyrin (TBPP) monomer; b: Structure of a tetra-(bromo-phenyl)-porphyrinato-zinc (TBPP-Zn) monomer; c: Structure of a tetra-(bromo-anthracene)-porphyrin (TBAP) monomer.

The porphyrin monomers were synthesized by Champness and co-workers at the University of Nottingham's Chemistry department.

The first molecule to be discussed is TBPP. TBPP was deposited from a K-cell onto Au(111) on mica under ultra high vacuum conditions. The Au(111) surface was first cleaned by repeated sputter-anneal cycles. Argon sputtering ensued at 10^{-5} mbar, 0.8 keV, 1 µA for 30 minutes. Subsequently the sample was annealed using a piece of Si(111) wafer placed behind the sample through which current was passed. The two steps were repeated until a clear herringbone reconstruction was observed with STM.

The TBPP was deposited from a K-cell at a deposition rate of 1 ML/h. The resulting surface was investigated with STM, as shown in Figure 4-12a. Unlike the other molecules investigated in this thesis, which can be imaged at negative or positive tip bias, the TBPP monomers were only visible in positive tip bias. Scanning at negative bias shows the herringbone reconstruction of the gold surface.

The porphyrin molecules form a close packed pattern with the two-dimensional space group p4. Some molecules appear with a darker contrast than the others. This is likely due to different conformations of the molecules [114].

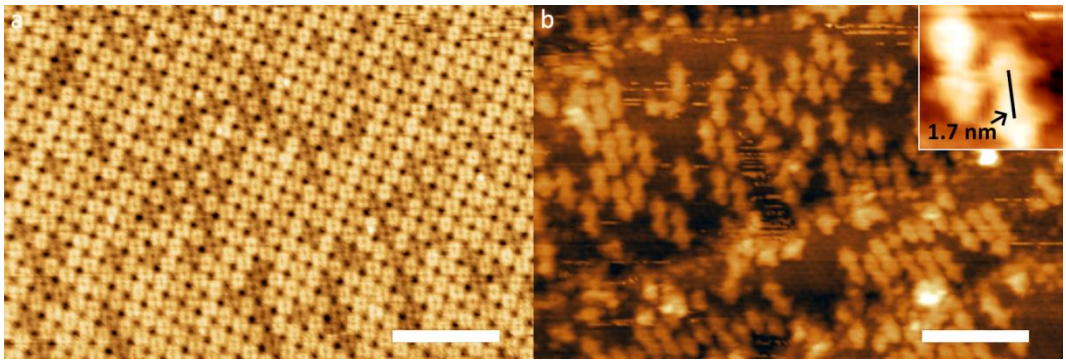

Figure 4-12a: STM image (+1.7 V, 0.03 nA) of 1 ML TBPP deposited onto Au(111); the molecules form a close packed ordered pattern; b: STM image (-1.7 V, 0.03 nA) of 1 ML TBPP deposited onto Au(111) and subsequent annealing at 300°C, dimers in parallel alignment are formed; inset: zoom of covalently linked dimers with centre-to-centre distance indicated; scale bar 10 nm.

Upon annealing of the substrate, dimers are predominantly formed, as shown in the STM image in Figure 4-12b. However, further annealing at elevated temperatures lead to desorption or disintegration of the porphyrin molecules rather than formation of extended covalent networks. Previous reports on covalently linked TBPP focussed mainly on the formation of covalent bonds at low surface coverage rather than extended networks. Grill and co-workers successfully formed small well-ordered islands of covalently linked TBPP as described in section 2.1.1.

However, they investigated mainly the impact the deposition temperature has on network formation and kept the sample at room temperature during deposition. Their results show patches of square covalently linked networks extending over several nanometres rather than complete monolayer coverage. Thus to form extended, highly interlinked polymers the porphyrin molecules

were as discussed in the previous section in relation to the benzene molecules, deposited onto a heated substrate and annealed subsequently. Best results were found to form at a very low deposition rates. TBPP was deposited overnight for 10 to 14 h onto a substrate held at 180°C at a deposition rate of 1ML/12h and subsequently annealed for two hours at 200°C. This approach leads to extended, covalently linked, random networks as shown in the STM image in Figure 4-13.

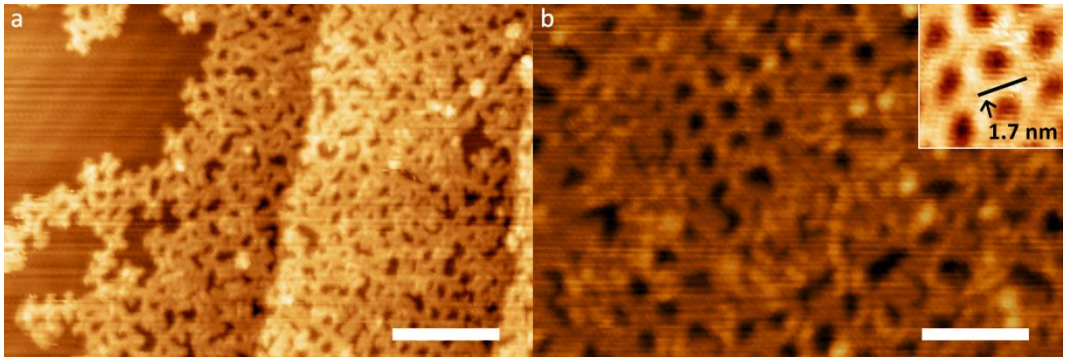

Figure 4-13: STM images (-1.5 V, 0.05 nA) of TBPP deposited for 10 h (a) and 14 h (b) onto Au(111) held at 180°C and subsequent annealing for 2 h at 200°C, the molecules form a continuous random network over large areas; inset: zoom of covalently linked molecules with centre-to-centre distance indicated; scale bar a: 10 nm, b: 5 nm.

Local patches of the expected square lattice are embedded in a highly interconnected disordered polymeric matrix. The centre-to-centre distance of two adjacent porphyrin molecules is measured to be 1.7 ± 0.1 nm for the dimers in Figure 4-12b and the locally square ordered polymer regions in Figure 4-13. This is in very good agreement with the experimentally determined (1.72 ± 0.03 nm) and calculated (1.71 nm) distances Grill reported [16].

Tip structure and scanning parameters (P- and I-gain) can influence the apparent structure of the polymers significantly, as shown in image 4-14. The STM images were all taken on the same sample on the same day with varying scanning parameters and tip pulsing in between images. Figure 4-14a

emphasises the structure of the network more than the individual porphyrin monomers. In Figure 4-14b the individual molecules become more prominent, and the bonds appear in lower contrast, the local square patterns and centre-to-centre distance however remain unchanged.

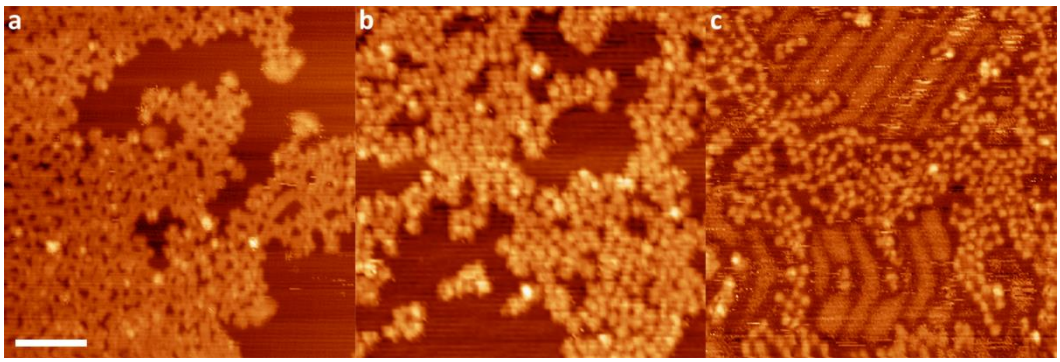

Figure 4-14: STM images of TBPP deposited onto Au(111) held at 180°C and subsequent annealing at 200°C; a: -1.5 V, 0.05 nA; b: -1.5 V, 0.05 nA; c: -1.7 V, 0,03 nA; scale bar 10 nm.

The covalent links between the individual porphyrin molecules in Figure 4-14c are not visible, the square TBPP subunits and a very pronounced herringbone reconstruction are the striking features of this image. The only indication for a covalent network is the centre-to-centre distance between adjacent molecules, and the dissimilar pattern to the self-assembled structures, as shown in Figure 4-12a.

Next tetra-(bromo-phenyl)-porphyrinato-zinc (TBPP-Zn) is investigated. As depicted in Figure 4-11b, the porphyrin macrocycle of TBPP-Zn has a zinc atom in its centre, the substituents at the *meso* positions are analogous to TBPP.

The molecules were deposited using the same deposition and substrate temperature parameters as the free-base version of the phenyl porphyrin molecule, TBPP. Slow sublimation at a deposition rate of 1 ML/12h for 10 to 14 h onto a clean gold substrate held at 180 °C was followed by annealing at 200°C for 2 h. The STM images in Figure 4-15 show that the resulting surface of

TBPP-Zn exhibits a similar structure and connectivity as the previously investigated TBPP networks.

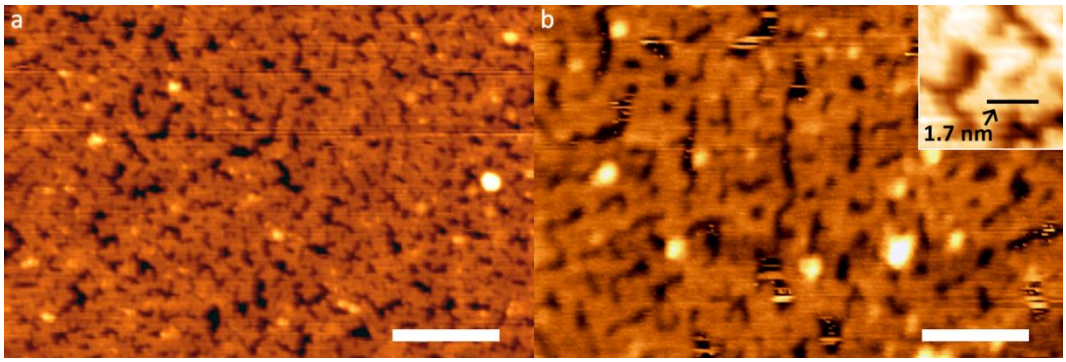

Figure 4-15: STM images (-1.5 V, 0.05 nA) of TBPP-Zn deposited onto Au(111) held at 180°C and subsequent annealing at 200°C, the molecules form a continuous random network over large areas; inset: zoom of covalently linked molecules with centre-to-centre distance indicated; scale bar a: 10 nm, b: 5 nm.

The STM images show a cross-linked extended structure with submolecular resolution on the porphyrin monomers. The centre-to-centre distance between two adjacent linked molecules is the same as for the free base molecules, 1.7 ± 0.1 nm.

The next porphyrin molecule investigated is tetra-(bromo-anthracene)-porphyrin, as depicted in Figure 4-10c. The molecules could not be deposited in UHV from a K-cell. Attempts to determine the deposition rate with a quartz microbalance did not show any sign of sublimed material on the thickness monitor.

Therefore electrospray deposition (ESD, as described in section 3.1) is chosen for deposition. The solution used in the experiments has a porphyrin monomer concentration of 100 µg/mL in a methanol/toluene mixture (1:3 by volume). The molecules were deposited at a flow rate of ~10 µL / min through a stainless steel emitter held at ~1.8 kV under atmospheric conditions onto gold for 10 minutes. During the deposition the pressure in the deposition chamber rose

from a base pressure of 10^{-9} mbar to the low 10^{-5} mbar range. The Au(111) on mica sample was cleaned prior to deposition by repeated cycles of Ar ion sputtering (1×10^{-5} mbar, 0.8 keV, ~1 µA) and subsequent annealing (~500°C), until a clear herringbone reconstruction was observed.

After deposition the sample was investigated with STM. No molecular structures could be resolved when scanning on the estimated area where the molecules hit the surface.

Subsequently the sample was annealed for 2 h at 200°C to desorb excess material, increase surface mobility of the porphyrin monomers, and facilitate Ullmann-type covalent coupling. STM images of the surface after annealing reveal patches of linked molecules, as shown in Figure 4-16.

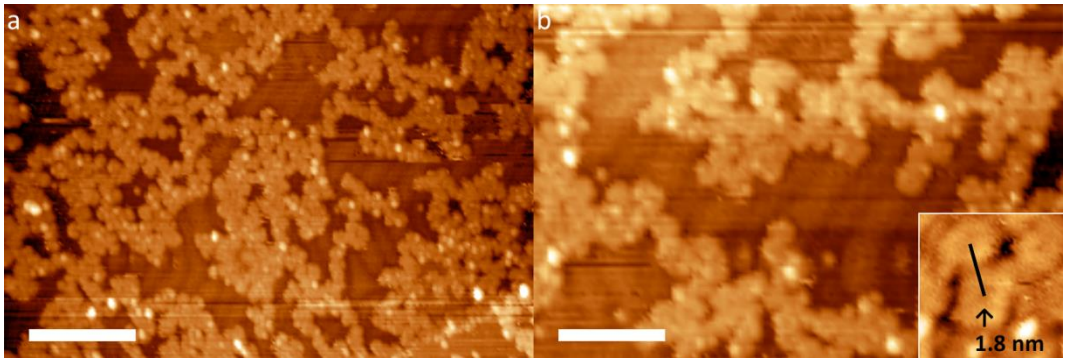

Figure 4-16: STM images (-1.7 V, 0.03 nA) of TBAP deposited onto Au(111) via electrospray deposition and subsequent annealing at 200°C, the molecules form an open, but continuous interconnected network; inset: zoom of covalently linked molecules with centre-to-centre distance indicated; scale bar a: 10 nm, b: 5 nm.

The molecules form dense interconnected islands with diameters of up to 20 nm, which are connected to other islands via polymeric chains. The polymeric chains preferably align along the herringbone reconstruction as can be seen in Figure 4-16b. The measured centre-to-centre distance is with 1.8 ± 0.2 nm slightly higher than the link between the similar TBPP and TBPP-Zn molecules,

although within error boundaries. The poor resolution of the STM images makes a precise estimation of the distance difficult.

4.4. Conclusions

Halogenated organic molecules may be used to form open-porous highly interconnected two-dimensional polymers on a gold substrate. The networks extend over large areas of the sample, near monolayer coverage is achieved. Due to the high reactivity of the radicals after dissociation of the halogen and the high bond strength of covalent links, the long range order of those networks is poor compared to self-assembled, weakly bonded structures. The vitreous structure and high interconnectivity of the molecules however results in a very high mechanical, thermal, and chemical stability. This feature is utilised in the following chapter, where porphyrin networks of monolayer thickness are transferred from the gold onto a new substrate.

Chapter 5

The transfer of metallic, molecular and polymer thin films using fullerenes as adhesive layers

5.1. Introduction

1- and 2-dimensional covalent organic networks are widely studied for possible applications as electronic materials and graphene analogues. Organic networks are commonly produced by on-surface coupling reactions leading to extended polymeric networks as described in the previous chapter. Via modification of the building blocks the frameworks can be tailored to meet target requirements. There have been great advances in the understanding of the growth and formation of such arrays, but their application in a functional form has so far been limited by their formation on substrates which are not compatible with potential applications. The formation of 2d covalent organic networks via radical covalent coupling typically requires specific substrates to catalyse the on-surface reaction. Metallic surfaces are commonly chosen particularly for schemes which require catalysts to enable dehalogenation, dehydrogenation, or other forms of radical formation of the molecules as a route to the formation of covalent bonds, as described in section 2.1. However, many of the potentially interesting optical and/or electrical properties of the resulting networks cannot be investigated or utilised while the structures remain adsorbed on a metal substrate.

In a complementary strand of research, the mechanical removal of thin films, molecular layers, and nanostructured semiconductors from substrates on which they are grown has been developed over several decades for applications in photonics, sensing and flexible electronics as described in section 2.3. This chapter will explore a novel way of template stripping (the removal of thin films/nanostructures from a substrate) and transfer printing (the transfer of thin films/nanostructures from one substrate to another) utilising the fullerene C_{60} as an adhesive. The development of a systematic process for the transfer of functional monolayers analogous to template stripping is thus of great interest, but many of the layers of potential interest are likely to be chemically and mechanically fragile and are therefore unlikely to be compatible with the

application of conventional epoxies and, in addition, have unknown solubilities in solvents which might be used to remove the epoxy layers in subsequent process steps. Furthermore, the application of epoxy is not easily compatible with the controlled environments, such as ultra-high vacuum, under which many on-surface polymerisation studies are performed.

This chapter will describe how a process was developed to transfer molecular thin films and polymerised monolayers of tetra-(bromo-phenyl)-porphyrin (TBPP) and tetra-(bromo-phenyl)-porphyrinato-zinc (TBPP-Zn) onto SiO_2. Porphyrin derivates were chosen because of a known route to their polymerisation as was shown in section 4.3 combined with their distinctive optical properties. Thin layers of porphyrin can be detected with fluorescence spectroscopy as demonstrated in Figure 5-1 on the example of 3 nm thin film of TBPP and TBPP-Zn deposited onto SiO_2/Si.

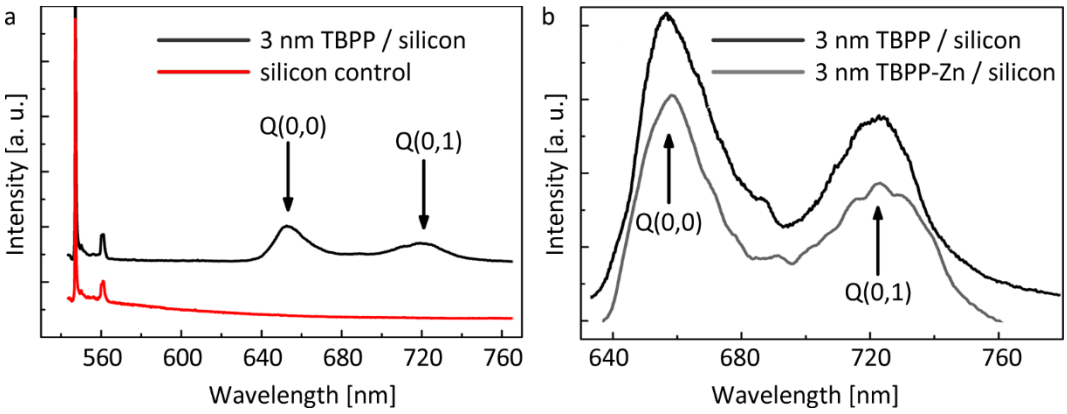

Figure 5-1: Fluorescence spectra (excitation wavelength = 532nm) of thin layers of TBPP and TBPP-Zn on SiO_2/Si substrates. The characteristic double-peak at 656 ± 1 nm (Q(0,0)) and 722 ± 1 nm (Q(0,1)) for TBPP and 655 ± 1 nm (Q(0,0)) and 720 ± 1 nm (Q(0,1)) for TBPP-Zn originates in intense absorptions in the visible region [47].

Figure 5-1 shows spectra of thin layers of porphyrin on a silicon substrate. In the wavelength region between 640 and 740 nm porphyrins, both free-base and

with a metallic centre, exhibit a characteristic double peak with one peak at ~655 nm (Q(0,0)) and one at ~720 nm (Q(0,1)). Porphyrin monomers are prone to beam damage and disintegrate or desorb at high laser intensity or long integration times. Fortunately the SiO_2 spectrum in this region is featureless and introduces a negligible background. Thus it is possible to detect very thin layers of porphyrin with very weak laser powers. The characteristic double peak of porphyrin corresponds to fluorescence of the Q bands Q(0,0) and Q(0,1) connected with transition from the first excited singlet state to the ground state ($S_0 \leftarrow S_1$), as described in section 2.2. The positions of the peaks is slightly blue-shifted for the zincated porphyrin TBPP-Zn compared to the free-base porphyrin TBPP. This is in agreement with previous studies [55].

5.2. Fullerenes as an adhesive

Before the entire transfer process was implemented, the adhesive qualities of fullerenes were explored. A sublimed layer of organic molecules provides unexpected adhesive properties which may be used to remove thin metallic films from a mica substrate by mechanical peeling. The focus in this chapter is in particular on the adhesive properties of C_{60}. Films with a thickness greater than 10 nm can be used for this application. The use of a sublimed C_{60} adhesion layer also ensures high chemical purity, is compatible with formation under UHV conditions, and is known, even for thicknesses down to 3 nm, to provide effective protection for buried 'UHV-clean' surfaces on exposure to atmosphere [115]. In addition, small organic molecules such as C_{60} are readily soluble in a range of solvents offering a flexible approach to the selective removal of the adhesion layers while leaving the underlying substrate intact.

The experiments start with a gold thin film deposited on mica. Pieces with typical dimensions of 1 x 1 cm^2 were loaded into a UHV system (base pressure 10^{-10} mbar) and prepared by repeated cycles of sputtering and annealing until a clear herringbone reconstruction pattern was observed with STM as described in

detail in Chapter 3. Fullerene films with thickness ranging from 5 nm to 100 nm were subsequently deposited via sublimation from a Knudsen cell at a deposition rate of 1 nm/min.

The samples were then removed from UHV and support layers of polydimethylsiloxane (PDMS) were deposited onto the sample. The PDMS was prepared from 9 parts of 184 silicon elastomer base and 1 part of 184 silicon elastomer curing agent (commercially supplied by Dow Corning), stirred thoroughly and left to de-gas for 20 minutes until all gas bubbles had been expelled. The viscous liquid was then applied to the sample with a thickness of ~1 mm, and cured in the oven at 150°C for 15 min. After the sample had cooled down to room temperature the elastic PDMS layer was cut to match the gold sample size and carefully lifted with a pair of tweezers. This mechanical peeling of the elastomer also removed more than 90% of the gold from the mica, as shown in the photographs in Figure 5-2a.

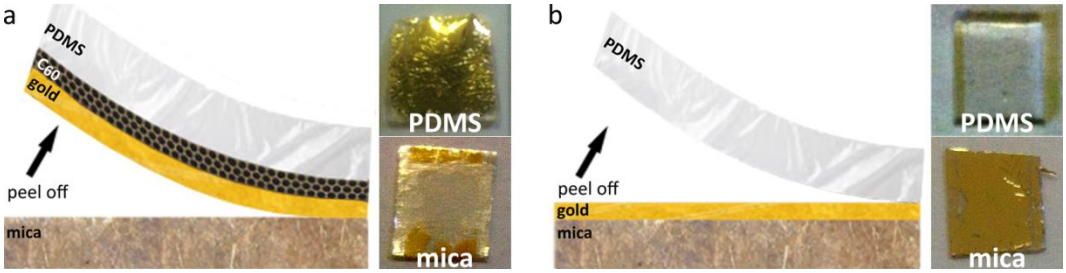

Figure 5-2: Schematics and photographs of mica and PDMS surfaces after peeling of PDMS off a gold on mica sample with (a) and without (b) a layer of C_{60}; the adhesive properties of C_{60} enable clean removal of the gold off the mica.

The remaining areas of gold which were not removed, were covered by clamps on the sample holder in the UHV chamber, and thus not exposed to C_{60}.

For control samples, where the PDMS was directly deposited onto a sputter-annealed clean Au(111) sample in the same way as described above, and the PDMS was peeled off afterwards, it left the gold layer intact on the mica as

depicted schematically and shown in the photographs in Figure 5-2b. This indicates that the adhesive properties arise from the fullerene layer.

For C_{60} layers with thickness of less than 10 nm the gold remained partially on the mica substrate. In this case application of the PDMS might have displaced the C_{60}. Those areas of direct contact between the gold and PDMS without adhesive would remain intact upon peeling. A fullerene thickness of 15 nm was therefore used as a standard in subsequent experiments. To explore if the peeling process is unique to gold as a substrate and C_{60} as adhesive, the same experiments were conducted substituting Ag(111) for Au(111), and perylene-tetracaboxylic-diimide (PTCDI) for C_{60} respectively. Peeling silver off mica using a 15 nm thick layer of C_{60} as an adhesive led to similar results – the peeling worked very reliably. An analogous, but less reliable and reproducible effect was obtained when substituting PTCDI for C_{60} when peeling gold off a mica substrate.

Optical microscope images of the surface before and after peeling reveal that the peeling process leaves a mudcrack-like pattern on the gold surface, as shown in the microscope image in Figure 5-3b.

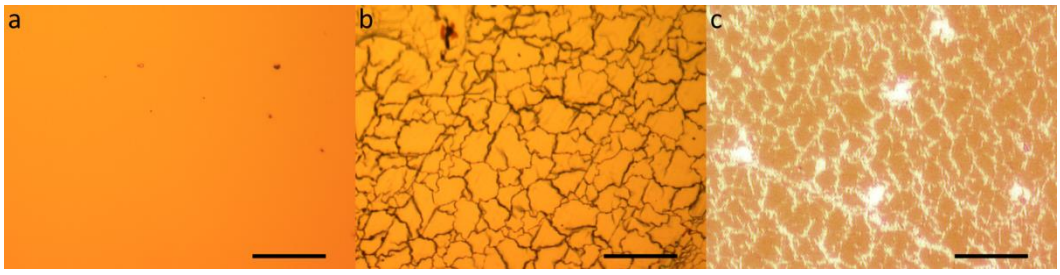

Figure 5-3: Optical microscope images of a: Gold on mica sample with 15 nm C_{60} sublimed from a K-cell; b: PDMS/C_{60}/gold after peeling from the mica substrate; c: PDMS/C_{60} after etching of gold; scale bar: 500 µm.

To investigate if the transfer process has any impact on the fullerene layer, the gold was etched after the sample was removed from the mica. This will be of relevance for transfer experiments in the following chapter. For the removal of

the gold layer commercial gold etchant, an aqueous potassium iodide solution was used on the exposed gold layer for 3 to 5 min. A few drops of KI were applied onto the sample until the whole surface was covered, without breaking the surface tension, so that the drop stayed on the sample only, and left to etch until the gold layer was completely gone. Subsequently the samples were rinsed with de-ionised water to remove excess KI, and blow-dried with nitrogen. The mudcrack pattern is preserved in the fullerene layer, as shown in the optical microscopy image in Figure 5-3c.

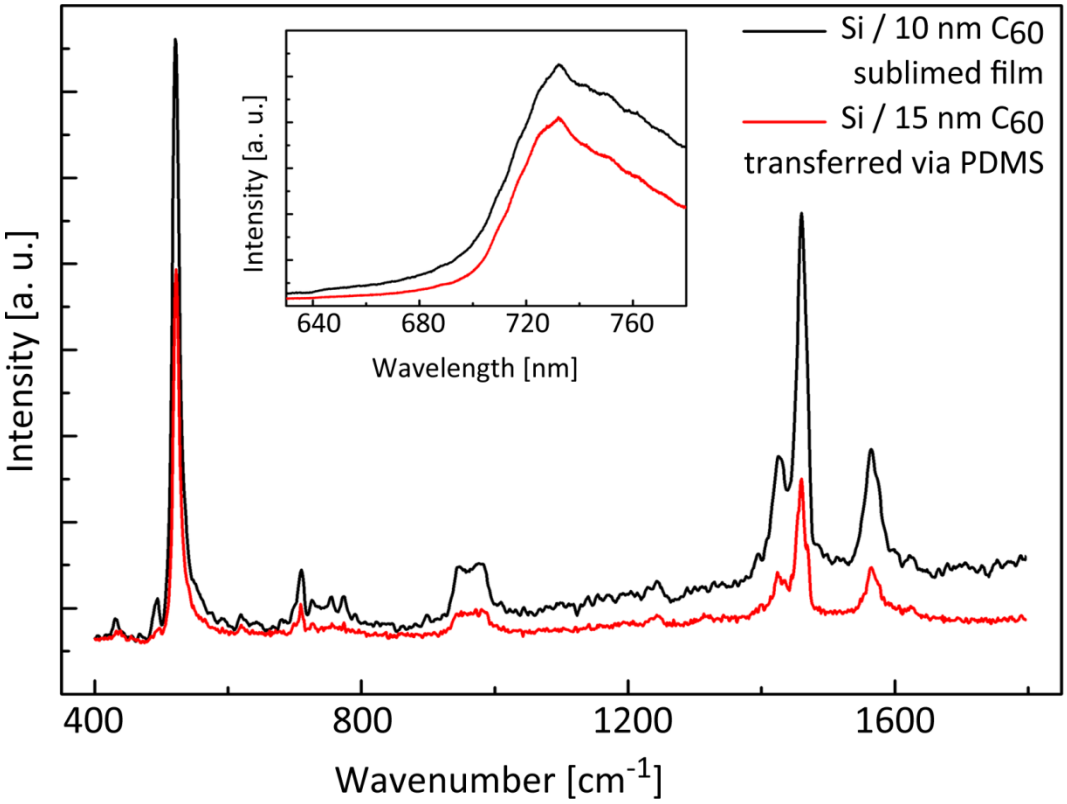

Figure 5-4: Raman spectra of C_{60} on SiO_2/Si; the features at 520 and 900-1000 cm^{-1} correspond to the Si substrate, the peak at 720 cm^{-1} and the region between 1400 and 1600 cm^{-1} with the relatively sharp peak at 1470 cm^{-1} are characteristic for C_{60} [107]; insert: fluorescence emission spectra (excitation wavelength = 532 nm) of the same samples with the characteristic broadened emission band at about 740 nm from excited singlet and triplet states of C_{60} [116].

The fullerene layer was then gently pressed onto a clean SiO_2/Si substrate and peeled off again, so that the C_{60} was transferred to the silicon. These samples were then investigated with Raman and fluorescence spectroscopy, as shown in Figure 5-4, and compared with a control sample.

The control samples have a 10 nm thick layer of C_{60} that has been directly deposited onto a SiO_2/Si substrate in UHV. The Raman and fluorescence spectra of the transferred C_{60} are very similar to the spectra obtained when molecules were sublimed directly onto SiO_2. The major Raman peaks at 720, 1430, 1460, and 1760 cm^{-1} are at the same position and exhibit the same relative peak heights in both spectra. (The different Raman shifts for C_{60} are explained in more detail in section 3.4.) Also the characteristic broadened emission bands of C_{60} in the fluorescence spectra at about 740 nm match each other closely, indicating that the fullerene layer survives the etching and stamping process mostly unharmed. While the spectra of the control sample have uniform intensities across the surface, the spectra of the transferred fullerene layer vary in intensity indicating an irregular thickness of the C_{60}.

Raman and fluorescence spectra of the PDMS after the stamping were taken to investigate at the location of the remaining C_{60}. The spectra exhibit the typical C_{60} peaks as observed on the silicon substrate, again of varying intensity across the sample. This indicates that the C_{60} is broken apart irregularly during the stamping process, some C_{60} is transferred to the target substrate and some remains on the PDMS.

5.3. Transfer of molecular thin films and covalent networks

5.3.1. Steps of the transfer process shown for molecular thin films

A different, more complex way to utilize the adhesive properties of C_{60} is to transfer molecular thin films from a metal substrate to another surface. Tetra-(bromo-phenyl)-porphyrin (TBPP) and tetra-(bromo-phenyl)-porphyrinato-zinc

(TBPP-Zn) were chosen for these experiments, and are referred to as porphyrin monomers throughout the chapter. For the purpose of the transfer experiments both molecules are interchangeable: their fluorescence spectra are almost identical as shown in section 5.1, and both form similar continuous disordered networks via Ullman coupling as described in section 4.3. The transfer process for such a porphyrin thin film is depicted as a schematic in Figure 5-5. Alongside most of the individual steps of the transfer, control samples were produced to simulate the current state of the sample and monitor the process with respect to expected outcomes.

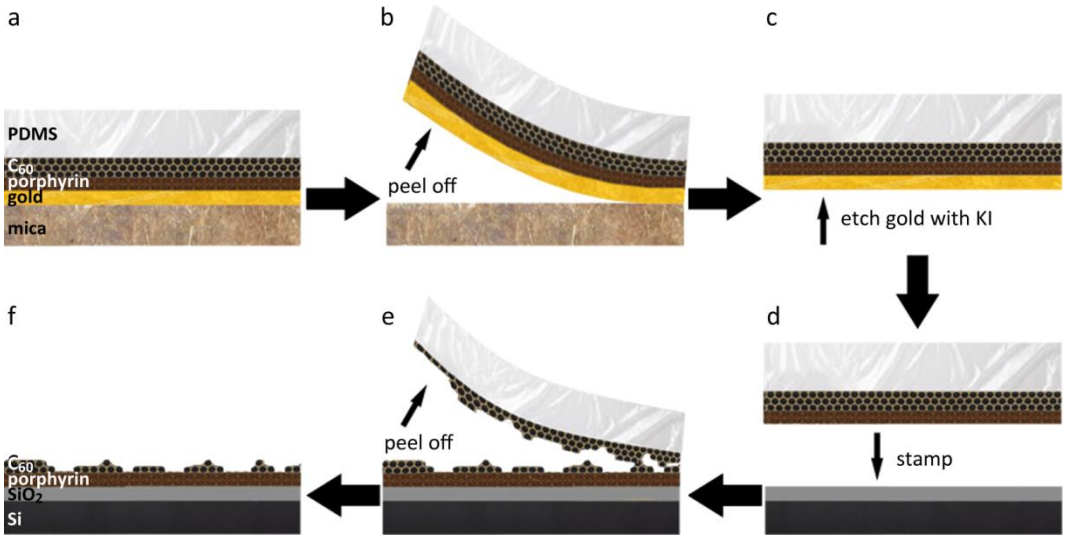

Figure 5-5: Schematic process for the transfer of porphyrin using C_{60} as an adhesive layer.

As before, the experiments start in UHV with a gold thin film on mica. The gold surface was prepared by repeated cycles of sputtering and annealing as described in Chapter 3 until a clear herringbone reconstruction pattern was observed with STM. Onto the gold substrate, held at room temperature, thin films of porphyrin monomers with thicknesses ranging from one monolayer to 10 nm were deposited via sublimation from a K-cell at deposition rates of 0.1 nm/min. On top of the porphyrin films 15 nm thick layers of C_{60} were deposited via sublimation from a K-cell at a deposition rate of 1 nm/min. In

addition to the adhesive effect of C_{60} the fullerenes also work as a buffer layer to protect the porphyrin when stamping it onto the target substrate. The samples were then taken out of the UHV chamber and coated with an approximately 1 mm thick layer of PDMS as described in section 5.2. The resulting sandwich is the starting point for the transfer process shown in Figure 5-5a.

After coating the sample in PDMS the gold/porphyrin/C_{60}/PDMS layer stack was manually peeled off the mica by carefully lifting it with a pair of tweezers, as depicted in Figure 5-5b. This step removed over 90% of the gold from the mica, leaving the gold exposed. The reliably successful near-complete removal of the gold layer comparable to the peeling described in section 5.2 indicates that the porphyrin thin film does not impair the peeling process.

Subsequently, the gold was etched using commercial gold etchant, an aqueous KI solution, as depicted in Figure 5-5c, until the gold layer is completely etched away, usually for 3 to 5 minutes. After removing the KI with a pipette, the sample was dipped into de-ionised water to remove excess KI and blow-dried with nitrogen. The exposed porphyrin layer was investigated with fluorescence spectroscopy and compared to a C_{60} control sample to verify the presence of the molecules at this stage in the transfer process.

Figure 5-6 shows fluorescence spectra for samples where one ML and 3 nm of porphyrin monomers were transferred to a PDMS substrate using a 15 nm layer of C_{60} as adhesive. The control sample was produced the same way as the other samples, only without the porphyrin layer. In the 3 nm porphyrin sample the characteristic porphyrin double peak is clearly visible. With a monolayer of porphyrin the C_{60} peak at ~740 nm dominates the spectrum in the region between 700 and 800 nm, but the first of the porphyrin double peak at 656±1 nm (Q(0,0)) can be detected in the spectrum. In samples with a thin porphyrin layer and a 15 nm layer of C_{60} the first porphyrin peak at 656±1 nm is a more

reliable indicator of the presence of porphyrin, the second porphyrin peak at 722±1 nm is too close and overlapping with the broad C_{60} peak at ~740 nm.

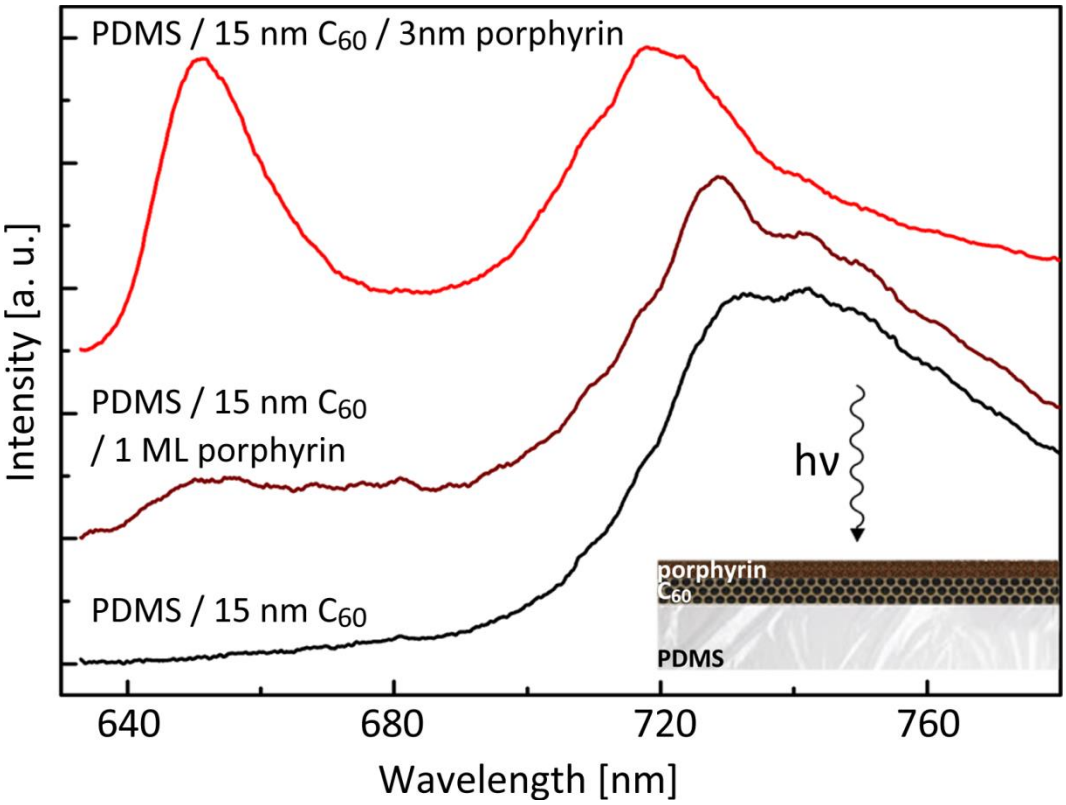

Figure 5-6 Normalised fluorescence emission spectra (excitation wavelength = 532 nm) of thin layers of tetra-(bromo-phenyl)-porphyrin over C_{60} on PDMS substrates during the transfer process; the characteristic double-peak at 656 ± 1 nm and 722 ± 1 nm of the porphyrin is dominant in thicker layers; in a monolayer of porphyrin the first peak at 656 ± 1 nm can just be resolved, while the second peak at 722 ± 1 nm is mostly covered by the broad C_{60} peak at about 740 nm.

The porphyrin/C_{60}/PDMS sample was then pressed onto the target substrate, namely thermal silicon with a 90 nm thick layer of thermally grown SiO_2 on top, and peeled off again. When peeling off the elastomer, the porphyrin and some of the C_{60} was transferred to the silicon surface, the rest of the fullerene layer remained on the PDMS. The sample was again investigated with fluorescence

spectroscopy to verify the success of the transfer and compared to spectra of control samples, as shown in Figure 5-7.

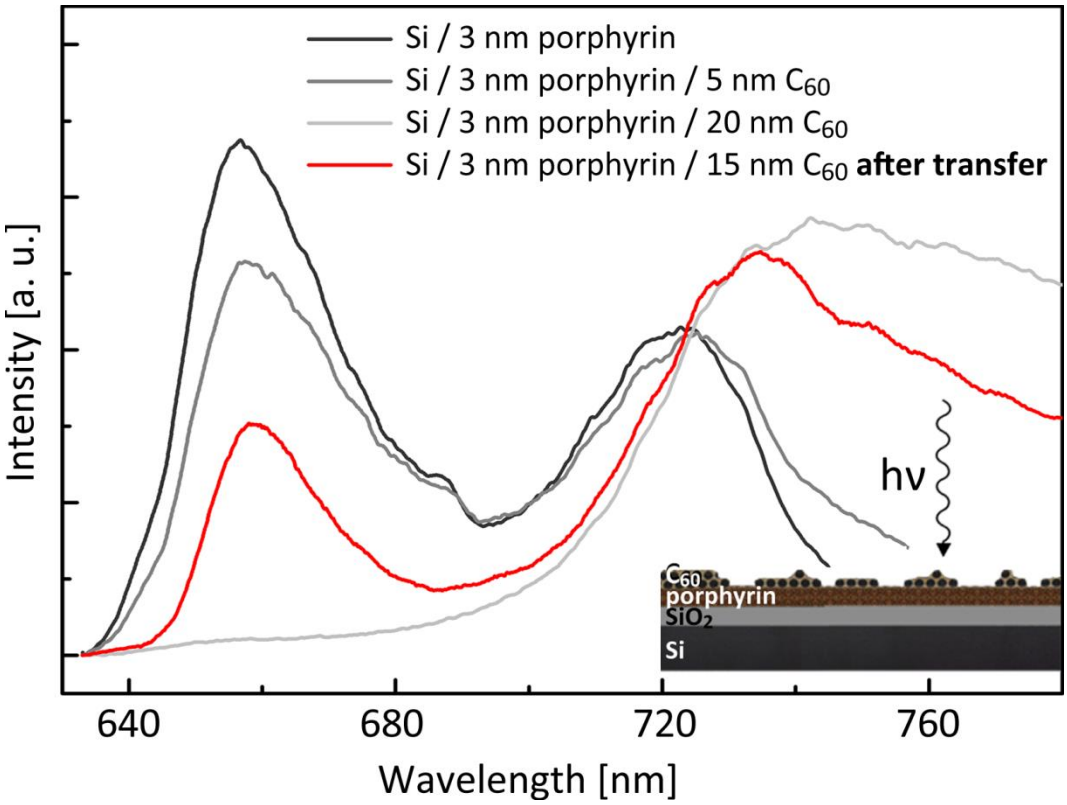

Figure 5-7: Normalised fluorescence emission spectra (excitation wavelength = 532 nm) of thin layers of tetra-(bromo-phenyl)-porphyrin covered by varying layers of C_{60} directly deposited onto SiO_2/Si substrates (grey) and a transferred thin layer of porphyrin (red).

To investigate how the expected fluorescence spectra of the samples after the transfer could look like, a set of control samples was produced by deposition of the layers that are expected after a successful transfer directly onto SiO_2. For that clean pieces of SiO_2/Si were inserted into the UHV chamber. Subsequently, 3 nm thick layers of porphyrin were deposited via sublimation from a K-cell at deposition rates of 0.1 nm/min and afterwards covered with 0 nm, 5 nm, or 20 nm C_{60} sublimed from a K-cell at a deposition rate of 1 nm/min. The spectra in Figure 5-7 show that porphyrin can still be detected if the C_{60} cover layer is

not thicker than 20 nm. The characteristic porphyrin double peak at 656±1 nm and 722±1 nm can clearly be observed when the porphyrin layer is covered by thin layers of C_{60} up to 5 nm. At a thickness of 20 nm the C_{60} signal with a very broad peak at ~740 nm dominates the spectrum, only the first porphyrin peak at 656±1 nm is just visible.

The ratio in intensities of the Q(0,0) peak to the C_{60} peak suggests that more than 5 nm of the originally 15 nm thick layer C_{60} were transferred from the PDMS onto the SiO_2/Si during the stamping on this area of the sample. Taking spectra at various points across the sample indicates that the C_{60} layer is broken apart irregularly during the peeling; the spectra exhibit peak ratios ranging from a 5 nm to a 15 nm thick cover layer of C_{60} on top of the porphyrin thin film. A more systematic investigation of the varying thickness of the C_{60} layer after the transfer via fluorescence spectroscopy maps will be discussed in the following chapter when covalent organic networks of monolayer thickness are transferred.

5.3.2. Transfer of covalent organic networks

The process of transferring thin molecular layers can be taken one step further when using materials for the transfer that have a higher thermal and chemical stability than C_{60}. In this case the fullerenes can be removed by annealing or with solvents without damaging the transferred layer, and the layer is left isolated on the new substrate. Polymerised organic monolayers meet the requirements of high chemical and thermal stability. The porphyrin monomers used for the transfer in the previous section can be polymerised by on-surface Ullmann coupling to form extended continuous disordered networks as described in detail in section 4.3. Slow deposition of TBPP and TBPP-Zn onto gold held at ~250°C and subsequent annealing at ~300°C leads to extended covalent networks as shown in Figure 5-8 and Figure 5-9, respectively.

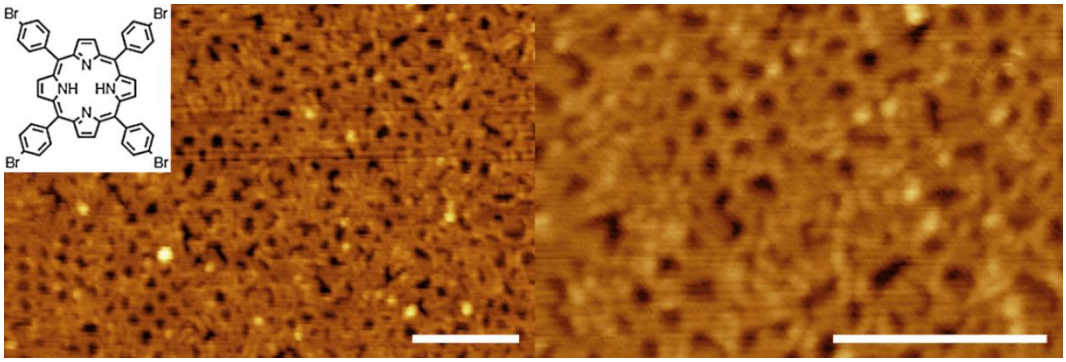

Figure 5-8: STM images (-1.5 V, 0.05 nA) of extended polymerized TBPP; scale bar 10 nm; inset: Structure of a TBPP monomer.

The STM images of the resulting surface for TBPP show small regions of local square order with lateral dimensions of about 5 nm within a disordered polymeric matrix. Due to the tip shape and scanning parameters the STM images in Figure 5-8 highlight the structure of the network.

A different tip shape and scanning parameters in the STM images in Figure 5-9 enabled submolecular resolution of individual porphyrin molecules.

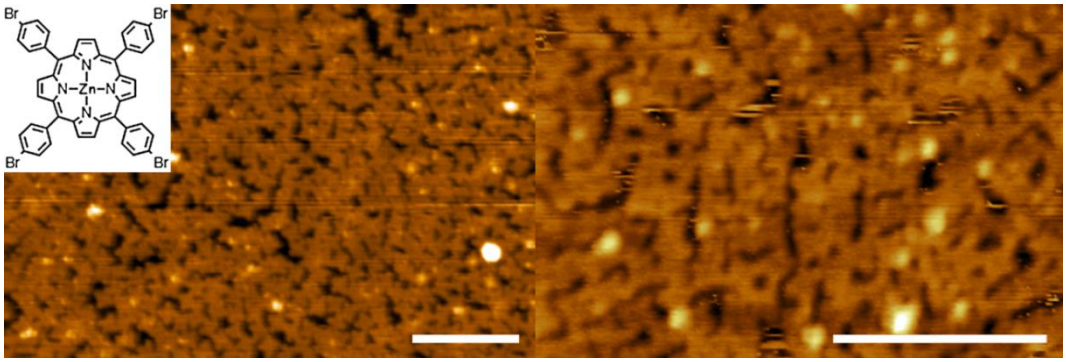

Figure 5-9: STM images (-1.7 V, 0.03 nA) of extended polymerized TBPP-Zn; scale bar 10 nm; inset: Structure of a TBPP-Zn monomer.

High symmetry and long-range order is not required in the polymers. The key factor for thermal and chemical stability is that the network is continuously covalently linked over large areas on the sample [117].

For the transfer of these continuous disordered networks a 15 nm thick layer of C_{60} was deposited onto the porphyrin and the network was transferred to Si/SiO_2 by peeling, gold etching, and mechanical transfer as described earlier. In order to demonstrate the effective transfer of the porphyrin polymer/C_{60} layers over large areas of the sample, fluorescence maps were taken over microscopic areas of 0.5 x 0.5 mm^2 across the centre region of the sample. Figure 5-10 shows maps of the fluorescence intensity at wavelengths corresponding to the first of the two porphyrin peaks at 655 nm (Q(0,0), Figure 5-10a) and the peak around 740 nm associated with C_{60} (Figure 5-10b). These maps confirm that porphyrin, together with C_{60}, was transferred over large areas of the sample. Prior to annealing, a variation in intensity of the Q(0,0) peak shown in Figure 5-10a was observed across the surface. This can be attributed to the attenuating effect of the residual C_{60} layer of varying thickness across the surface.

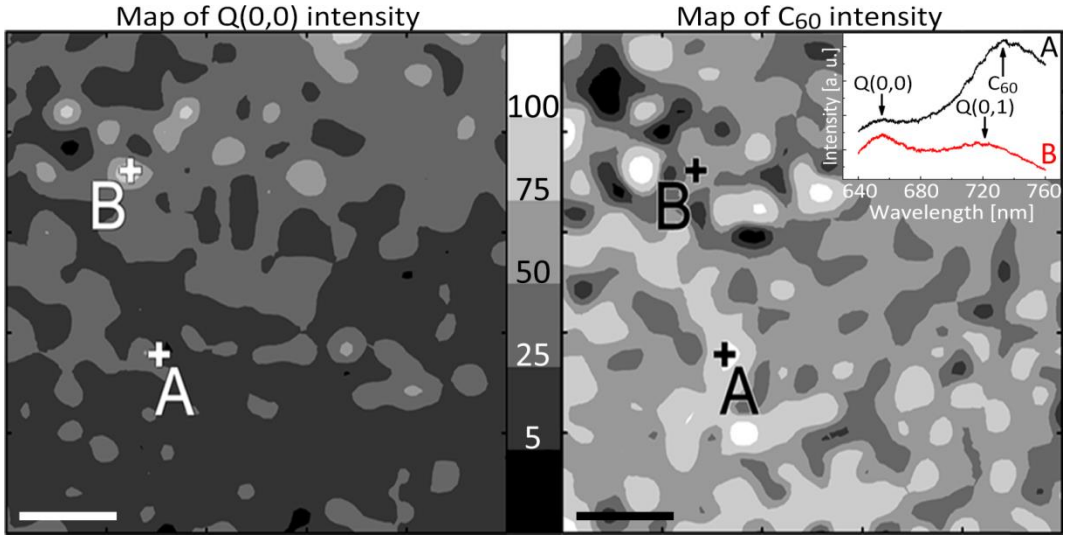

Figure 5-10: Fluorescence emission spectroscopy maps over 0.25 mm^2 (excitation wavelength = 532 nm) of transferred polymerised TBPP-Zn networks after the transfer onto SiO_2, scale bar 100 µm; insert: selected spectra of points A and B on the maps.

This hypothesis is consistent with a comparison of spectra taken at positions A and B, shown in the inset of Figure 5-10b, with spectra taken from control

samples of C_{60} films of varying thicknesses, shown in Figure 5-7, implying that during the transfer the C_{60} layer is broken apart irregularly. Dark areas in Figure 5-10a show regions where there was either no porphyrin transferred, or there is a very thick layer of C_{60}. In medium grey regions, for example around point A, porphyrin was successfully transferred, but is covered by a few nm of C_{60}. The peak-to-peak ratio of the two porphyrin peaks in light grey regions fits the fingerprint spectrum of porphyrin without C_{60}, as shown for point B.

Due to the thermal and chemical stability of the covalent bonds linking neighbouring porphyrins, the residual C_{60} can be removed by either annealing the sample in high vacuum or with solvents such as toluene or carbon disulfide without removing the polymeric network. While solvent cleaning is much faster than annealing, it also exposes the sample to another chemical, while annealing takes longer, it also is cleaner and easier tuneable. Test samples of 15 nm thick layers of C_{60} transferred onto SiO_2/Si were produced and cleaned both with solvents and by annealing and investigated with optical microscopy.

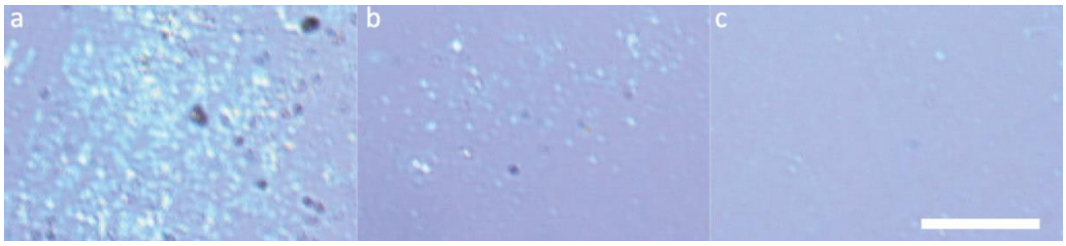

Figure 5-11: Optical microscopy images of a transferred fullerene layer before any treatment (a), after dipping in toluene for 30 sec (b), and after annealing in HV at 300°C for 120 min (c); the light blue patches are C_{60} islands; scale bar 50 µm.

Figure 5-11a shows the surface before removing the C_{60}. Large islands on the surface appear as bright features under the microscope and have a typical diameter of 1 to 5 µm. When rinsing the sample in toluene for 30 seconds, most of the C_{60} is removed, only few small islands remained, as shown in Figure 5-11b.

An alternative way of removing the residual C_{60} after the transfer is annealing. The sample was inserted into a high vacuum chamber (base pressure 10^{-6} mbar) and annealed at 300°C for 120 minutes. Although this method takes longer, it leads to a cleaner surface, as shown in Figure 5-11c, and does not require the use of further chemicals. Similar experiments were conducted on porphyrin monomer thin films deposited directly onto SiO_2/Si and covered by 15 nm of C_{60}. With those samples solvent or annealing treatment resulted in complete removal of the molecular thin film. That is not a surprising result, since the sublimation temperature of porphyrin in UHV is about 100°C lower than the sublimation temperature of C_{60}. After reviewing the microscopy results annealing in high vacuum was chosen as the preferred method for the removal of fullerenes. After the first set of fluorescence maps the samples were inserted into a high vacuum chamber (base pressure 10^{-6} mbar) for annealing. The temperature was slowly increased over 180 min, then held at 200°C for 120 min, and finally left to cool down to room temperature over 60 min.

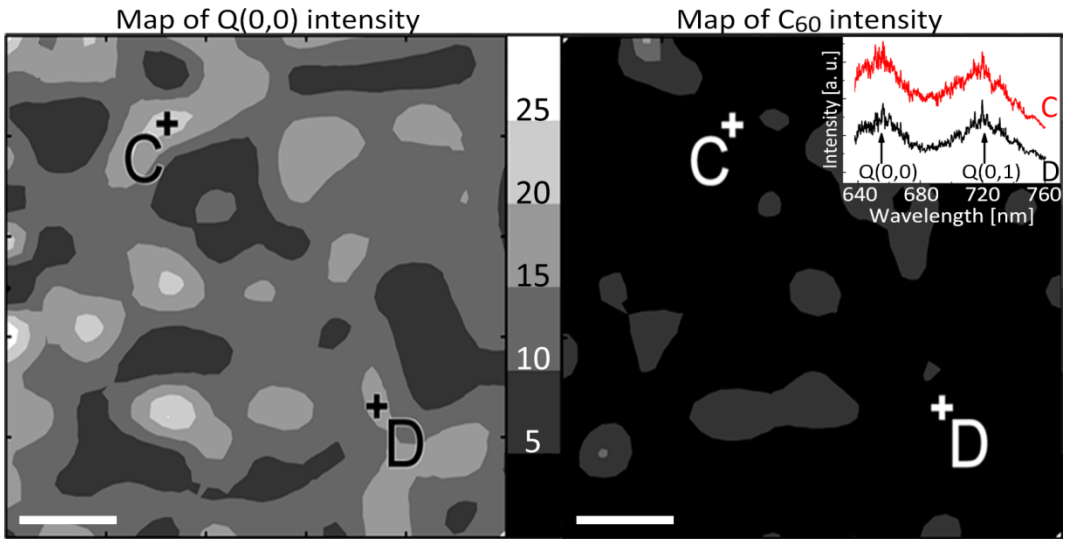

Figure 5-12: Fluorescence emission spectroscopy maps over 0.25 mm² (excitation wavelength = 532 nm) of transferred polymerised TBPP-Zn networks after thermal desorption of the fullerene layer; scale bar 100 µm; insert: selected spectra of points C and D on the maps.

Figure 5-12 shows a new set of fluorescence spectroscopy maps of the same area as before obtained after extracting the sample from the vacuum chamber. The map in Figure 5-12a shows that the porphyrin is still present on the surface with near homogenous intensity, while the map in Figure 5-12b shows that the fullerene has been almost completely removed from the surface. The characteristic double peak at 655±1 nm for Q(0,0) and 720±1 nm for Q(0,1) in the fluorescence spectra of the polymerised porphyrin is present across over 90% of the mapped area, two example spectra are displayed in the inset in Figure 5-12b.

The spectra of transferred porphyrin two-dimensional polymers are similar in shape to those of transferred or sublimed porphyrin monomer monolayers; the peaks are observed at, within experimental error, the same wavelength as the monomer.

5.4. Conclusions and outlook

In conclusion we have shown that C_{60} shows an unexpected mechanical adhesion which is sufficiently strong to promote the removal of a metal film from a mica substrate. Furthermore this route may be used to remove molecular thin films from a metal substrate through a process of mechanical removal followed by etching, and also to transfer them to a dielectric surface. The method is demonstrated for a SiO_2 substrate but is expected to be compatible with other dielectrics. The process is effective for films with thickness as small as a monolayer and has been demonstrated as route to isolate two dimensional polymers formed by on-surface synthesis, allowing an investigation of their functional properties.

Chapter 6

Molecular trapping in stacked porphyrin nanorings

6.1. Introduction

As a route to tailor molecular surface structures, non-covalent interactions have been exploited for the formation of a wide variety of two-dimensional supramolecular networks with specific dimensions, symmetry, and functionality. Typically the building blocks in these structures are small, rigid molecules, but there has recently been growing interest in the adsorption and on-surface synthesis of much larger and more flexible species, such as extended one-dimensional polymers and other molecules which exhibit conformational freedom [117, 118]. The exact conformation of an adsorbed macromolecule or polymer is difficult to control since the intramolecular elastic energy associated with the inherent flexibility of the molecule can be comparable with intermolecular and molecule-surface interactions. The first half of this chapter shows that non-covalent interactions may be used to control the shape of flexible polymers by exploiting a newly observed, and unexpected, supramolecular organization of cyclic porphyrin nanorings into stacked columns. The nanorings are deposited using electrospray, and the stacking arises from aggregation in the solvent prior to deposition which is preserved after deposition. The stacking results in an increase in the bending stiffness of the polymer nanorings and a transition to a near circular shape.

Porphyrin molecules are also of great interest due to their optoelectronic properties and have been investigated widely across the physical and biological sciences [35]. In recent work the synthesis of a new type of porphyrin-derived nanostructure, a cyclic polymer nanoring, has been demonstrated [42, 43]. These butadiyne-linked nanorings are synthesized using a template directed strategy, via the formation of Vernier self-assemblies, as described in detail in section 2.2. These new materials attract great interest due to the delocalized nature of their molecular orbitals and their similarity to the biological light-harvesting complexes LH1 and LH2 [119]. Using the Vernier-templating approach, it is possible to synthesize nanorings with a high level of control over

the number of porphyrin groups, and it has been possible to isolate cyclic structures with 6, 8, 12, 16, 18, 24, and 30 porphyrin units. In a cyclic porphyrin nanoring each porphyrin macrocycle is linked to two neighbouring porphyrins by butadiyne linker groups. A schematic diagram of c-P24, the nanoring with 24 linked zincato-porphyrins, is shown in Figure 6-1a and b. Octyloxy side chains are attached to the porphyrin macrocycle via aryl groups to promote solubility. The centre-to-centre porphyrin spacing in analogue linear polymers is 1.33 nm [118], implying a diameter of 10.16 nm (the separation of diametrically opposed Zn atoms) for c-P24 assuming a circular conformation.

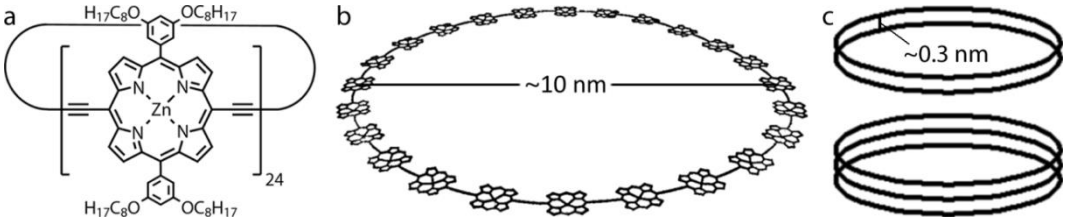

Figure 6-1a: Chemical structure of c-P24; b: Schematic structure of a c-P24 nanoring without side groups, diameter ~10 nm; c: Diagram of a double stacked and a triple stacked nanoring with a layer spacing of ~0.3 nm.

The formation of arrays of nanopores which have the potential to trap and organise adsorbed guest molecules has been widely studied as a route to combine spatial organisation and chemical functionalization on a surface. This has been successfully achieved using nanoporous templates stabilised by hydrogen bonding, metal co-ordination and covalent coupling, both in solution and in vacuum. In most cases the nanoporous networks have a height corresponding to a single monolayer [3, 120].

The second part of this chapter explores the capture of molecules within a trap formed by single as well as stacked layers of porphyrin nanorings with diameters up to 10 nm and heights of up to 1 nm, as shown in Figure 6-1c. There are significant differences between the statistics of the capture of sublimed C_{60} molecules depending on both height and diameter of the traps.

6.2. Electrospray deposition of porphyrin nanorings

The cyclic porphyrin oligomer c-P24 is investigated using STM following deposition of the nanorings onto a Au(111) surface using electrospray. This technique permits the direct transfer of large molecules, which are not compatible with sublimation, from solution into an ultra high vacuum system, as described in section 3.2.3. The porphyrin nanoring of primary interest in this chapter is the molecule c-P24 which consists of 24 porphyrin subunits and has a diameter, assuming a circular conformation, of approximately 10 nm.

Before the molecule c-P24 was deposited onto the the Au(111) on mica substrate, the surface was cleaned by repeated cycles of Ar ion sputtering (6×10^{-6} mbar, 0.8 keV, ~3 μA) for 30 min and subsequent annealing at 500°C for 20 min with a controlled slow cooling down to room temperature over 20 min, until a clear herringbone reconstruction was observed. For the electrospray deposition the solution concentration was 100 μg/ml c-P24 in a methanol/toluene mixture (1:3 by volume). The solution was passed at a flow rate of ∼10 μL/min through a stainless steel emitter held at ∼1.8 kV under atmospheric conditions for 5 minutes. A highly directional jet of droplets then entered the vacuum system via a narrow capillary tube, and then passed through differentially pumped chambers before impinging on the gold substrate. During the deposition the pressure in the preparation chamber rose from a base pressure of 10^{-10} mbar to the high 10^{-6} mbar range. The surface was then investigated with STM in the same vacuum chamber.

The STM topograph in Figure 6-2 shows nanorings adsorbed on step edges of the Au(111) surface where 24 individual porphyrin units that constitute one nanoring can be clearly resolved. The conformation for c-P24 shows a significant deviation from a circular shape due to the inherent flexibility of the nanorings. For example, the nanoring in the centre of Figure 6-2 has long and short axes equal to 13 and 6 nm, respectively.

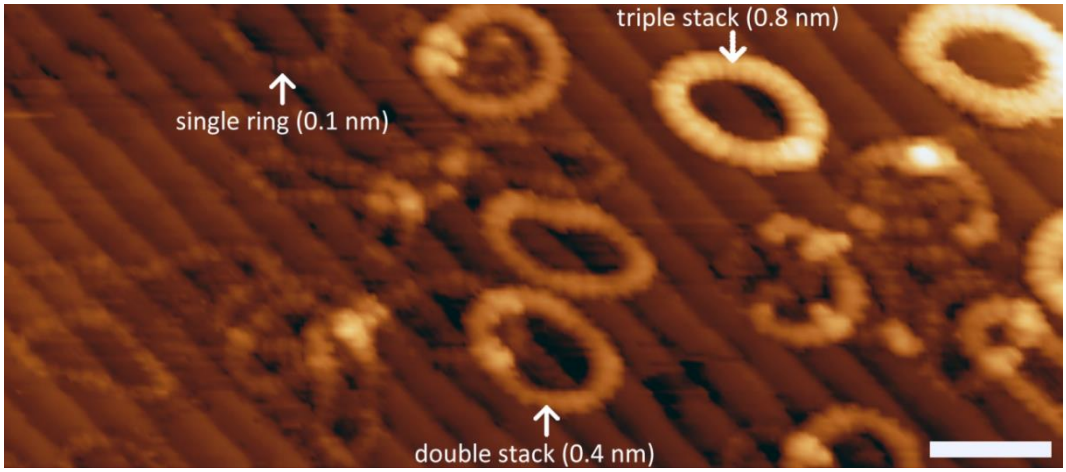

Figure 6-2: STM image (-1.7 V, 0.03 nA) of c-P24 nanorings on Au(111) deposited via electrospray deposition; scale bar 10 nm.

In addition to the deformation, different apparent heights, 0.1, 0.4, and 0.8 nm, respectively, of the nanorings are observed, in good agreement with previous work published on stacked cyclic porphyrin nanorings [121]. Examples of these heights are marked in Figure 6-2. In the nanorings of each apparent height 24 porphyrin subunits can still be resolved.

The height of 107 rings across 20 STM images was measured and is plotted in Figure 6-3.

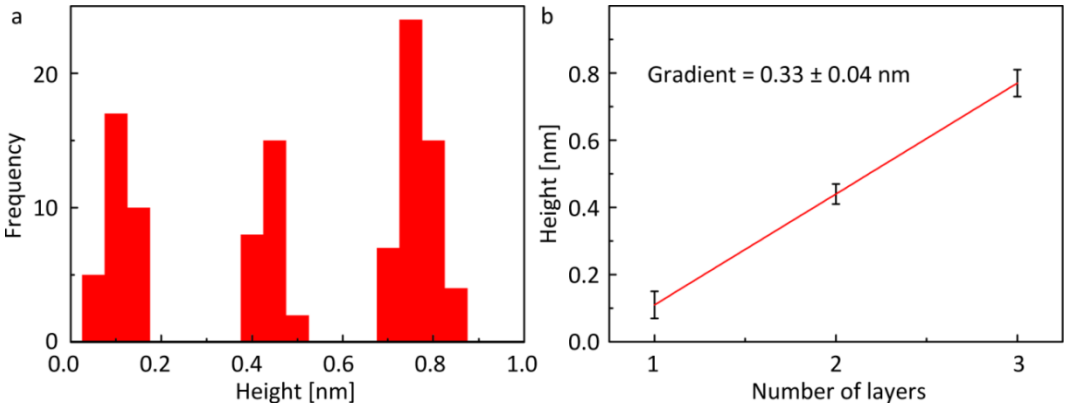

Figure 6-3a: Histogram of c-P24 nanoring heights; b: Average height of the clustered values versus the peak number.

The histogram in Figure 6-3a shows that nanoring heights are clustered around discrete values, and therefore the higher features are attributed to stacks of two and three nanorings. In Figure 6-3b the average height of the nanorings within the clusters is plotted versus peak number. It is found to be linear within errors with a gradient, corresponding to the layer spacing in the stacks, of 0.33 ± 0.04 nm. This value is consistent with parallel alignment of porphyrin groups and stabilization of the stacked nanorings by π-π interactions [121, 122]. The gradient does not intersect with the origin, because the apparent height of the gold substrate cannot be directly compared to the apparent height of the porphyrin stacks in STM experiments, as explained in section 3.3.

Also present on the surface are partially overlapping nanorings, a few examples can be observed in Figure 6-2 on the left. The height of the crossing points of two single layer rings corresponds to that of a double layer stacked ring, providing further evidence that the high contrast nanorings arise from stacking.

6.3. Adding fullerenes

The variable height of the columnar stacks facilitates a study of the influence of the vertical dimension (perpendicular to the substrate) on the capture of guest molecules by a supramolecular trap. After the characterisation of the nanorings with STM, C_{60} was deposited by sublimation from a Knudsen cell at deposition rates of ~0.01 ML/min.

Figure 6-5 shows STM images of the surface following the deposition of c-P24 followed by 20 min (a), 40 min (b), 60 min (c), and 80 min (d) deposition of C_{60}. With a deposition rate of 0.1 ML/min, the expected coverage of C_{60} molecules is 0.2 ML (a), 0.4 ML (b), 0.6 ML (c), and 0.8 ML (d). The nanorings are clearly resolved as cyclic structures as described in the previous section. Also apparent in the images are rows of C_{60} molecules which are, for low coverages

as seen in Figure 6-5a, predominantly adsorbed either along step edges on the Au(111) surface, or as islands nucleated within the nanorings. With increasing coverage large islands also grow outside the nanorings as well, as can be observed in Figures 6-5 b to d.

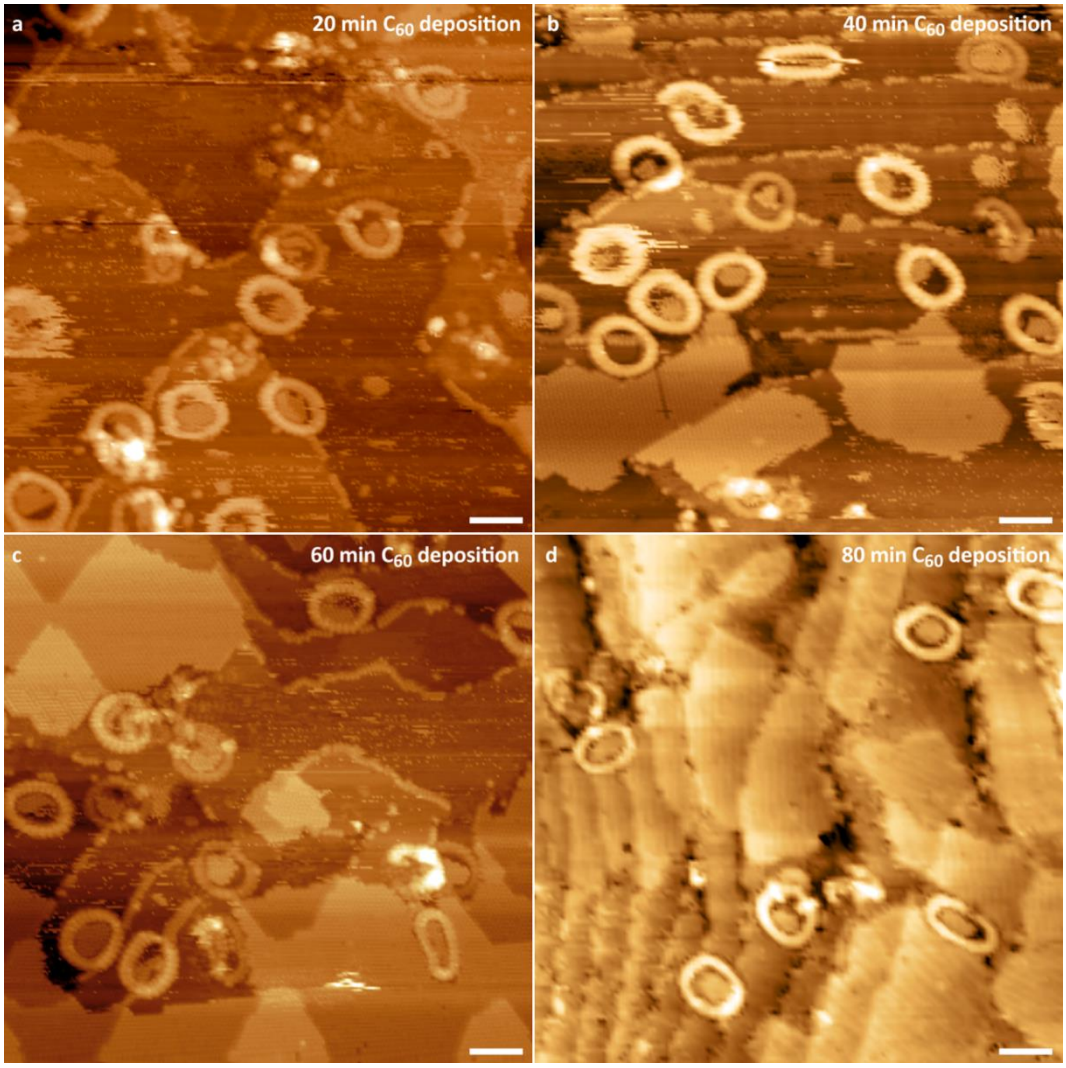

Figure 6-5: STM images (-1.7 V, 0.03 nA) of c-P24 porphyrin nanorings deposited via electrospray deposition and subsequently sublimed C_{60} for stepwise increased coverage; scale bar 10 nm.

The apparent ring height of the stacks in all images after the sublimation of C_{60} is decreased by approximately 0.15 nm compared to the images in the

previous section. In the lower left of Figure 6-6 a triple height nanoring is clearly resolved and is identified by the red line along which a height profile is extracted and shown in the inset of Figure 6-6. A height profile is also shown for a double height nanoring (upper left; purple line profile); this nanoring straddles a step edge of the Au(111) surface. A monolayer nanoring in the top right corner of the image appears as depression around captured C_{60}.

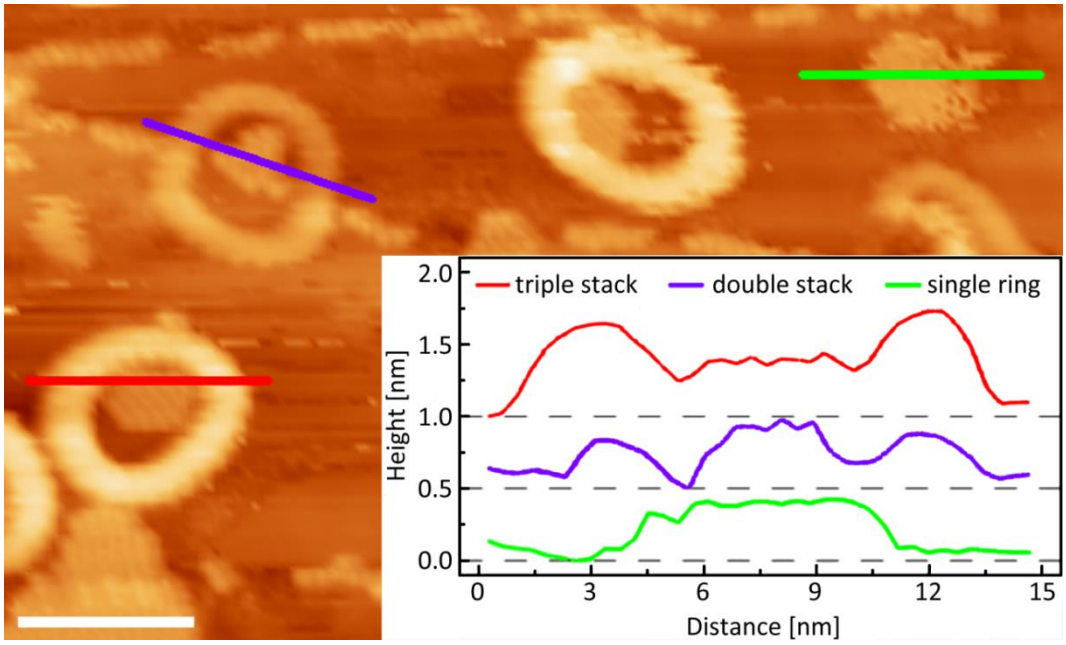

Figure 6-6: STM image (-1.7 V, 0.03 nA) of c-P24 porphyrin nanorings deposited via electrospray deposition and subsequently sublimed C_{60} (40 min); profile lines indicated; scale bar 10 nm; inset: Profiles through porphyrin nanorings of variable stacking height partially filled with C_{60};

In each of these nanorings there is captured C_{60}, arranged in hexagonal close packed islands. The single C_{60} molecules can be resolved individually in the images and in the profile lines. A C_{60} molecule has an effective height, from the line profiles of ~ 0.4 nm and is approximately the same for each ring. This effective height for the C_{60} is close to that expected from previous studies [123].

In contrast the height of the enclosing nanoring differs significantly. For the triple stacked ring a height of 0.65 nm was measured, whereas for the double stacked ring a height of 0.3 nm, and for the monolayer, a depression of ~0.05 nm was measured. The difference in height between stacked rings with different numbers of layers is close to a multiple of 0.33 nm, the same as without C_{60}. The absolute heights of the stacked nanorings however are lower by approximately 0.15 nm. This systematic difference is attributed to variations in the termination of the STM tip as compared with the experiments in section 6.2. In particular, it is possible that in these experiments C_{60} was transferred to the tip.

6.4. Analysis and statistics of the STM images

After a series of sequential depositions, the variation of the effective coverage of C_{60} inside and outside the nanorings was determined. As expected, the C_{60} coverage outside the nanorings shows a linear dependence with cumulative deposition time. To determine this value only the parts of the overall area not covered or enclosed by nanorings were taken into account. The proportion of this fraction of the surface covered by C_{60} was then plotted, as shown in Figure 6-8. The coverage within the nanorings is determined as a fraction of area of the enclosed C_{60} island divided by the pore area of the individual ring, which varies due to shape distortion. For the pore area – the cavity of the nanoring – the dark contrast area enclosed by the inner perimeter of the nanoring was measured.

From Figure 6-8 it is clear that there is an enhanced probability of fullerene adsorption within the nanorings. In addition, the capture probability is highest for the monolayer rings, with the higher, stacked rings having a capture probability intermediate between that of the monolayers and the surrounding gold surface. These observations are consistent with an enhanced nucleation rate for C_{60} island formation within the nanorings which might arise, for example, from an enhanced residence time of a molecule within the nanoring.

This might be expected due to the interaction of the C_{60} with the internal edges of the nanoring and is also consistent with a barrier for molecules to diffuse over the nanoring and escape from the local trapped region. The reduction of relative coverage for higher, stacked rings is likely due to a larger barrier for molecules to overcome to enter into to the nanopore.

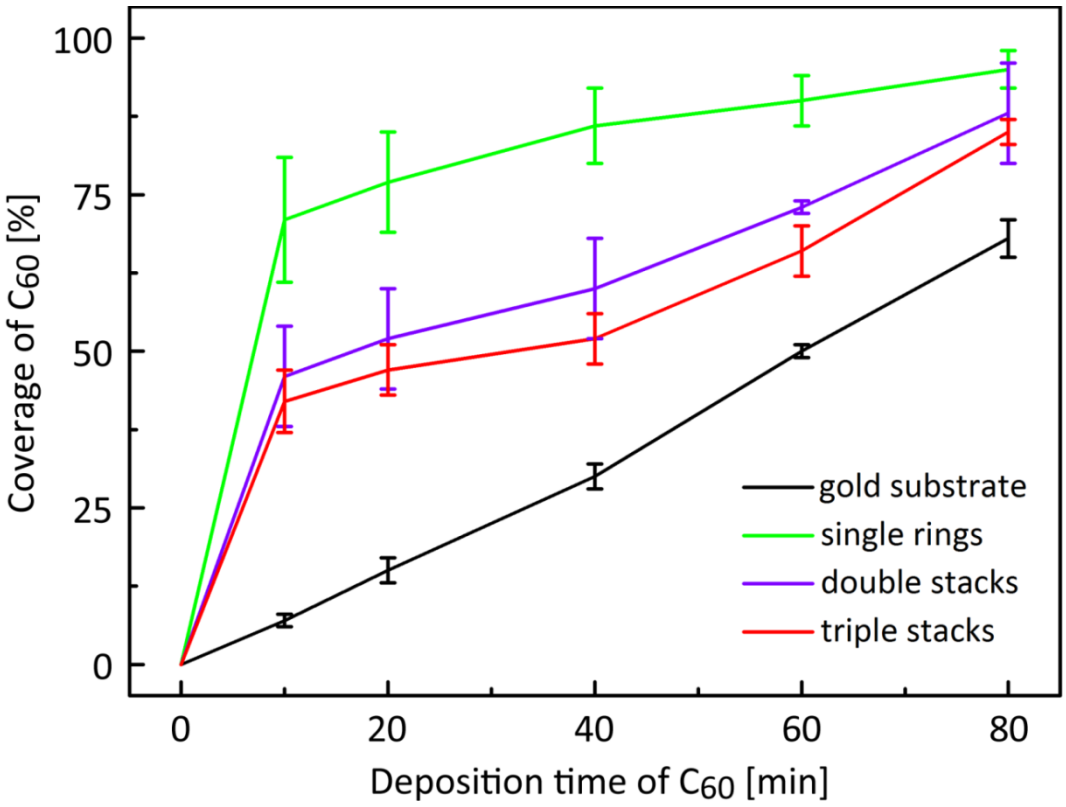

Figure 6-8: Coverage of C_{60} inside and outside the porphyrin nanorings with increasing C_{60} deposition time.

Furthermore, the density within nanorings of all heights is significantly greater than the surrounding region, particularly at low coverage, implying that at least some of the captured molecules must be incident elsewhere on the surface and diffuse before becoming trapped in the nanoring.

The capacity of c-P24 is significantly less than that expected from the geometric radius of c-P24, 5 nm. The observed effective radius is about 3.4 nm, and the difference, 1.6 nm, is very close to the length of the aryl side chains

attached to the porphyrin macrocycles. This suggests that these sidegroups are adsorbed in a quasi-linear conformation which spread radially across the surface forming a region at the inner perimeter of the ring where it is not energetically favourable for C_{60} islands to grow.

This deviation from a circular shape influences the capacity of C_{60} molecules that fit in the nanopore. A few examples are shown in Figure 6-9. A circular nanoring (ratio of long axis to short axis of a nanoring is 1:1) can hold 37 C_{60} molecules, consistent with the measured maximum cavity size of 38 nm^2. The capacity of the nanoring decreases rapidly with deviation from a circular shape. An ellipse with a ratio 1:2 for short axis to long axis can only hold 24 C_{60} molecules. Most observed nanorings exhibit more irregular, oval perimeters.

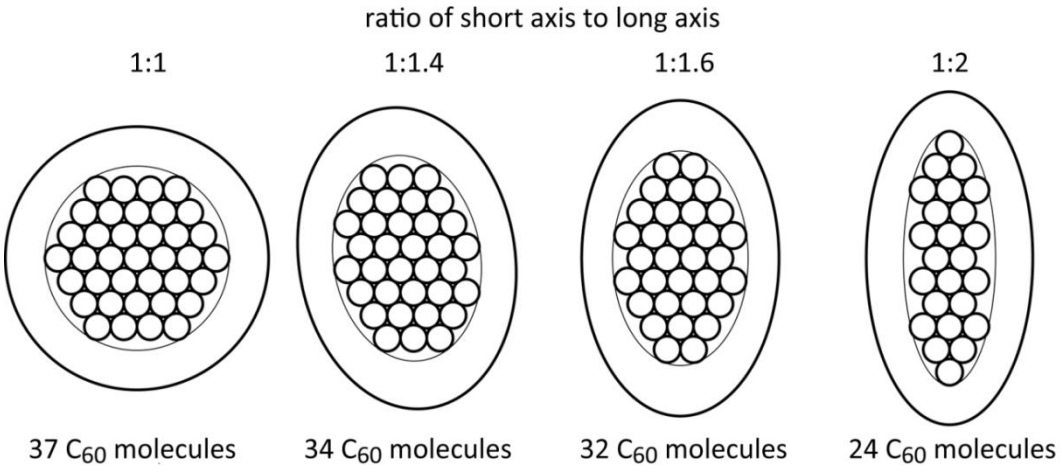

Figure 6-9: Schematic filling configurations for circular and elliptical c-P24 nanorings, the thick line indicates the perimeter of the nanoring through the centre of the porphyrin molecules, the thin line indicates the inner perimeter of the exclusion zone.

An example is shown in Figure 6-10, a zoomed in image of a nanoring with an enclosed C_{60} island, taken from Figure 6-5c in the lower left corner. In this image it is possible to resolve both individual C_{60} molecules and also the porphyrin sub-

units within the nanoring; the latter are associated with the regular contrast variation around the perimeter of the nanoring and it is possible to confirm that, as expected, there are 24 groups.

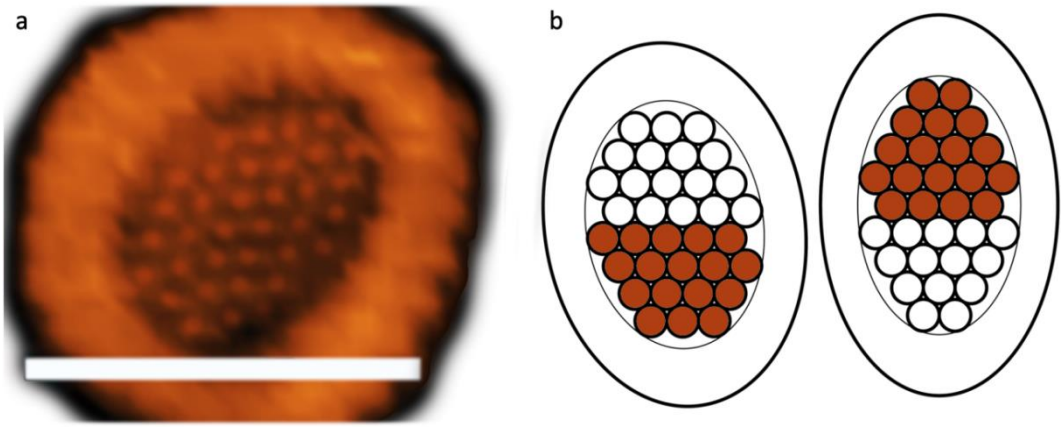

Figure 6-10a: Zoomed in STM image (-1.7 V, 0.03 nA) of a c-P24 porphyrin nanoring filled with C_{60} as observed in Figure 6-5c, scale bar 10 nm; b: schematics of elliptical nanorings filled with C_{60}; the highlighted circles indicate the configuration of the island observed in the STM image.

The image also shows that C_{60} molecules within the nanoring adopt the expected hexagonal close packed structure. In this case the island contains 35 C_{60} molecules and exhibits a hybrid island conformation of two of the examples shown in Figure 6-9 fitting its egg-shaped perimeter. In addition, the low 1.5 nm wide contrast gap between the C_{60} molecules and the centre of the porphyrin groups can clearly be resolved in this image, what is attributed to the excluded area for C_{60} within the ring.

6.5. Comparison with c-P12

The smaller c-P12 molecule was deposited the same way as c-P24 via electrospray deposition. Figure 6-11 shows an STM image of c-P12, the nanoring with 12 porphyrin units on Au(111).

The herringbone reconstruction of the gold surface can be observed in the image. The nanorings can clearly be distinguished from the substrate, it is possible to count the 12 porphyrin monomers in some of them.

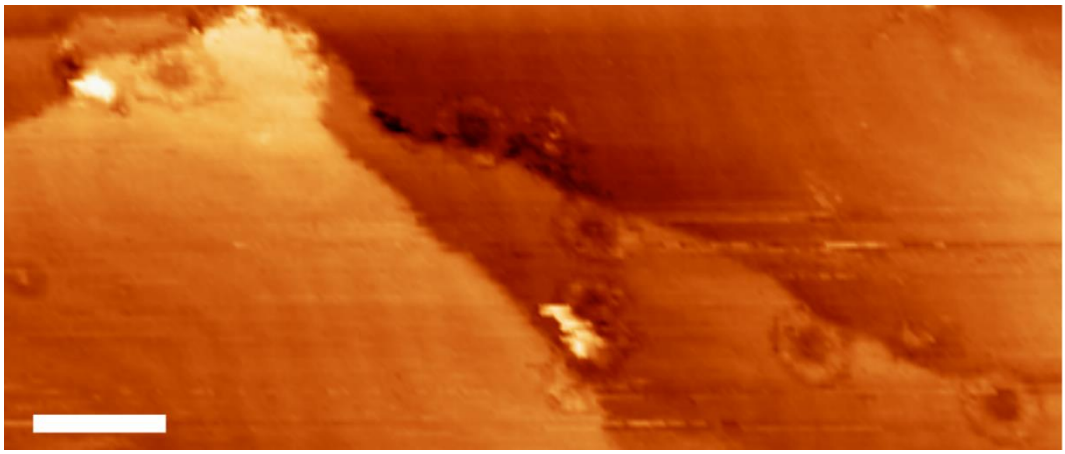

Figure 6-11: STM image (-1.7 V, 0.03 nA) of c-P12 nanorings on Au(111) deposited via electrospray deposition; scale bar: 10 nm.

There are similarities and differences when comparing c-P24 and c-P12. Like with c-P24, in c-P12 the constituent porphyrin groups lie parallel to a supporting substrate (Au(111)), the apparent height in the STM images of the rings is the same. Unlike the larger c-P24, c-P12 adopts a near-circular conformation with a diameter of approximately 5 nm. The deviation from circular conformation is much reduced. Another striking difference is that, unlike c-P24, c-P12 does not form stacks. All rings on the surface have the same apparent height of 0.1 nm. The rings are predominantly observed at step edges. These results also agree with the experiments on c-P12 reported by Svatek *et. al.* [121].

Subsequently C_{60} was deposited onto the c-P12 nanorings in a similar set of experiments to the c-P24 nanorings described earlier. However, sequential deposition of C_{60} onto the smaller c-P12 porphyrin nanorings lead to different results. First, a layer of c-P12 nanorings was deposited with electrospray deposition, followed by deposition of C_{60} via sublimation. Figure 6-12 shows STM images acquired after deposition of C_{60} for 40 min (a) and 80 min (b).

For the lower coverage of 0.4 ML C_{60} shown in Figure 6-12a a preference for C_{60} adsorption in regions outside the nanorings is observed. In particular it is clear that even where the local coverage of C_{60} is very high, within a hexagonally close packed island, C_{60} is not present within the nanoring. In fact for this particular nanoring there is no captured C_{60} and the nanoring is embedded within a fullerene island which has grown around it (note that the porphyrin sub-units of the nanoring can be resolved in this image). At higher coverage (0.8 ML C_{60}) shown in Figure 6-12b, C_{60} islands grown around the nanoring can be observed. In this case, however, three C_{60} molecules are trapped within the nanoring.

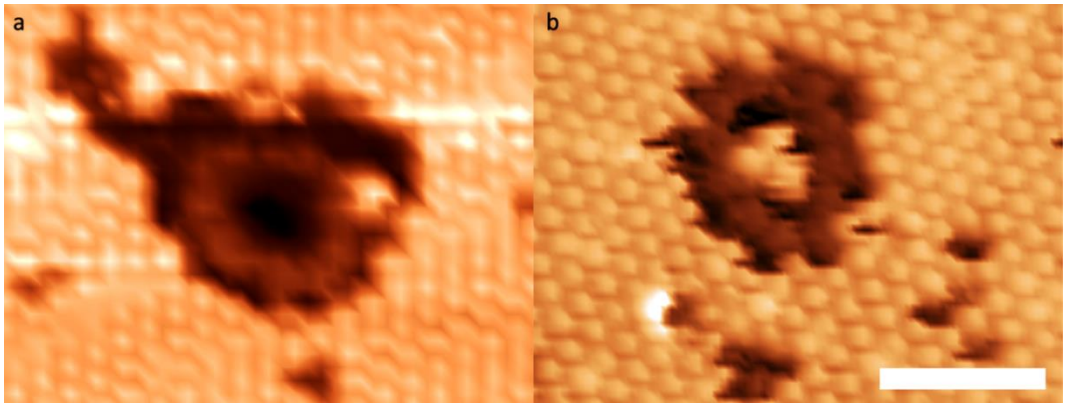

Figure 6-12: Zoom into STM images (-1.7 V, 0.03 nA) of c-P12 deposited via electrospray deposition and subsequently sublimed C_{60} for 40 min (a) and 80 min (b); scale bar 5 nm.

The very low fraction of captured C_{60} within the c-P12 nanorings is consistent with the excluded region observed for the c-P24. Since a denuded region within ~1.6 nm of the centre of the porphyrin macrocycle is expected, the effective trapping radius of a nanoring is reduced from the geometric radius (2.5nm) to about 0.9 nm. The effective area of a circular region with this radius is hence ~2.5 nm^2, which corresponds to ~ 2.9 A_{mol}, where A_{mol} is the area occupied per C_{60} molecule in a hexagonally close-packed layer. This is consistent with the observation of a maximum of three captured C_{60} molecules.

The absence of C_{60} in c-P12 at lower overall coverage implies that there are more favourable bonding sites available at low coverage. This is in contrast to c-P24 and is, at least partially, due to the lower co-ordination of trapped molecules in c-P12. Since only 3 molecules may be accommodated the maximum co-ordination is 2, much lower than for the clusters in c-P24 and elsewhere on the surface.

6.6. Transfer of porphyrin nanorings

Unlike the porphyrin monomers and polymers discussed in section 3.4, porphyrin oligomers covalently connected via butadiyne linker groups exhibit a characteristic Raman signal. This is of advantage in tracking the success of the transfer of molecular thin films. Thin layers of porphyrin nanorings for transfer were prepared via immersion instead of electrospray deposition. Immersion allows an even coverage across the whole surface, which is favourable over the uneven distribution of electro-sprayed molecules for the transfer and spectroscopy experiments. A thin film of c-P24 in solution with a concentration of 100 µg/ml in a methanol/toluene mixture (1:3 by volume) was produced on flame-annealed gold by immersion for 30 min. Raman spectra were obtained from the surface prior to transfer, as shown in Figure 6-13. The molecular thin film was subsequently transferred from the gold substrate to PDMS. The method used is similar to the transfer method established in Chapter 5. The sample was inserted into a UHV chamber (base pressure 10^{-10} mbar) and 15 nm of C_{60} were deposited via sublimation from a Knudsen cell onto the sample at a deposition rate of 1 nm/min. The sample was removed from UHV and an approximately 1 mm thick support layer of PDMS is deposited onto the sample and cured in the oven at 150°C for 15 min. After the sample has cooled down, the PDMS/C_{60}/nanorings/gold layer stack can be lifted from the mica, leaving the gold exposed. The gold was etched in aqueous KI for 3 min. The exposed nanorings/C_{60} layers on PDMS were investigated with Raman spectroscopy, as shown in Figure 6-13. To determine the contribution to the Raman signal from

the C_{60} and PDMS layers, a control sample was produced the same way as described above, only without the porphyrin nanoring layer.

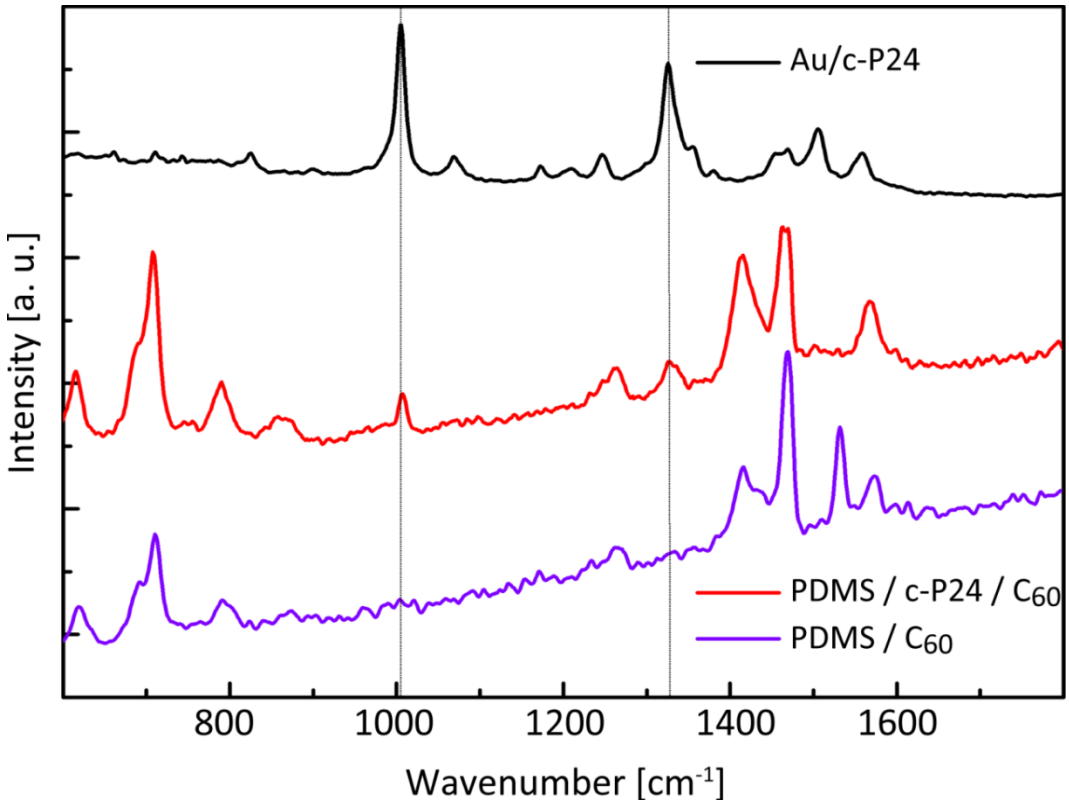

Figure 6-13: Raman spectra of c-P24 nanorings before the transfer (black line) and after the transfer (red line); control spectrum of transferred C_{60} without nanorings (purple line) shows the contribution of PDMS and C_{60} to the spectra.

The spectra show that two distinct peaks at ~1000 cm^{-1} and ~1330 cm^{-1} are present on both the gold sample prior to transfer as well as after the transfer on PDMS, but not on the PDMS/C_{60} control sample. Thus, these peaks are allocated to Raman shifts of the porphyrin nanorings. Neither PDMS nor C_{60} contribute to the signal in those regions, indicating a successful transfer of nanorings.

To obtain a spectrum of the nanorings only, control samples were produced on a silicon substrate. The samples were prepared the same way, via immersion of thermally grown SiO_2/Si (oxide thickness 90 nm) for 30 minutes in a porphyrin

nanoring solution with a concentration of 100 µg/ml in a methanol/toluene mixture (1:3 by volume). Before deposition the silicon samples were cleaned in IPA in an ultrasonic bath for 5 minutes and subsequently blow-dried with nitrogen. Silicon is chosen as a substrate for Raman spectroscopy because it has a very well defined spectrum and exhibits zero background outside its well defined narrow peaks at 520 cm^{-1} and 960 cm^{-1}, thus making it an ideal substrate for resolving weak Raman shifts outside these regions.

After preparing samples Raman spectra were obtained. Figure 6-14 shows spectra of c-P12 and c-P24 porphyrin nanorings on SiO_2/Si and a silicon control spectrum.

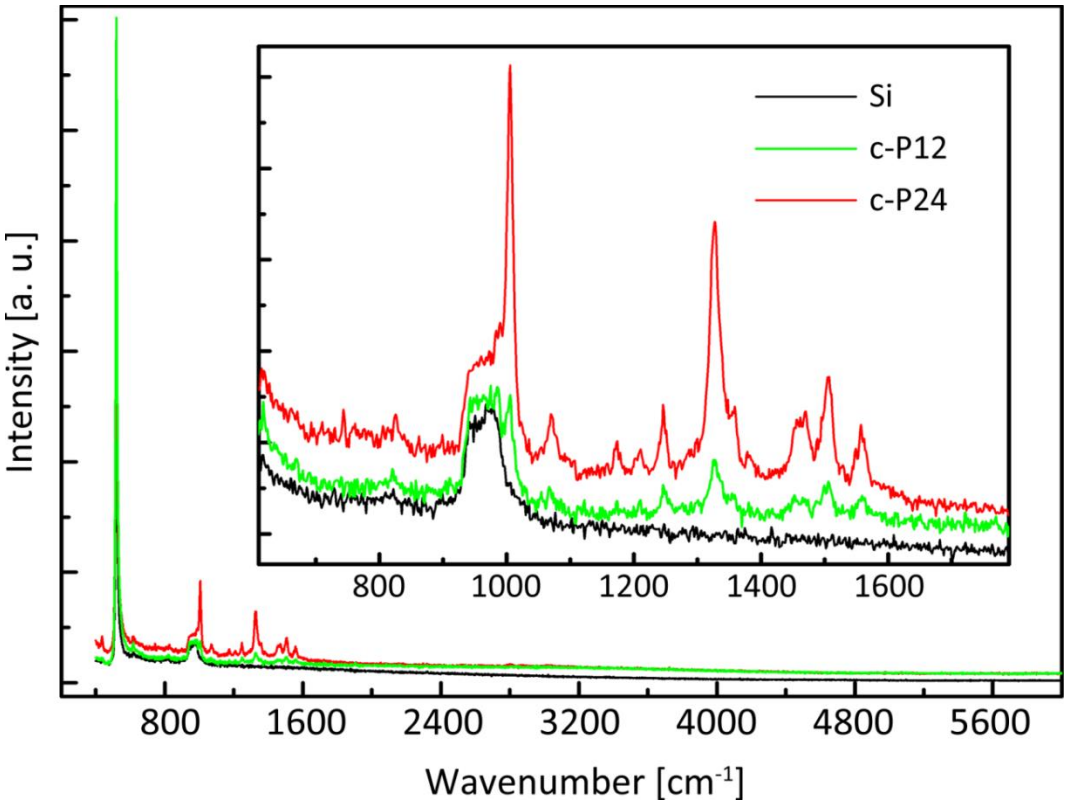

Figure 6-14: Raman spectra of a thin film of c-P12 and c-P24 porphyrin nanorings on a Si/SiO_2 substrate and control spectrum of a clean Si/SiO_2 sample; the characteristic peaks in the region between 1000 and 1600 cm^{-1} are more prominent in the c-P24 sample.

The Raman spectra of c-P24 and c-P12 exhibit a range of peaks between 1000 cm^{-1} and 1600 cm^{-1}. These are attributed to the various bending and stretching modes of the butadiyene linker group. Roman [124] showed that the Raman shift of the peaks can vary significantly with the substituents around the diacetylene group (R-C≡C-C≡C-R). This makes assignments of the peaks to its contributing Raman modes without extensive computational effort difficult. However, matching the spectra of c-P12 and c-P24 to Raman studies of molecules containing diacetylene groups the peak at ~1000 cm^{-1} is attributed to torsion of the C≡C bond, and the peak at ~1330 cm^{-1} is linked to stretching of the ≡C-C≡ group.

6.6. Conclusions

The porphyrin nanorings c-P24 and c-P12, nanorings with 24 or 12 porphyrin subunits respectively are deposited onto a surface in UHV using electrospray deposition and imaged with STM. The molecule c-P24 can aggregate in solution into columnar stacks, which influences the mechanical stiffness of the macromolecule. The stacking effect is preserved during electrospray deposition, and those stacked nanorings can trap adsorbed material such as fullerenes. The trapping probability is influenced both by the height of the (stacked) nanorings and the perimeter length. Porphyrin oligomers and fullerenes are both organic semiconductors, and the formation of controlled structures, with the option of transfer to any other substrate, opens the possibility to study the influence of supramolecular order on optoelectronic properties such as exciton transfer, luminescence, or photovoltaic effects.

Chapter 7

Raman and STM studies of acetylenic (Glaser-Hay) coupling of porphyrins

7.1. Introduction

Mimicking their natural counterparts, synthetically formed conjugated porphyrin polymers are studied extensively for their potential applications in optoelectronics, light harvesting, and nanoscale charge transport. One possible route to polymerised molecules, covalent linking of acetylenes via the oxidative coupling reaction in solution in the presence of a copper catalyst has been explored and refined by synthetic chemists since the 1970s. Today, acetylenic coupling is widely used as a flexible approach to the controlled design of various macromolecules. A prominent example is the synthesis of various linear and cyclic porphyrin oligomers described in detail in section 2.2.

Additionally to wet chemistry synthesis, the Glaser-Hay coupling reaction is very promising for the controlled fabrication of novel two-dimensional materials on surfaces. The on-surface synthesis of functional, thermally and chemically stable tailored two-dimensional nanostructures and networks is of great interest in the field of optoelectronics. This has motivated the study of different on-surface covalent coupling reactions under ultrahigh vacuum conditions on metal surfaces, as explored comprehensively in section 2.1. However, many of the established and well explored methods require considerable activation barriers and/or comprise potentially unwanted contaminants. To date, the most frequently applied 2D reaction is the Ullmann coupling of aryl halides at various metal surfaces, some of which are discussed in Chapters 2 and 4. Prospective drawbacks of these surface catalysed Ullmann reactions are the relatively high activation barriers and the generation of free halogens after dissociation. Often the covalent coupling reaction results in potentially unwanted co-adsorbed halogens coexisting with the target structures.

Coupling processes with mild reaction conditions that preserve fragile molecules and, at the same time, do not produce contaminations are needed. Acetylenic coupling, where the only by-product is volatile H_2, has been

successfully applied to the formation of functional nano-architectures, as has been described in section 2.1.4. Comparing reaction parameters of similar molecules described in the literature, it becomes apparent that Glaser-Hay coupling reactions also seem to have significantly lower activation barriers than Ullmann coupling reactions. Ullmann-type coupling reactions of various phenyl halides on silver substrates are depicted in Figure 7-1a (see section 2.1.1 for details). The coupling of ethynyl benzenes on a silver substrate, as shown in Figure 7-1b, was reported recently by Barth and co-workers (see section 2.1.4 for details).

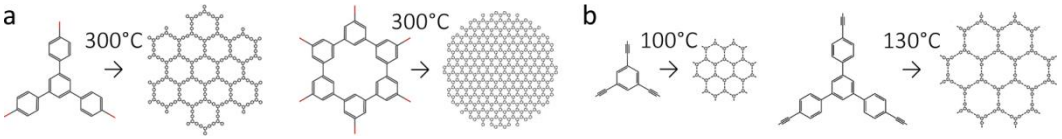

Figure 7-1a: Formation of polyphenylene networks via Ullmann coupling from TBPB and HCP, the reaction temperature on a silver substrate has been reported to be 300°C [7, 18]; b: Formation of polyphenylene networks via Glaser-Hay coupling from TEB and ext-TEB, the reaction temperature on a silver substrate has been reported to be 100°C to 130° [26].

Dissociation of the halogen-aryl bond on a silver substrate occurs in all reported studies at or below room temperature. The covalent coupling reaction however requires thermal activation at about 300°C [7, 18]. Covalent bonds via Glaser-Hay coupling of ethynyl benzenes on a silver substrate on the other hand start to form at 30°C to 60°C, with the formation of extended networks occurring at 100°C to 250°C [26].

The experiments described in this chapter explore, using Raman and STM measurements, surface mediated Glaser-Hay coupling of ethynyl porphyrins. The alkyne homocoupling takes place on the Au(111) noble metal surface as well as on a SiO_2/Si substrate in vacuum with volatile H_2 as the only by-product. The fragile porphyrin compounds used for the experiments are deposited from

solution or via electrospray. Attempts to evaporate the molecules from a K-cell resulted in decomposition of the molecules before they reached their sublimation temperature.

7.2. Raman studies of one-dimensional polymerisation of solution deposited di-ethynyl porphyrin monomers

Porphyrin monomers were deposited from solution in ambient conditions and subsequently annealed in high vacuum to form covalent bonds via Glaser-Hay coupling. The porphyrin molecule investigated first is di-ethynyl-di-aryl-porphyrin (DEDAP), as shown in Figure 7-2.

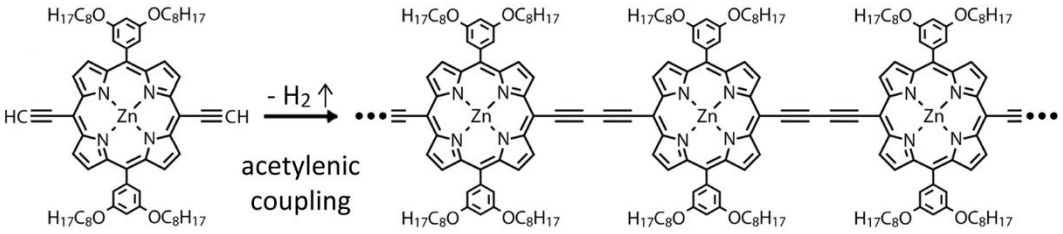

Figure 7-2: Structure of a di-ethynyl-di-aryl porphyrin (DEDAP) molecule and the acetylenic coupling reaction forming a porphyrin polymer.

One DEDAP molecule has the same structure as one porphyrin subunit of the porphyrin oligomers described in sections 2.2.2 and 6. A zinc metalated porphyrin centre is *meso* substituted with two long aryl chains and two ethynyl groups in *trans* configuration. The ethynyl groups may form covalent links via the Glaser-Hay coupling reaction, as depicted in Figure 7-2, upon thermal activation. Traditionally such acetylene linked porphyrin oligomers are synthesised using wet chemistry templating techniques described in section 2.2.2. Linear and cyclic oligomers with high purity and yield can be synthesised, however their shape is confined by the templates available. The experiments described in this chapter explore the prospect of on-surface acetylenic polymerisation of the same porphyrin monomers resulting in one dimensional oligomers of variable size.

The DEDAP monomers were dissolved in in a methanol/toluene mixture (1:3 by volume) and diluted to a concentration of 100 µg/ml. Si(100), terminated with a 90 nm oxide layer was chosen as substrate. Prior to deposition the silicon was cleaned in IPA in an ultrasonic bath for 5 minutes and blow-dried with nitrogen. The clean silicon samples were immersed for 30 minutes in the prepared solution. After 30 minutes the samples were blow-dried with nitrogen and Raman and fluorescence spectra were taken. Fluorescence spectroscopy shows that the porphyrin monomers exhibit the characteristic porphyrin fluorescence double peak in the 600 to 800 nm region of the spectrum, as described in section 2.2.3. Despite the low density of porphyrin macrocycles on the surface may be clearly resolved in Figure 7-3.

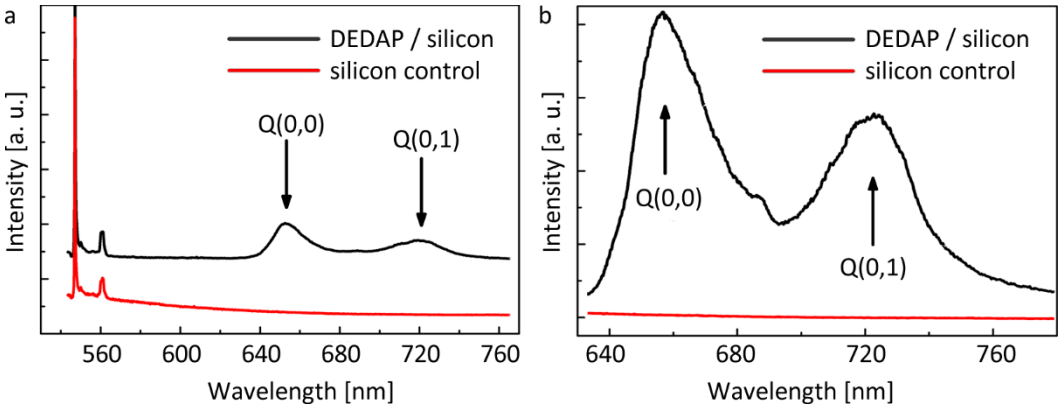

Figure 7-3: Fluorescence spectra (excitation wavelength = 532nm) of solution deposited di-ethylene-di-aryl-porphyrin (DEDAP) on a SiO_2/Si substrate and control spectra of SiO_2/Si; the characteristic double-peak at 655 ± 1 nm (Q(0,0)) and 720 ± 1 nm (Q(0,1)) [53, 54].

The monomer samples were inserted into a high vacuum chamber (base pressure 10^{-8} mbar), where they were annealed at 50°C for 2 h. Upon removing the samples from the high vacuum chamber Raman spectra were taken again. This cycle of heating in HV and Raman spectroscopy was repeated for annealing cycles at 100°C, 200°C, and 300°C for 2 h each. Raman spectra taken after annealing at 50°C and 100°C do not differ from the spectrum of the monomers

taken after deposition at room temperature. The presence of the monomers on the surface was verified via fluorescence spectroscopy to ensure the molecules did not desorb during annealing. However, the spectrum of the sample taken after annealing at 200°C differs significantly. Figure 7-4 shows Raman spectra of the DEDAP molecules before and after annealing and of linear l-P10 oligomers on silicon.

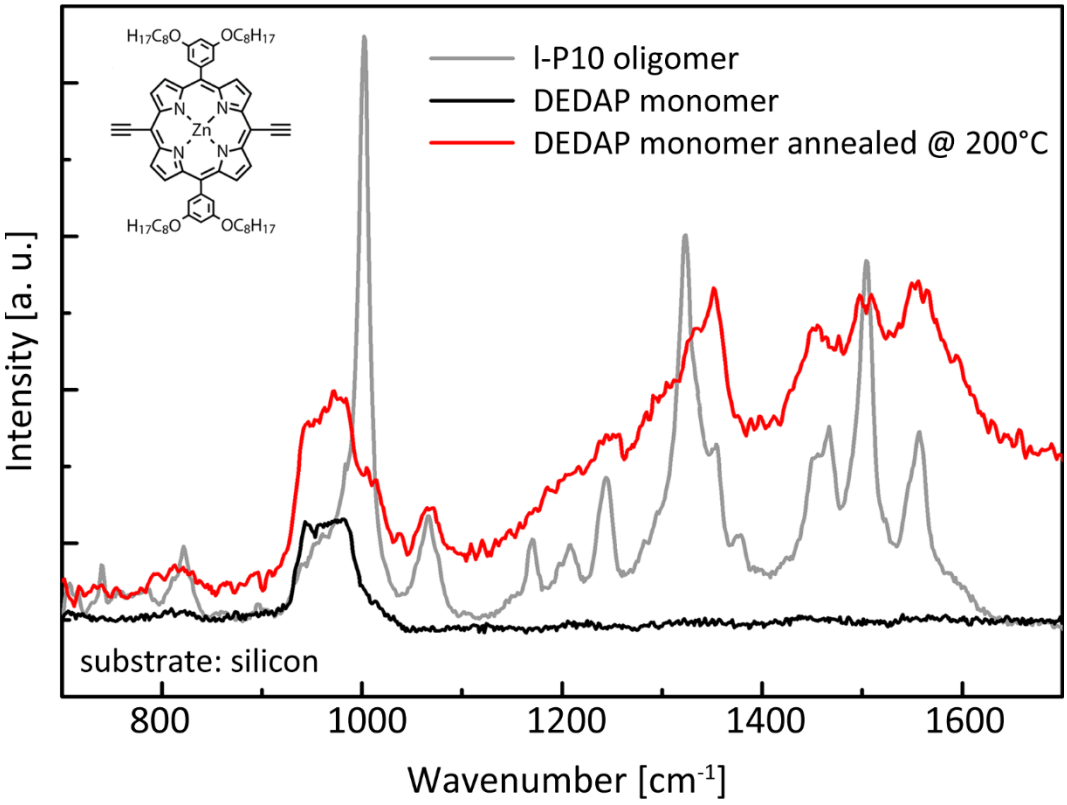

Figure 7-4: Raman spectra of l-P10 (grey) and DEDAP before (black) and after (red) annealing on silicon; the broad peak at 930-990 cm^{-1} corresponds to the silicon substrate, the remaining features are attributed to the ethylene-linked porphyrins; inset: structure of DEDAP.

While the monomers do not exhibit features prior to annealing (the peak at 930-990 cm^{-1} is from the silicon substrate), the monomers after annealing show a set of distinctive peaks on a high background. When comparing the relative

intensity and position of those peaks to the l-P10 spectrum it is apparent that the main features are similar in both samples.

Parallel to deposition and annealing of the monomers control samples of various linear and circular porphyrin oligomers (Figure 7-5a) were produced using the same deposition method and parameters. Those give typical spectra of acetylene-linked porphyrins of specific dimensions. Subsequently Raman spectra were obtained for these samples, some of which are shown in Figure 7-5b. The porphyrin oligomers exhibit distinct spectra. Spectra of similar butadiene-linked porphyrins in literature exhibit a similar set of Raman shifts in the region between 1300 and 1600 cm^{-1} [67, 68].

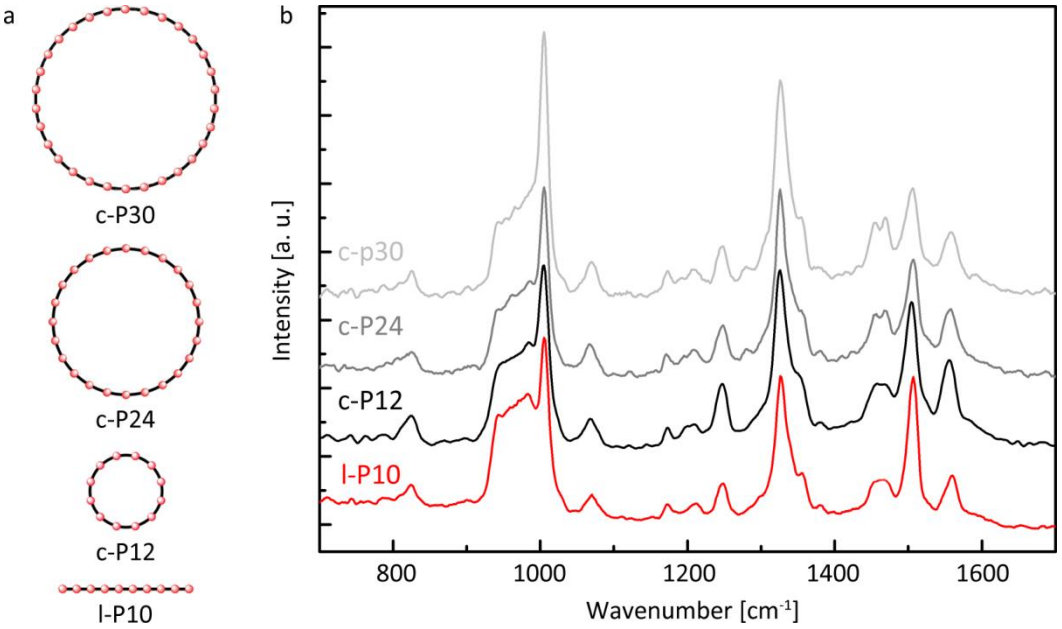

Figure 7-5a: Schematic structures of the different porphyrin oligomers investigated; b: Normalised Raman spectra of solution deposited porphyrin oligomers.

The Raman spectra of the different porphyrin oligomers all exhibit the same general shape and location of the peaks in the Raman spectrum. However, the relative intensities change depending on the size of the oligomer. There is no significant difference between the linear and cyclic porphyrins, suggesting that

the bending of the butadiene link has little effect on the vibrational Raman modes of the high intensity shifts. Raman spectra are taken with a green laser (532 nm) at relatively low laser power (1% to 10% of 40 mW). Long or intense irradiation results in significant decrease of the observed features upon taking the spectrum on the same position anew.

The same set of experiments was conducted on flame-annealed Au(111) on mica surfaces with a similar outcome, as shown in Figure 7-6.

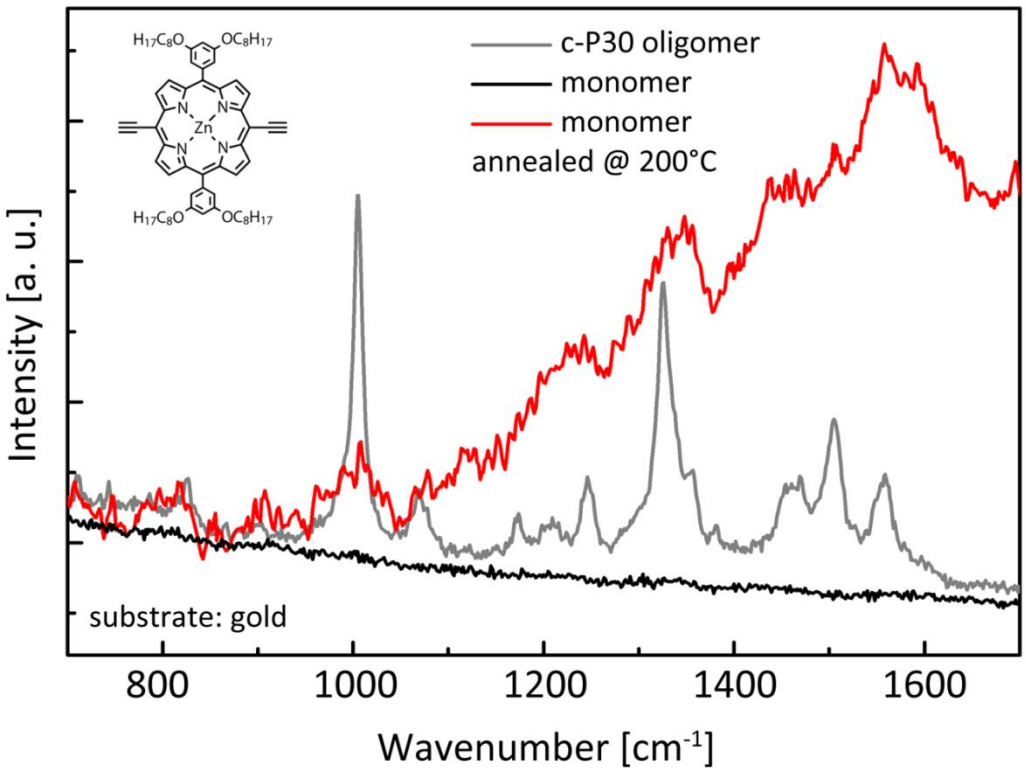

Figure 7-6: Raman spectra of c-P30 and DEDAP before and after annealing on gold; again the features are attributed to the ethylene-linked porphyrins; inset: structure of DEDAP.

The DEDAP molecules were deposited via immersion into a 100 ug/ml solution for 30 min and subsequently blow-dried with nitrogen. The samples were investigated with Raman and fluorescence spectroscopy. No Raman peaks can be observed on the sample prior to annealing, as for the

silicon samples. The presence of the molecules before polymerisation cannot be verified with fluorescence spectroscopy. To initiate covalent coupling the samples were annealed in HV (base pressure 10^{-6} to 10^{-5} mbar) at 200°C for 2 h and investigated subsequently with Raman spectroscopy.

Spectra on a gold substrate show similar results to the spectra on a silicon substrate, although the background of the annealed DEDAP is more predominant. The position of the features at 1450-1600 cm^{-1} seems to be red-shifted compared to a c-P30 nanoring control sample. This shift is not observed on silicon substrates, interaction between the gold substrate and the molecules might influence the vibrational modes and thus the Raman shifts.

7.3. STM and Raman studies of two-dimensional polymerisation of electrospray deposited tetra-ethynyl porphyrin monomers

Covalent two dimensional networks formed via Glaser-Hay coupling of tetra-ethynyl-porphyrin (TEP, as shown in Figure 7-7) were investigated using STM following deposition of the porphyrin monomers on an Au(111) surface using electrospray and subsequent annealing of the sample.

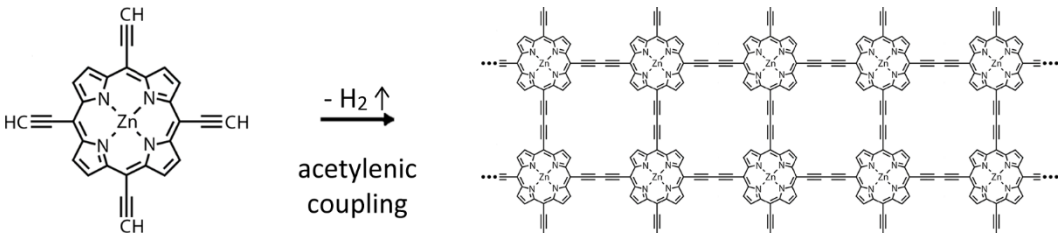

Figure 7-7: Structure of a tetra ethynyl porphyrin (TEP) molecule and the acetylenic coupling reaction forming an ideal two dimensional porphyrin polymer.

The molecules investigated in this chapter have the same core structure as the phenyl porphyrin monomers described in the previous experiments,

however the aryl side chains are substituted by ethynyl groups as. Therefore this molecule is considerably smaller and lighter than DEDAP due to the loss of the long side chains.

This enables the molecules, in principle, to form two-dimensional extended networks via acetylenic Glaser-Hay coupling rather than linear or cyclic polymers. The centre-to-centre distance of the porphyrin molecules in the network is expected to be 1.33 nm, the same as the separation between two neighbouring porphyrin units in analogue linear porphyrin oligomers formed by Anderson and co-workers via solution based synthesis [84].

Attempts to deposit the molecules in UHV from a K-cell failed, the molecules disintegrated before sublimation. Therefore electrospray deposition (as described in section 3.1) was chosen for deposition. The solution concentration used in the experiments was 100 µg/mL porphyrin monomers in a methanol/toluene mixture (1:3 by volume). The molecules were deposited at a flow rate of ~10 µL / min through a stainless steel emitter held at ~1.8 kV under atmospheric conditions onto gold for 10 minutes. During the deposition the pressure in the deposition chamber rose from a base pressure of 10^{-10} mbar to the high 10^{-6} mbar range. The Au(111) on mica sample was cleaned before the deposition by repeated cycles of Ar ion sputtering (1×10^{-5} mbar, 0.8 keV, ~2 µA) and subsequent annealing (~500°C), until a clear herringbone reconstruction was observed.

Figure 7-8 shows STM images following the deposition of TEP via ESD and subsequent annealing of the sample at about 150°C for 2 h. The molecules form disordered open networks that exhibit a weak correlation to the herringbone orientation.

The centre-to-centre distance between adjacent molecules is found to be 1.3 ± 0.1 nm, which is in good agreement with the expected value of 1.33 nm,

consistent with covalently linked porphyrin molecules [84]. Due to the nature of electrospray deposition, the coverage of the network depends on the position on the sample relative to the centre point, where the electrospray beam impinges on the surface.

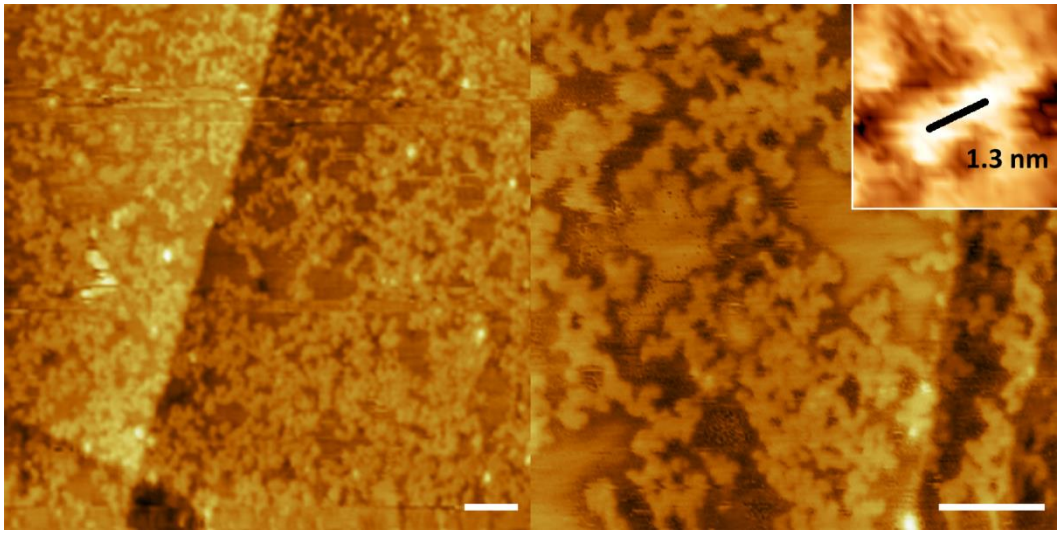

Figure 7-8: STM images (-1.7 V, 0.03 nA) of tetra-ethynyl-porphyrin (TEP) on Au(111) deposited via electrospray deposition and subsequent annealing at 150°C; scale bar 10 nm; inset: zoom of a dimer with centre-to-centre distance indicated.

The STM images in Figure 7-9 were taken at three different locations on the same sample each 200 nm apart moving towards the centre.

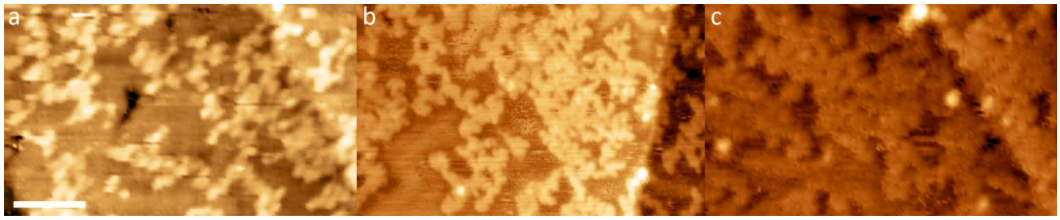

Figure 7-9: STM images (-1.7 V, 0.03 nA) of TEP networks across the sample; the scanned areas are approximately 200 nm apart; scale bar 10 nm.

The gradient in coverage originating in the nature of the electrospray deposition technique allows for investigation of the network formed at the same parameters with different molecule density on the surface. At low coverages small clusters and short chains of 4 to 8 porphyrin monomers dominate the surface, as seen in Figure 7-9a. A higher density of molecules results in the formation of islands with diameters of up to 20 nm that are interconnected irregularly by chains, as shown in the STM image in Figure 7-9b. Upon scanning closer to the centre of the incident electrospray beam, the average island size becomes bigger and the patches are closer together and better interconnected.

Analogous to the experiments described in section 7.2, solution deposited sampled of TEP were produced on silicon and gold substrates and subsequently annealed to initiate Glaser-Hay coupling. The porphyrin monomers were dissolved in in a methanol/toluene mixture (1:3 by volume) and diluted to a concentration of 100 μg/ml. The substrates were cleaned immediately before deposition by treating the Si sample immersed in IPA in an ultrasonic bath for 5 minutes, and flame annealing the gold on mica surface. The clean samples were subsequently immersed for 30 minutes in the prepared solution. After 30 minutes the samples were blow-dried with nitrogen and Raman and fluorescence spectra were taken. Fluorescence spectroscopy on the silicon sample verifies the presence of the porphyrin monomers on the surface. The characteristic porphyrin fluorescence double peak in the 600 to 800 nm region of the spectrum is observed.

The TEP monomer samples were inserted into a high vacuum chamber (base pressure 10^{-8} mbar), where they are annealed at 50°C for 2 h. After the samples have cooled down to room temperature, they were removed from the high vacuum chamber and Raman spectra were obtained. The samples were subsequently annealed at higher temperatures of 100°C, 150°C, and 200°C for 2 h each. After each heating step, the samples were taken to the Raman system for spectroscopy.

Unlike the larger DEDAP molecule discussed in the previous section, the TEP molecules do not undergo Glaser-Hay coupling on the silicon surface. After each annealing step the sample was characterised. No changes were observed in the Raman spectrum. Fluorescence spectroscopy suggests that the samples desorb in between 100°C and 150°C. After annealing the sample up to 100°C the characteristic double peak is present in the fluorescence spectrum, after annealing the sample at 150°C however the porphyrin fluorescence signal is no longer present, and thus probably the molecules have desorbed or decomposed.

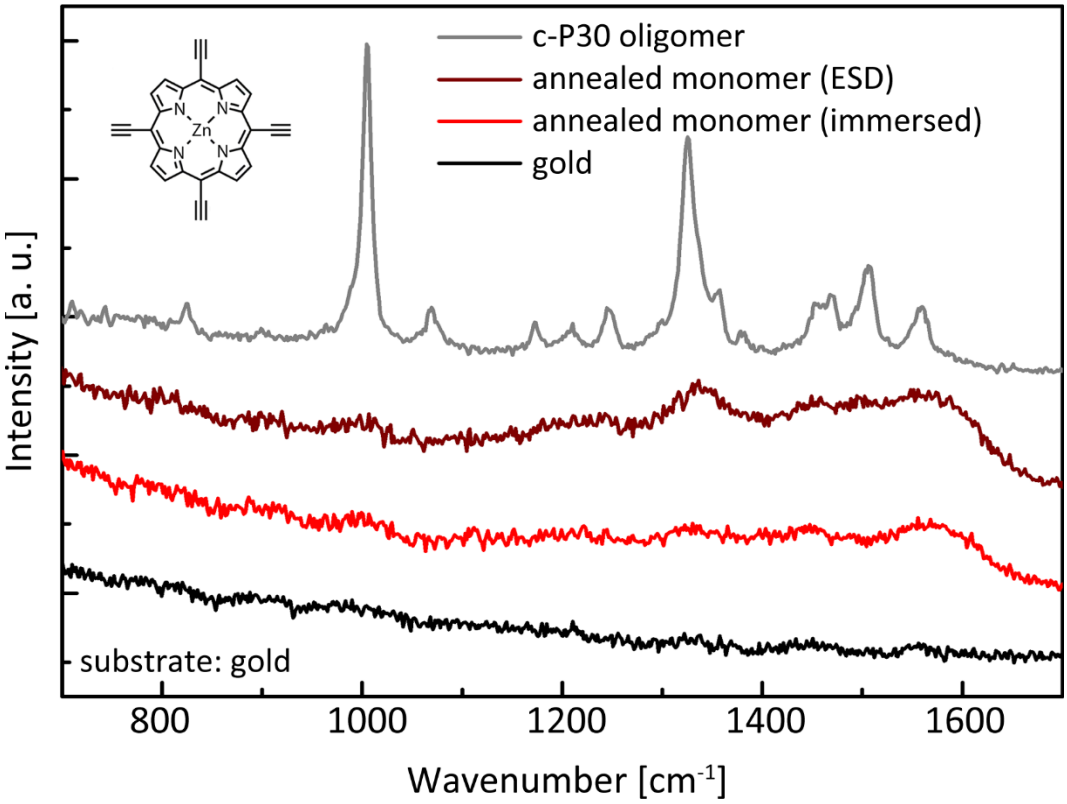

Figure 7-10: Raman spectra of c-P30 and TEP before and after annealing on gold; the features attributed to the butadiene-linked porphyrins are very distinctive in the c-P30 spectrum and much weaker in the spectra of thermally activated monomers; inset: structure of TEP.

On the gold substrate however Glaser-Hay coupling of the TEP monomers is possible, as has been demonstrated with STM earlier. Raman spectra of TEP on

gold taken after annealing at 50°C and 100°C do not differ from the spectrum of the monomers taken after deposition at room temperature.

After annealing the sample at 150°C, a change in the Raman spectrum was observed. Figure 7-10 shows Raman spectra of the solution deposited TEP molecules before and after annealing at 150°C and of solution deposited c-P30 porphyrin nanorings on a gold substrate.

The sample with the TEP molecule deposited via ESD and annealed in UHV, which was investigated earlier with STM, was taken out of the UHV camber and Raman spectra were taken for comparison with the solution deposited samples.

The Raman spectra of the annealed TEP monomers exhibit broad Raman shifts of relatively low intensity at the expected wavenumbers which are not present for clean gold samples or samples with the monomers prior to annealing.

7.4. Conclusions and outlook

The acetylenic coupling reaction of porphyrin monomers that is used by synthetic chemists in the formation of linear and cyclic porphyrin oligomers can be realised on surfaces. The distinct Raman fingerprint of butadiene-linked porphyrins serves as a tool to verify the success of on-surface Glaser-Hay coupling. Depending on the nature of the substituents at the meso positions of the porphyrin macrocycle, one dimensional chains or two dimensional networks are formed. Di-ethynyl-di-aryl-porphyrins (DEDAP) form covalent links on silicon and gold substrates, resulting in linear oligomers of unknown length. The lighter tetra-ethynyl-porphyrin (TEP) appears to have a narrower temperature window, where Glaser-Hay coupling is induced and the molecules don't desorb. On a silicon substrate the desorption temperature is lower than the temperature required for acetylenic coupling.

Future work might address the question of whether DEDAP forms covalent links on a gold substrate at lower temperatures than 200°C due to the supposed catalytic properties of gold. Complementary studies on copper and silver substrates might help to gain insight into the coupling, diffusion, and desorption properties of porphyrin monomers. A more detailed Raman study on porphyrin oligomers of different lengths might allow deductions as to the length of the oligomers formed on-surface by thermal activation of the DEDAP monomers.

Chapter 8

Summary and outlook

This thesis focuses on different aspects of nano architecture, the formation of well-defined and characterised systems at a molecular scale. The thesis provides novel ways to control and manipulate the formation of molecular structures that have the prospect of being implemented into a wide variety of future research.

First, the formation of extended two dimensional polymer networks is explored. Hydrogen bonded systems with long-range order on one hand and the mechanics of covalent coupling of individual molecules on the other have been extensively studied in the past. Thus, a strong motivation was to combine both aspects and form extended, stable structures. Especially in the light of possible applications of organic monolayers in optoelectronic devices, strong intermolecular coupling is a highly desired material property for two dimensional molecular networks.

Whereas covalently coupled long range ordered molecular crystalline structures with negligible defect density were not realised, polymer networks stretched over several microns could be formed reliably. Extended covalent hexagonal networks with benzene based molecules as building blocks may serve as graphene analogues. Unlike graphene, the pore size of these structures can be tailored by altering the chemistry of the building blocks. Deposition parameters such as deposition rate and substrate temperature influence whether the final structures tend to be more microcrystalline or a glassy.

Porphyrin, sometimes called the pigment of life for its ubiquity in nature, was another molecule successfully assembled into polymer networks. The networks formed were extended, highly interconnected, disordered networks with local patches displaying the porphyrin's square symmetry.

Next, a process for the transfer of such molecular layers was developed. Most bottom-up approaches for the formation of covalently coupled structures require a metal catalyst as substrate. This may be a significant limitation to

certain applications. Recently, several methods have been described for the transfer of graphene sheets. However, those were not applicable to a big variety of molecular thin films due to the use of aggressive solvents. Unexpected adhesive properties of C_{60} were used to transfer metallic, molecular and polymer thin films from a gold surface to dielectric substrates.

This transfer method has great potential in the characterisation of molecular and polymer thin films in the absence of metal. Another possible application is in the fabrication of sophisticated nanoscale devices.

Porphyrin monomers can not only be used to form extended polymer networks, but also well-defined macromolecules. Stacked porphyrin nanorings with 24 porphyrin subunits show interesting interactions with C_{60} when deposited onto the same gold substrate. The C_{60} molecules become trapped inside the nanorings. This is another route to control the architecture on a molecular level. Porphyrin nanorings are crucial subunits of the light harvesting complexes LH1 and LH2, the functional units in photosynthesis. The combination of porphyrin with C_{60} in electron donor/acceptor systems has been investigated in the past. Thus, controlled formation of porphyrin nanorings with trapped C_{60} molecules might be of use for research synthetic biomimetic light-harvesting structures.

Most on-surface formations of covalent bonds to date are based on the Ullman reaction, a coupling reaction between aryl halides in the presence of a metal catalyst. The final experimental chapter explores a different approach to on-surface coupling. Porphryin molecules with acetylene linkers were successfully polymerised via Glaser-Hay coupling. This coupling reaction also works on non-metallic substrates. It is also a good alternative to Ullman-type coupling when the release of halogens must be avoided.

Chapter 9

Bibliography

[1] A. Gourdon, On-surface covalent coupling in ultrahigh vacuum, *Angew. Chem. Int. Ed. Engl.*, 47, 37, 6950–3, 2008.

[2] L. Bartels, Tailoring molecular layers at metal surfaces., *Nat. Chem.*, 2, 2, 87–95, 2010.

[3] M. O. Blunt, J. C. Russell, N. R. Champness, and H. Beton, Templating molecular adsorption using a covalent organic framework., *Chem. Commun.*, 46, 38, 7157–7159, 2010.

[4] M. Lackinger and W. M. Heckl, Carboxylic acids: Versatile building blocks and mediators for two-dimensional supramolecular self-assembly, *Langmuir*, 25, 19, 11307–11321, 2009.

[5] M. Matena, T. Riehm, M. Stöhr, T. A. Jung, and L. H. Gade, Transforming surface coordination polymers into covalent surface polymers: linked polycondensed aromatics through oligomerization of N-heterocyclic carbene intermediates., *Angew. Chem. Int. Ed. Engl.*, 47, 13, 2414–7, 2008.

[6] U. Schlickum, R. Decker, F. Klappenberger, G. Zoppellaro, S. Klyatskaya, M. Ruben, I. Silanes, A. Arnau, K. Kern, H. Brune, and J. V. Barth, Metal-organic honeycomb nanomeshes with tuneable cavity size., *Nano Lett.*, 7, 12, 3813–7, 2007.

[7] R. Gutzler, H. Walch, G. Eder, S. Kloft, W. M. Heckl, and M. Lackinger, Surface mediated synthesis of 2D covalent organic frameworks: 1,3,5-tris(4-bromophenyl)benzene on graphite(001), Cu(111), and Ag(110)., *Chem. Commun.*, 29, 4456–8, 2009.

[8] I. Langmuir, The Arrangement of Electrons in Atoms and Molecules., *J. Am. Chem. Soc.*, 41, 6, 868–934, 1919.

[9] G. Brunetto, A. S. Autreto, L. D. Machado, B. I. Santos, R. B. dos Santos, and D. S. Galvão, Nonzero Gap Two-Dimensional Carbon Allotrope from Porous Graphene, *J. Phys. Chem. C*, 116, 23, 12810–12813, 2012.

[10] J. L. Mendoza-Cortés, S. S. Han, H. Furukawa, O. M. Yaghi, and W. A. Goddard, Adsorption mechanism and uptake of methane in covalent

organic frameworks: theory and experiment., *J. Phys. Chem. A*, 114, 40, 10824–33, 2010.

[11] J. L. Mendoza-Cortés, S. S. Han, and W. A. Goddard, High H2 uptake in Li-, Na-, K-metalated covalent organic frameworks and metal organic frameworks at 298 K., *J. Phys. Chem. A*, 116, 6, 1621–31, 2012.

[12] D. C. Sherrington, Polymers as Catalysts, *Br. Polym. J.*, 12, 2, 70–74, 2007.

[13] F. Ullmann and J. Bielecki, Über Synthesen in der Biphenylreihe, *Berichte der Dtsch. Chem. Gesellschaft*, 34, 2, 2174–2185, May 1901.

[14] S. Hla, L. Bartels, G. Meyer, and K. Rieder, Inducing all steps of a chemical reaction with the scanning tunnelling microscope tip: towards single molecule engineering, *Phys. Rev. Lett.*, 85, 13, 2777–80, 2000.

[15] S.-W. Hla, G. Meyer, and K.-H. Rieder, Selective bond breaking of single iodobenzene molecules with a scanning tunnelling microscope tip, *Chem. Phys. Lett.*, 370, 3–4, 431–436, 2003.

[16] L. Grill, M. Dyer, L. Lafferentz, M. Persson, M. V Peters, and S. Hecht, Nano-architectures by covalent assembly of molecular building blocks., *Nat. Nanotechnol.*, 2, 11, 687–91, 2007.

[17] L. Lafferentz, V. Eberhardt, C. Dri, C. Africh, G. Comelli, F. Esch, S. Hecht, and L. Grill, Controlling on-surface polymerization by hierarchical and substrate-directed growth., *Nat. Chem.*, 4, 3, 215–20, 2012.

[18] M. Bieri, M.-T. Nguyen, O. Gröning, J. Cai, M. Treier, K. Aït-Mansour, Ruffieux, C. a Pignedoli, D. Passerone, M. Kastler, K. Müllen, and R. Fasel, Two-dimensional polymer formation on surfaces: insight into the roles of precursor mobility and reactivity., *J. Am. Chem. Soc.*, 132, 46, 16669–76, 2010.

[19] J. Cai, Ruffieux, R. Jaafar, M. Bieri, T. Braun, S. Blankenburg, M. Muoth, A. Seitsonen, M. Saleh, X. Feng, K. Müllen, and R. Fasel, Atomically precise bottom-up fabrication of graphene nanoribbons., *Nature*, 466, 7305, 470–3, 2010.

[20] N. Zwaneveld, R. Pawlak, M. Abel, D. Catalin, D. Gigmes, D. Bertin, and L. Porte, Organized formation of 2D extended covalent organic frameworks at surfaces., *J. Am. Chem. Soc.*, 130, 21, 6678–9, May 2008.

[21] S. Weigelt, C. Busse, C. Bombis, M. M. Knudsen, K. V Gothelf, T. Strunskus, C. Wöll, M. Dahlbom, B. Hammer, E. Laegsgaard, F. Besenbacher, and T. R. Linderoth, Covalent interlinking of an aldehyde and an amine on a Au(111) surface in ultrahigh vacuum, *Angew. Chem. Int. Ed. Engl.*, 46, 48, 9227–30, 2007.

[22] M. Treier, N. V Richardson, and R. Fasel, Fabrication of surface-supported low-dimensional polyimide networks, *J. Am. Chem. Soc.*, 130, 43, 14054–5, 2008.

[23] C. Glaser, Beiträge zur Kenntniss des Acetenylbenzols, *Berichte der Dtsch. Chem. Gesellschaft*, 2, 1, 422–424, 1869.

[24] A. S. Hay, Oxidative Coupling of Acetylenes. II 1, *J. Org. Chem.*, 27, 9, 3320–3321, 1962.

[25] F. Diederich, Carbon scaffolding: building acetylenic all-carbon and carbon-rich compounds, *Nature*, 369, 6477, 199–207, May 1994.

[26] Y.-Q. Zhang, N. Kepčija, M. Kleinschrodt, K. Diller, S. Fischer, A. C. Papageorgiou, F. Allegretti, J. Björk, S. Klyatskaya, F. Klappenberger, M. Ruben, and J. V Barth, Homo-coupling of terminal alkynes on a noble metal surface., *Nat. Commun.*, 3, 1286, 2012.

[27] H.-Y. Gao, H. Wagner, D. Zhong, J.-H. Franke, A. Studer, and H. Fuchs, Glaser coupling at metal surfaces., *Angew. Chem. Int. Ed. Engl.*, 52, 14, 4024–8, 2013.

[28] H.-W. Wanzlick, Nucleophile Carben-Chemie, *Angew. Chemie*, 74, 4, 129–134, 1962.

[29] L. R. Milgrom, G. Yahioglu, D. W. Bruce, S. Morrone, F. Z. Henari, and W. J. Blau, Mesogenic Zinc(u) complexes of 5,10,15,20- tetraarylethynyl-substituted porphyrins, *Adv. Mater.*, 9, 4, 313–316, 1997.

[30] P. Rothemund, Formation of Porphyrins from Pyrrole and Aldehydes, *J. Am. Chem. Soc.*, 57, 10, 2010–2011, 1935.

[31] E. Hückel, Grundzüge der Theorie ungesättigter und aromatischer Verbindungen, *Zeitschrift für Elektrochemie und Angew. Phys. Chemie*, 43, 9, 752–788, 1937.

[32] A. D. Adler, F. R. Longo, J. D. Finarelli, J. Goldmacher, J. Assour, and L. Korsakoff, A simplified synthesis for meso-tetraphenylporphine, *J. Org. Chem.*, 32, 2, 476–476, 1967.

[33] J. S. Lindsey, I. C. Schreiman, H. C. Hsu, C. Kearney, and A. M. Marguerettaz, Rothemund and Adler-Longo reactions revisited: synthesis of tetraphenylporphyrins under equilibrium conditions, *J. Org. Chem.*, 52, 5, 827–836, 1987.

[34] G. Badger, R. Jones, and R. Laslett, Porphyrins. VII. The synthesis of porphyrins by the Rothemund reaction, *Aust. J. Chem.*, 17, 9, 1028, 1964.

[35] T. Tanaka and A. Osuka, Conjugated porphyrin arrays: synthesis, properties and applications for functional materials., *Chem. Soc. Rev.*, 44, 943-969, 2014.

[36] H. L. Anderson and J. K. M. Sanders, Synthesis of a cyclic porphyrin trimer with a semi-rigid cavity, *J. Chem. Soc. Chem. Commun.*, 22, 1714, 1989.

[37] S. Anderson, H. L. Anderson, and J. K. M. Sanders, Expanding roles for templates in synthesis, *Acc. Chem. Res.*, 26, 9, 469–475, 1993.

[38] S. Anderson, H. L. Anderson, and J. K. M. Sanders, Template-directed synthesis of linear and cyclic butadiyne-linked porphyrin oligomers up to a linear octamer, *J. Chem. Soc. Perkin Trans. 1*, 2, 18, 2247, 1995.

[39] M. Hoffmann, J. Kärnbratt, M.-H. Chang, L. M. Herz, B. Albinsson, and H. L. Anderson, Enhanced π Conjugation around a Porphyrin[6] Nanoring, *Angew. Chemie*, 120, 27, 5071–5074, 2008.

[40] M. Hoffmann, C. J. Wilson, B. Odell, and H. L. Anderson, Template-directed synthesis of a pi-conjugated porphyrin nanoring., *Angew. Chem. Int. Ed. Engl.*, 46, 17, 3122–5, 2007.

[41] R. T. Kelly, R. L. Xie, C. Kraebel Weinreb, and T. Bregant, A molecular vernier, *Tetrahedron Lett.*, 39, 22, 3675–3678, May 1998.

[42] M. C. O'Sullivan, J. K. Sprafke, D. V Kondratuk, C. Rinfray, T. D. W. Claridge, A. Saywell, M. O. Blunt, J. N. O'Shea, H. Beton, M. Malfois, and H. L. Anderson, Vernier templating and synthesis of a 12-porphyrin nano-ring., *Nature*, 469, 7328, 72–5, 2011.

[43] D. V. Kondratuk, L. M. Perdigao, M. C. O'Sullivan, S. Svatek, G. Smith, J. N. O'Shea, H. Beton, and H. L. Anderson, Two Vernier-templated routes to a 24-porphyrin nanoring., *Angew. Chem. Int. Ed. Engl.*, 51, 27, 6696–9, 2012.

[44] H. L. Anderson, Building molecular wires from the colours of life: conjugated porphyrin oligomers, *Chem. Commun.*, 23, 2323–2330, 1999.

[45] K. Smith and J. Falk, *Porphyrins and metalloporphyrins*. 1975.

[46] C. Soret, Über ein Refractometer zur Messung der Brechungsexponentenund der Dispersion fester Körper, *Zeitschrift für Krist. - Cryst. Mater.*, 7, 1, 529–546, 1883.

[47] J. S. S. Baskin, H.-Z. H. Yu, and A. H. Zewail, Ultrafast dynamics of porphyrins in the condensed phase: I. Free base tetraphenylporphyrin, *J. Phys. Chem.,* 106, 42, 9837–9844, 2002.

[48] H. Fischer and D. Küst, Ueber das mikroskopische und optische Verhalten verschiedener Kohlenwasserstoffe, Harze und Kohlen, *Zeitschrift für Krist. - Cryst. Mater.*, 7, 1, 1883.

[49] R. S. Becker and J. B. Allison, Metalloporphyrins. Electronic Spectra and Nature of Perturbations. I. Transition Metal Ion Derivates 1a, *J. Phys. Chem.*, 67, 12, 2662–2669, 1963.

[50] L. R. Milgrom, *The Colours of Life: An Introduction to the Chemistry of Porphyrins and Related Compounds*. Oxford University Press, 1997.

[51] M. Gouterman, Spectra of porphyrins, *J. Mol. Spectrosc.*, 6, 138–163, 1961.

[52] A. H. Corwin, A. B. Chivvis, R. W. Poor, D. G. Whitten, and E. W. Baker, Porphyrin studies. XXXVII. The interpretation of porphyrin and metalloporphyrin spectra, *J. Am. Chem. Soc.*, 90, 24, 6577–6583, 1968.

[53] J. Karolczak, D. Kowalska, A. Lukaszewicz, A. Maciejewski, and R. Steer, Photophysical Studies of Porphyrins and Metalloporphyrins: Accurate Measurements of Fluorescence Spectra and Fluorescence Quantum Yields for Soret Band Excitation of Zinc Tetraphenylporphyrin, *J. Phys. Chem. A*, 108, 21, 4570–4575, May 2004.

[54] B. Białkowski, Y. Stepanenko, M. Nejbauer, C. Radzewicz, and J. Waluk, The dynamics and origin of the unrelaxed fluorescence of free-base tetraphenylporphyrin, *J. Photochem. Photobiol. A Chem.*, 234, 100–106, 2012.

[55] M. Uttamlal and S. Holmes-Smith, The excitation wavelength dependent fluorescence of porphyrins, *Chem. Phys. Lett.*, 454, 4–6, 223–228, 2008.

[56] H. N. Fonda, J. V. Gilbert, R. A. Cormier, J. R. Sprague, K. Kamioka, and J. S. Connolly, Spectroscopic, photophysical, and redox properties of some meso-substituted free-base porphyrins, *J. Phys. Chem.*, 97, 27, 7024–7033, 1993.

[57] B. Minaev and M. Lindgren, Vibration and Fluorescence Spectra of Porphyrin-Cored 2,2-Bis(methylol)-propionic Acid Dendrimers., *Sensors (Basel).*, 9, 3, 1937–66, 2009.

[58] G. Santosh and M. Ravikanth, Synthesis and spectral properties of N4, N3S, and N2S2 porphyrins containing one, two, three, and four meso-furyl groups, *Tetrahedron*, 63, 33, 7833–7844, 2007.

[59] J.-S. Hsiao, B. Krueger, R. W. Wagner, T. E. Johnson, J. K. Delaney, D. C. Mauzerall, G. R. Fleming, J. S. Lindsey, D. F. Bocian, and R. J. Donohoe, Soluble Synthetic Multiporphyrin Arrays. 2. Photodynamics of Energy-Transfer Processes, *J. Am. Chem. Soc.*, 118, 45, 11181–11193, 1996.

[60] D. Wróbel, I. Hanyż, R. Bartkowiak, and R. M. Ion, Fluorescence and Time-Resolved Delayed Luminescence of Porphyrins in Organic Solvents and Polymer Matrices, *J. Fluoresc.*, 8, 3, 191–198, 1998.

[61] S. E. J. Bell, A. H. R. Al-Obaidi, M. J. N. Hegarty, J. J. McGarvey, and R. E. Hester, Resonance Raman spectra of the triplet state of free-base tetraphenylporphyrin and six of its isotopomers, *J. Phys. Chem.*, 99, 12, 3959–3964, 1995.

[62] R. E. Oakes and S. E. J. Bell, DFT Studies of the Resonance Raman Spectra of Ground and Excited Triplet State Free Base meso - Tetraphenylporphyrin (H_2TPP), *J. Phys. Chem. A*, 107, 50, 10953–10959, 2003.

[63] M. Atamian, R. J. Donohoe, J. S. Lindsey, and D. F. Bocian, Resonance Raman spectra and normal-coordinate analysis of reduced porphyrins. 1. Zinc(II) tetraphenylporphyrin anion, *J. Phys. Chem.*, 93, 6, 2236–2243, 1989.

[64] J. H. Perng and D. F. Bocian, Resonance Raman spectra of free base and zinc(II) octaethylporphyrin anions, *J. Phys. Chem.*, 96, 12, 4804–4811, 1992.

[65] A. A. Bhuiyan, J. Seth, N. Yoshida, A. Osuka, and D. F. Bocian, Resonance Raman Characterization of Excitonically Coupled meso, meso-Linked Porphyrin Arrays, *J. Phys. Chem. B*, 104, 46, 10757–10764, 2000.

[66] D. H. Jeong, M.-C. Yoon, S. M. Jang, D. Kim, D. W. Cho, N. Yoshida, N. Aratani, and A. Osuka, Resonance Raman Spectroscopic Investigation of Directly Linked Zinc(II) Porphyrin Linear Arrays, *J. Phys. Chem. A*, 106, 10, 2359–2368, 2002.

[67] D. Beljonne, G. E. O'Keefe, J. Hamer, R. H. Friend, H. L. Anderson, and J. L. Brédas, Investigation of the linear and nonlinear optical response of edge-linked conjugated zinc porphyrin oligomers by optical spectroscopy and configuration interaction techniques, *J. Chem. Phys.*, 106, 23, 9439, 1997.

[68] D. Arnold, G. A. Heath, and D. A. James, Porphyrin Dimers Linked by Conjugated Butadiyne Bridges: Preparations, Spectra, Voltammetry and Reductive Spectroelectrochemistry of {[M(OEP)](μ-C 4)[M(OEP)]}(M 2 ≡H 4 , Co 2 , Ni 2 , Cu 2 , Zn 2 , Pd 2 , Pt 2 , Co/Ni, Ni/Cu, Ni/Zn), *J. Porphyrins Phthalocyanines*, 03, 01, 5–31, 1999.

[69] R. W. Wagner, J. Seth, S. I. Yang, D. Kim, D. F. Bocian, D. Holten, and J. S. Lindsey, Synthesis and Excited-State Photodynamics of a Molecular Square Containing Four Mutually Coplanar Porphyrins, *J. Org. Chem.*, 63, 15, 5042–5049, 1998.

[70] M. Hegner, Wagner, and G. Semenza, Ultralarge atomically flat template-stripped Au surfaces for scanning probe microscopy, *Surf. Sci.*, 291, 1–2, 39–46, 1993.

[71] Wagner, M. Hegner, H.-J. Guentherodt, and G. Semenza, Formation and in Situ Modification of Monolayers Chemisorbed on Ultraflat Template-Stripped Gold Surfaces, *Langmuir*, 11, 10, 3867–3875, 1995.

[72] J. Diebel, H. Löwe, Samorí, and J. Rabe, Fabrication of large-scale ultra-smooth metal surfaces by a replica technique, *Appl. Phys. A Mater. Sci. Process.*, 73, 3, 273–279, 2001.

[73] D. W. Mosley, B. Y. Chow, and J. M. Jacobson, Solid-state bonding technique for template-stripped ultraflat gold substrates., *Langmuir*, 22, 6, 2437–40, 2006.

[74] Samorí, J. Diebel, H. Löwe, and J. Rabe, Template-Stripped Gold Supported on Ni as a Substrate for SAMs, *Langmuir*, 15, 7, 2592–2594, 1999.

[75] J. J. Blackstock, Z. Li, and G. Jung, Template stripping using cold welding, *J. Vac. Sci. Technol. A Vacuum, Surfaces, Film.*, 22, 3, 602, 2004.

[76] D.-Y. Khang, H. Jiang, Y. Huang, and J. a Rogers, A stretchable form of single-crystal silicon for high-performance electronics on rubber substrates., *Science*, 311, 5758, 208–12, 2006.

[77] D.-H. Kim, J.-H. Ahn, W. M. Choi, H.-S. Kim, T.-H. Kim, J. Song, Y. Y. Huang, Z. Liu, C. Lu, and J. a Rogers, Stretchable and foldable silicon integrated circuits., *Science*, 320, 5875, 507–11, 2008.

[78] A. Turchanin, A. Beyer, C. T. Nottbohm, X. Zhang, R. Stosch, A. Sologubenko, J. Mayer, Hinze, T. Weimann, and A. Gölzhäuser, One Nanometre Thin Carbon Nanosheets with Tuneable Conductivity and Stiffness, *Adv. Mater.*, 21, 12, 1233–1237, 2009.

[79] K. S. Kim, Y. Zhao, H. Jang, S. Y. Lee, J. M. Kim, J.-H. Ahn, Kim, J.-Y. Choi, and B. H. Hong, Large-scale pattern growth of graphene films for stretchable transparent electrodes., *Nature*, 457, 7230, 706–10, 2009.

[80] E. Sabatani, J. Cohen-Boulakia, M. Bruening, and I. Rubinstein, Thioaromatic monolayers on gold: a new family of self-assembling monolayers, *Langmuir*, 9, 11, 2974–2981, 1993.

[81] A. J. Pollard, R. R. Nair, S. N. Sabki, C. R. Staddon, L. M. A. Perdigão, C. H. Hsu, J. M. Garfitt, S. Gangopadhyay, H. F. Gleeson, A. K. Geim, and H. Beton, Formation of Monolayer Graphene by Annealing Sacrificial Nickel Thin Films, *J. Phys. Chem. C*, 113, 38, 16565–16567, 2009.

[82] Q. Yu, J. Lian, S. Siriponglert, H. Li, Y. Chen, and S.-S. Pei, Graphene segregated on Ni surfaces and transferred to insulators, *Appl. Phys. Lett.*, 93, 11, 113103, 2008.

[83] A. Reina, X. Jia, J. Ho, D. Nezich, H. Son, V. Bulovic, M. S. Dresselhaus, and J. Kong, Large area, few-layer graphene films on arbitrary substrates by chemical vapour deposition., *Nano Lett.*, 9, 1, 30–5, 2009.

[84] L. N. Rozanov, *Vacuum Technique*. CRC Press, 2002.

[85] M. Henzler and W. Göpel, *Oberflächenphysik des Festkörpers*. Vieweg+Teubner Verlag, 1994.

[86] M. Knudsen, Laws of Molecular Flow and Internal Viscosity Flow of Gases through Tubes., *Ann. Phys. Lpz*, 28, 75–130, 1908.

[87] G. Sauerbrey, Verwendung von Schwingquarzen zur Wägung dünner Schichten und zur Mikrowägung., *Zeitschrift für Phys.*, 155, 2, 206–222, 1959.

[88] J. Fenn, M. Mann, C. Meng, S. Wong, and C. Whitehouse, Electrospray ionization for mass spectrometry of large biomolecules., *Science*, 246, 4926, 64–71, 1989.

[89] A. Jaworek, Micro- and nanoparticle production by electrospraying, *Powder Technol.*, 176, 1, 18–35, 2007.

[90] J.C. Swarbrick, J. B. Taylor, J. N. O'Shea, Electrospray deposition in Vacuum., *Applied Surface Science,* 15, *252,* 5622-5626, 2006.

[91] J. N. O'Shea, J. B. Taylor, J. C. Swarbrick, G. Magnano, L. C. Mayor, and K. Schulte, Electrospray deposition of carbon nanotubes in vacuum., *Nanotechnology*, 18, 3, 035707, 2007.

[92] G. Binning, H. Rohrer, C. Gerber, and E. Weibel, Surface studies by scanning thermal microscopy, *Phy. Rev. Lett*, 49, 57–61, 1982.

[93] J. Bardeen, Tunnelling from a many-particle point of view, *Phys. Rev. Lett.*, 6, 57, 1961.

[94] C. Julian Chen. Introduction to scanning tunneling microscopy. Oxford series in optical and imaging sciences 4. *Oxford University Press*, New York, 1993.

[95] J. Tersoff and D. R. Hamann, Theory and Application for the Scanning Tunneling Microscope, *Phys. Rev. Lett.*, 50, 25, 1998–2001, 1983.

[96] K. Hansma and J. Tersoff, Scanning tunneling microscopy, *J. Appl. Phys.*, 61, 2, R1, 1987.

[97] J. Wintterlin, J. Trost, S. Renisch, R. Schuster, T. Zambelli, and G. Ertl, Real-time STM observations of atomic equilibrium fluctuations in an adsorbate system: O/Ru(0001), *Surf. Sci.*, 394, 1–3, 159–169, 1997.

[98] M. J. Rost, L. Crama, Schakel, E. van Tol, G. B. E. M. van Velzen-Williams, C. F. Overgauw, H. ter Horst, H. Dekker, B. Okhuijsen, M. Seynen, A. Vijftigschild, Han, A. J. Katan, K. Schoots, R. Schumm, W. van Loo, T. H.

Oosterkamp, and J. W. M. Frenken. Scanning probe microscopes go video rate and beyond. *Review of Scientific Instruments*, 76, 5, 053710, 2005.

[99] Z.-X. Xie, Z.-F. Huang, and X. Xu, Influence of reconstruction on the structure of self-assembled normal-alkane monolayers on Au(111) surfaces, *Phys. Chem. Chem. Phys.*, 4, 8, 1486–1489, 2002.

[100] J. V. Barth, H. Brune, G. Ertl, and R. J. Behm. Scanning tunnelling microscopy observations on the reconstructed Au(111) surface - atomic structure, long-range superstructure, rotational domains and surface defects. *Physical Review B*, 42, 15, 9307-9318, 1990.

[101] A. Sharma and S. G. Schulman, *Introduction to Fluorescence Spectroscopy*. Wiley, 1999.

[102] J. R. Ferraro and K. Nakamoto, Introductory Raman Spectroscopy, *Academic Press Ltd* 1994.

[103] C. V. Raman and K. S. Krishnan, A new type of secondary radiation, *Nature*, *121*, 501-502, 1928.

[104] R. L. McCreery, Raman Spectroscopy for Chemical Analysis, *Wiley-Interscience* 2000

[105] V. Schettino, M. Pagliai, L. Ciabini, and G. Cardini, The Vibrational Spectrum of Fullerene C 60, *J. Phys. Chem. A*, 105, 50, 11192–11196, 2001.

[106] M. Cardona and G. Güntherodt, Eds., *Light Scattering in Solids VIII*, 76. Springer Berlin Heidelberg, 2000.

[107] J. Menéndez, J. B. Page, and S. Guha, The isotope effect on the Raman spectrum of molecular C60, *Philos. Mag. Part B*, 70, 3, 651–659, 1994.

[108] W. H. Zachariasen, The Atomic Arrangement In Glass, *J. Am. Chem. Soc.*, 54, 10, 3841–3851, 1932.

[109] S. Blankenburg, M. Bieri, and R. Fasel, Porous graphene as an atmospheric nanofilter, *Small*, 6(20), 2266–2271, 2010.

[110] I. Horcas, R. Fernández, J. M. Gómez-Rodríguez, J. Colchero, J. Gómez-Herrero, and A. M. Baro, WSXM: a software for scanning probe

microscopy and a tool for nanotechnology., *Rev. Sci. Instrum.*, 78, 1, 013705, 2007.

[111] J. Schindelin, I. Arganda-Carreras, E. Frise, V. Kaynig, M. Longair, T. Pietzsch, S. Preibisch, C. Rueden, S. Saalfeld, B. Schmid, J.-Y. Tinevez, D. J. White, V. Hartenstein, K. Eliceiri, Tomancak, and A. Cardona, Fiji: an open-source platform for biological-image analysis., *Nat. Methods*, 9, 7, 676–82, 2012.

[112] M. Dion, H. Rydberg, E. Schröder, D. C. Langreth, and B. I. Lundqvist, Van der Waals Density Functional for General Geometries, *Phys. Rev. Lett.*, 92, 24, 246401, 2004.

[113] S. Whitelam, I. Tamblyn, T. K. Haxton, M. B. Wieland, N. R. Champness, J. Garrahan, and H. Beton, Common Physical Framework Explains Phase Behavior and Dynamics of Atomic, Molecular, and Polymeric Network Formers, *Phys. Rev. X*, 4, 1, 011044, 2014.

[114] S.P. Jarvis, S. Taylor, J. D. Baran, D. Thompson, A. Saywell, N. Champness, L. Grill, J. A. Larsson, and P. Moriarty, Physisorption Controls Conformation of TetraPhenyl-Porphyrins on Cu(111)., *manuscript in preparation*

[115] B. N. Cotier, M. D. Upward, F. H. Jones, Moriarty, and H. Beton, Atomic scale protection using fullerene encapsulation, *Appl. Phys. Lett.*, 78, 1, 126, 2001.

[116] J. Catalan and J. Elguero, Fluorescence of C60 and C70, *J. Am. Chem. Soc.*, 9, 9249–9252, 1993.

[117] L. Lafferentz, F. Ample, H. Yu, S. Hecht, C. Joachim, L. Grill, and H. Hu, Conductance of a single conjugated polymer as a continuous function of its length., *Science*, 323, 5918, 1193–7, 2009.

[118] A. Saywell, J. K. Sprafke, L. J. Esdaile, A. J. Britton, A. Rienzo, H. L. Anderson, J. N. O'Shea, and H. Beton, Conformation and packing of porphyrin polymer chains deposited using electrospray on a gold surface., *Angew. Chem. Int. Ed. Engl.*, 49, 48, 9136–9, 2010.

[119] G. McDermott, S. M. Prince, A. A. Freer, A. M. Hawthornthwaite-Lawless, M. Z. Papiz, R. J. Cogdell, and N. W. Isaacs, "Crystal structure of an integral membrane light-harvesting complex from photosynthetic bacteria," *Nature*, 374, 6522, 517–521, 1995.

[120] R. Madueno, M. T. Räisänen, C. Silien, and M. Buck, Functionalizing hydrogen-bonded surface networks with self-assembled monolayers., *Nature*, 454, 7204, 618–21, 2008.

[121] S. A. Svatek, L. M. A. Perdigão, A. Stannard, M. B. Wieland, D. V Kondratuk, H. L. Anderson, J. N. O'Shea, and H. Beton, Mechanical stiffening of porphyrin nanorings through supramolecular columnar stacking., *Nano Lett.*, 13, 7, 3391–5, 2013.

[122] M. Hutin, J. K. Sprafke, B. Odell, H. L. Anderson, and T. D. W. Claridge, A discrete three-layer stack aggregate of a linear porphyrin tetramer: solution-phase structure elucidation by NMR and X-ray scattering., *J. Am. Chem. Soc.*, 135, 34, 12798–807, 2013.

[123] S. Guo, D. Fogarty, M. Nagel, and S. A. Kandel, Thermal Diffusion of C60 Molecules and Clusters on Au(111), 111, 14074–14081, 2004.

[124] M. Roman and M. Baranska, Vibrational and theoretical study of selected diacetylenes., *Spectrochim. Acta. A. Mol. Biomol. Spectrosc.*, 115, 493–503, 2013.